Synthesis and Characterization of Novel Fullerenes and Carbon Nanotubes

by

Charles Richard Piskoti

B. A. (University of Michigan at Flint) 1995
M. S. (University of California at Berkeley) 1998

A dissertation submitted in partial satisfaction of the requirements for the degree of

Doctor of Philosophy
in

Physics

in the

GRADUATE DIVISION

of the

UNIVERSITY OF CALIFORNIA, BERKELEY

Committee in charge:

Professor Alex Zettl, Chair
Professor Marvin Cohen
Professor Jeffrey Long

Spring 2000

Synthesis and Characterization of Novel Fullerenes and Carbon Nanotubes

by

Charles Richard Piskoti

Table of Contents

Chapter 1.

Introduction and outline.....1

Chapter 2.

Historical perspective..... 4

2.1 Discovery of C_{60} 4
2.2 Bulk synthesis 6
2.3 Details of the Krätschmer-Huffman arc technique 7
2.4 Superconducting fullerites 8
2.5 Theory of superconductivity in fullerenes 8
2.6 Description of doping experiment 11
2.7 Higher fullerenes 14
2.8 Carbon nanotubes 15
2.9 Nanotube synthesis 17
2.10 Carbon nanotube theory and applications 19
2.11 Lower fullerenes 20

Chapter 3.

Carbon 36..... 22

3.1 Nitrogenated fullerenes 22
3.2 Synthesis of C_{36} 25
3.3 Predicting which fullerenes will form 27
3.4 Clathrin 31

Chapter 4.

C_{36} theory 34

4.1 Introduction 34
4.2 C_{36} molecule 34
4.3 C_{36} dimers 36
4.4 C_{36} solids 39
4.5 Superconductivity 41
4.6 Doping of C_{36} 42
4.7 Other properties of C_{36} 46

Chapter 5.

C_{36} experiment 49

5.1 Solubility and air sensitivity 49
5.2 Mass spectrometry of pyridine extract 53
5.3 Electron diffraction 55
5.4 Scanning tunneling spectroscopy 57
5.5 Infrared spectroscopy 61
5.6 Transport measurements 62
5.7 Microwave loss measurements 67
5.8 Magnetization measurements and organic ferromagnets 69
5.9 C_{36} derivatives 74

Chapter 6.

Other experiments 77

6.1 Coated ferromagnetic nanoclusters 77
6.2 Enhanced growth of multi-walled carbon nanotubes 82
6.3 Nanotube doping 87

Bibliography 93

List of Figures

Figure 2-1.Mass spectrum published by Rohfling,Cox and Kaldor showing peaks which vary by single carbon atoms below C_{30} and by carbon dimers above C_{30} 5

Figure 2-2.Schematic of the Krätschmer-Huffman arc chamber used for producing fullerenes. 7

Figure 2-3.Diagram showing how the energy levels of a C_{60} molecule (left) broaden into the energy bands in a K_3C_{60} crystal (right)[9]. 9

Figure 2-4.Basic design of the doping cell originally used to dope C_{60} thin films. 12

Figure 2-5.Transmission electron micrographs of a) a multi-walled carbon nanotube and b) a single-walled carbon nanotube. 16

Figure 2.6.Schematic of the laser ablation setup for producing high purity single-walled carbon nanotubes. 17

Figure 3-1.Notebook page (JBH notebook #1) showing mass spectrum of graphite sublimation product formed in nitrogen. 23

Figure 3-2.Proposed structure for $C_{30}N_6$. 24

Figure 3-3.a) Mass spectrum of raw soot from graphite arc at 400 torr He. b) Mass spectrum of a film evaporated from the soot of figure 3.3a after C_{60} and higher fullerenes had been extracted with toluene. 28

Figure 3-4.Pictures of all possible C36 isomers consisting exclusively of pentagons and hexagons. 30

Figure 3-5.A chart showing the most common spherical clathrin molecules observed. 32

Figure 4-1.Six structural isomers of C_{36}: (a) the D_{6h}, (b) D_{2d}, (c) C_{2v} and (d) D_{3h} fullerenes, (e) the C_{3v} bowl and (f) the D_{18d} ring. 35

Figure 4-2.Several dimers and one of the trimers studied by Grossman, et. al.. 37

Figure 4-3.Reaction pathway for two neutral C_{36} molecules and two C_{36}^{-1} anions. ... 38

Figure 4-4.Fully relaxed LDA crystal structures formed by stacking planes of unbonded C_{36} units. 39

Figure 4-5.Fully relaxed LDA crystal structures formed by stacking planes of bonded C_{36} units. 40

Figure 4-6.The (a) D_{6h} $C_{24}N_{12}$ fullerene and the (b) D_{6h} $C_{36}Cl_{12}$ fullerene. 43

Figure 4-7.Na_2C_{36} nad K_2C_{36} crystal structures. 45

Figure 4-8.LDA calculated IR spectra for the D_{6h} and D_{2d} molecules. 48

Figure 5-1.Schematic of a new arc chamber designed to be transferred into an argon glovebox prior to opening. 50

Figure 5-2.Schematic of the extractor used to extract C_{36} under inert conditions. 52

Figure 5-3.a)Time of flight mass spectrum of the pyridine soluble extract. b) Time of flight mass spectrum of the same material after reduction with potassium in liquid ammonia. 54

Figure 5-4.Electron diffraction pattern of a C36 crystallite. The pattern is hexagonal with a calculated d-spacing of 6.68 Å. 56

Figure 5-5.N(E) for C_{36} as measured on Au (111) and HOPG substrates. 58

Figure 5-6.Theoretical electronic spectra for five different configurations of C36 molecules illustrated in figure 4.3. 59

Figure 5-7.Infrared spectrum of the pyridine extract after baking at 225 °C overnight in vacuum to remove adsorbed pyridine. 61

Figure 5-8.Resistance vs. temperature of a potassium doped C_{36} sample under 37 kbar

pressure. 64

Figure 5.9.Several I-V curves on a sample of potassium doped C_{36} at 37 kbar. 65

Figure 5.10.Resistance vs. temperature plot for potassium doped C_{36} data measured at low current levels. 66

Figure 5.11.Plot showing the change in microwave power with magnetic field vs. the total applied field. 68

Figure 5.12.Magnetization data for 50 mg of K_3C_{60} (T_c = 19.3K. 71

Figure 5.13.Magnetization data for potassium intercalated C_{36} using a magnetic field of 30 gauss. 72

Figure 5-14.Magnetization of C_{36} vs. magnetic field at 100K. 73

Figure 5-15.Electron impact mass spectrum of the product from a reaction with C_{36}, n-butyl lithium and methyl iodide. 76

Figure 6-1.Transmission electron micrograph of several ferromagnetic nanoclusters. 79

Figure 6-2.Selected area electron diffraction pattern from several nickel/iron clusters. 80

Figure 6-3.Plot comparing growth rate of nanotube-rich material to total pressure for both pure helium and a 1:1 nitrogen/helium buffer gas. 86

Figure 6-4.TEM micrograph of typical multi-wall carbon nanotubes grown in the low pressure nitrogen/helium arc. 87

Figure 6-5.Resistance vs. temperature plot of single-walled nanotubes before and after baking at 425°C for 8 hours. 90

Figure 6-6.Resistance vs. temperature plot of single-walled carbon nanotubes after baking and intercalating with C_{60}. 91

Figure 6-7.Resistance vs. temperature plot of single-walled carbon nanotubes, previously

doped with C_{60}, after baking and intercalating with potassium. 92

List of Tables

Table 2-1:Maximum conductivity reached in several C_{60} doping experiments conducted at AT&T Bell Laboratories. 11

Table 2-2:A list of most of the superconducting doped phases of C_{60} in order from lowest to highest T_c. 13

Table 4-1:Binding energy (eV/C_{36}), density (C_{36}/au^3) and gap (eV) for each crystal structure considered here. 44

Table 4-2:Calculated NMR chemical shifts (ppm) relative to TMS for C_{36} fullerenes with D_{6h} and D_{2d} symmetries.. 47

Table 6-1:Data on yield and growth rate for a series of 5 minute arc runs in pure helium buffer gas. 83

Table 6-2:Data on yield and growth rate for a series of 5 minute arc runs in a 1:1 helium/nitrogen buffer gas. 84

Acknowledgments

I wish to thank my advisor, Professor Alex Zettl, for all that he has taught me. I feel that his guidance has helped me to develop into a well rounded experimentalist, not to mention an expert white water rafter and a more knowledgeable Porsche/Volkswagon mechanic. His systematic, rational approach to problem solving is something that I plan to emulate throughout my career.

I would also like to acknowledge our theorist collaborators, Professor M. L. Cohen, Professor S. G. Louie, Dr. J. C. Grossman and Dr. M. Côté, who made this work possible by providing the driving force that lead to the many breakthroughs on the C_{36} project. I am certainly indebted to all of them for our many fruitful discussions and all of the ideas that they generate.

Over my years at Berkeley I have enjoyed working and interacting with many colleagues in the Zettl group. During my first two years, I was the newcomer. The lab at that time consisted of Nasreen Chopra, Kasra Khazeni, Phil Collins, Michael Fuhrer and Jim Hone. Nasreen quickly became my first close friend in graduate school after we started working together on synthesis and microscopy of nanotubes. I couldn't have asked to meet a warmer, more friendly person in my first few days of being in Berkeley. Kasra also became a friend who taught me lot about fashion and especially shoes. Phil is one of the hardest working scientists I've ever met. I respect his determination for taking on a project that few would ever dream of attempting. Michael and Jim are both truly great experimentalists as well as great practical joksters every April 1st.

Over the past year, I've assumed the role of senior graduate student to an entirely

new set of Zettl group members. These include John Cumings, Masahiro Ishigami, Keith Bradley, Adam Fennimore, Xiaosheng Huang and Aileen Wang. John is certainly one of the most productive graduate student that I've ever worked with. He seems to have a knack for figuring out which problems in research are solvable and then he tackles these projects head on often producing swift and groundbreaking results. I've also established a friendship with John and I admire him for his taste in music, his very unique outlook on the world and his understanding of the way that the DMV issues license plates. Masa has inherited the difficult task of maintaining and operating the low temperature STM. I know that with his uncompromising work ethic and attention to detail that he is the right scientist for the job. Masa has also been a good friend. I've enjoyed watching and talking about baseball and movies with him. Keith is also someone who has the ability to solve tough research problems with great efficiency. I'm glad I was able to work with him and I'm equally glad that I never had to ride in a car with him (just kidding Keith). Adam, Xiaosheng and Aileen are all first rate physicists whom I wish I had had the opportunity to work more closely with.

I've also been lucky enough to have the help of two undergraduate assistants: Jane Burward-Hoy and Sabrina Qwan. Jane was instrumental in the execution of some of the early experiments of the C_{36} project. Both Jane and Sabrina were very hands on experimentalists who never had a problem with getting covered with carbonaceous soot, a quality that was essential for this kind of work. I've also become good friends with Sabrina and I know that I will miss those long conversations we've had about both of our futures.

Most of all, I wish to acknowledge everyone in my family. My father and mother, Charles and Irene, for their love, support and all they have taught me. My dad has taught

me how to be a critical thinker which has helped to give me a solid foundation as a scientist. My mother has taught me countless things about life which I could not have learned in my years of formal academic training. My sister, Beth, is someone who I admire very much for all she has accomplished in her medical career. Every time I've felt overwhelmed by graduate school, I gain motivation by thinking about the extreme challenges that she faces and overcomes every day. I am also grateful to my uncle Jim and aunt Carol for giving me a place to escape to on days when I needed to get away from Berkeley, not to mention a home cooked meal. My cousin, Kirk McCardell, and best friend, Chris Rowe, are two people that, through many long telephone calls, helped me feel like I never left Michigan even though I was 3000 miles away.

Finally, I want to acknowledge all of the friends I've made here in Berkeley. I know that Friday evenings won't be the same without my friends Brent Nelson, Matt McKerley and Dan Brace. It had become a routine for Brent, Dan and I to wait for Matt to commute back from Redwood City which usually took most of the night. Another routine was when they would ask me on a weekly basis whether or not I had the proof I needed on the C_{36} project. Having this fan club really helped me keep my enthusiasm for the project.

Chapter 1.

Introduction and outline

A major part of this thesis details a collaborative effort that lead to the discovery and ongoing research of the new pure carbon molecule, C_{36}. Chapter 2 begins by detailing the history of fullerene molecules starting with the original mass spectrometry work performed 1984. Prior to the discovery of these pure carbon molecules, carbon was thought to only exist in two allotropes, graphite and diamond. The study by Kroto, et. al. opened up an entirely new field of research into a new class of pure carbon molecules known as fullerenes[1]. Coincidentally, carbon nanotubes were discovered in 1991 when the flurry of fullerene research was nearing its peak. Because nanotubes are also pure carbon structures, they are often placed in the same category as fullerenes. Our research group, like many others, has focused on both fullerenes and nanotubes over the past several years. Because these fields are so interrelated, this chapter also chronicles the early history of carbon nanotube research. Wherever appropriate, specific details are given about the methods of synthesizing these new materials

Chapter 3 gives a detailed account of the work leading up to the discovery of C_{36}. This project was initiated during a joint theoretical/experimental investigation into synthesizing fullerenes containing nitrogen in place of selected carbon atoms on various fullerene molecules. This investigation lead to a strong collaborative effort between Professors Cohen and Louie's theory group and Professor Zettl's experimental group in trying

to find and characterize both C_{36} and the nitrogen doped $C_{30}N_6$ and $C_{24}N_{12}$. This chapter presents some of the early mass spectral evidence for C_{36}. It also describes some of the research problems faced when dealing with lower fullerenes. This includes the necessary violation of the isolated pentagon rule and the large number of isomers that must be ruled out when trying to determine the structure of these molecules.

Chapter 4 summarizes most of the theoretical calculations performed by our collaborators: Dr. J. C. Grossman, M. Côté, Professor M. L. Cohen and Professor S. G. Louie. Properties of the single C_{36} molecule are examined as well as dimers, trimers and infinite solids consisting of pure C_{36} and compounds consisting of C_{36} and alkali metals. Several variations of C_{36} are treated such as the nitrogen substituted $C_{24}N_{12}$, the chlorinated $C_{36}Cl_{12}$ and C_{36} with metal atoms trapped inside. For the purpose of characterization, several basic properties were calculated such as infrared and nuclear magnetic resonance spectroscopy. One of the most interesting results from this work is the prediction that solids containing C_{36} have a possibility of exhibiting high temperature superconductivity.

Chapter 5 describes all of the experimental work that has been done in the Zettl group to synthesize, characterize and derivatize C_{36}. The synthesis method is described in detail including all precautions taken to keep the material from being exposed to air. Results are presented on mass spectrometry, electron diffraction, infrared spectroscopy as well as transport, magnetic susceptibility and microwave loss spectroscopy on alkali doped samples. Preliminary results on possible superconductivity in C_{36} are discussed.

Chapter 6 summarizes significant experimental results not related to C_{36}. This

includes a study of growth enhancement of multi-walled nanotubes. This enhancement was achieved by introducing a partial pressure of nitrogen gas into the synthesis chamber. Also included is a study of the changes in single-wall nanotube transport under the influence of baking and intercalation and a new method of producing coated, ferromagnetic nanoclusters.

Chapter 2.

Historical perspective

2.1 Discovery of C_{60}

In the mid-1980's, a new class of pure carbon molecules was discovered by Kroto, Curl, Heath and Smalley while studying the mass distribution of carbon cluster ions produced during laser vaporization of a graphite target[1]. Their findings showed that carbon clusters formed for every carbon number below C_{30} and for every even numbered carbon cluster above C_{30}. Also, as the power of the Nd:YAG ablation laser was varied, they found a consistently large signal at the peak corresponding to C_{60}. A similar carbon cluster experiment was almost simultaneously performed by Rohlfing, Cox and Kaldor at Exxon's Corporate Research Science lab[2]. This group also observed only even numbered carbon clusters above C_{30} as well as the presence of an unusually large peak at C_{60}. Although the data from these groups appeared nearly identical, the interpretations were very different. The Exxon group assigned the larger clusters to carbyne structures, linear chains of carbon with alternating single and triple bonds. Because the subunit of carbyne is a C$_2$ dimer, this explained why only even numbered clusters were present in the high mass end of the spectra. No explanation was given for the slightly larger peak at C_{60}. Contrary to this, Kroto, et. al. included in their paper the hypothesis that C_{60} was a stable molecule with a hollow,

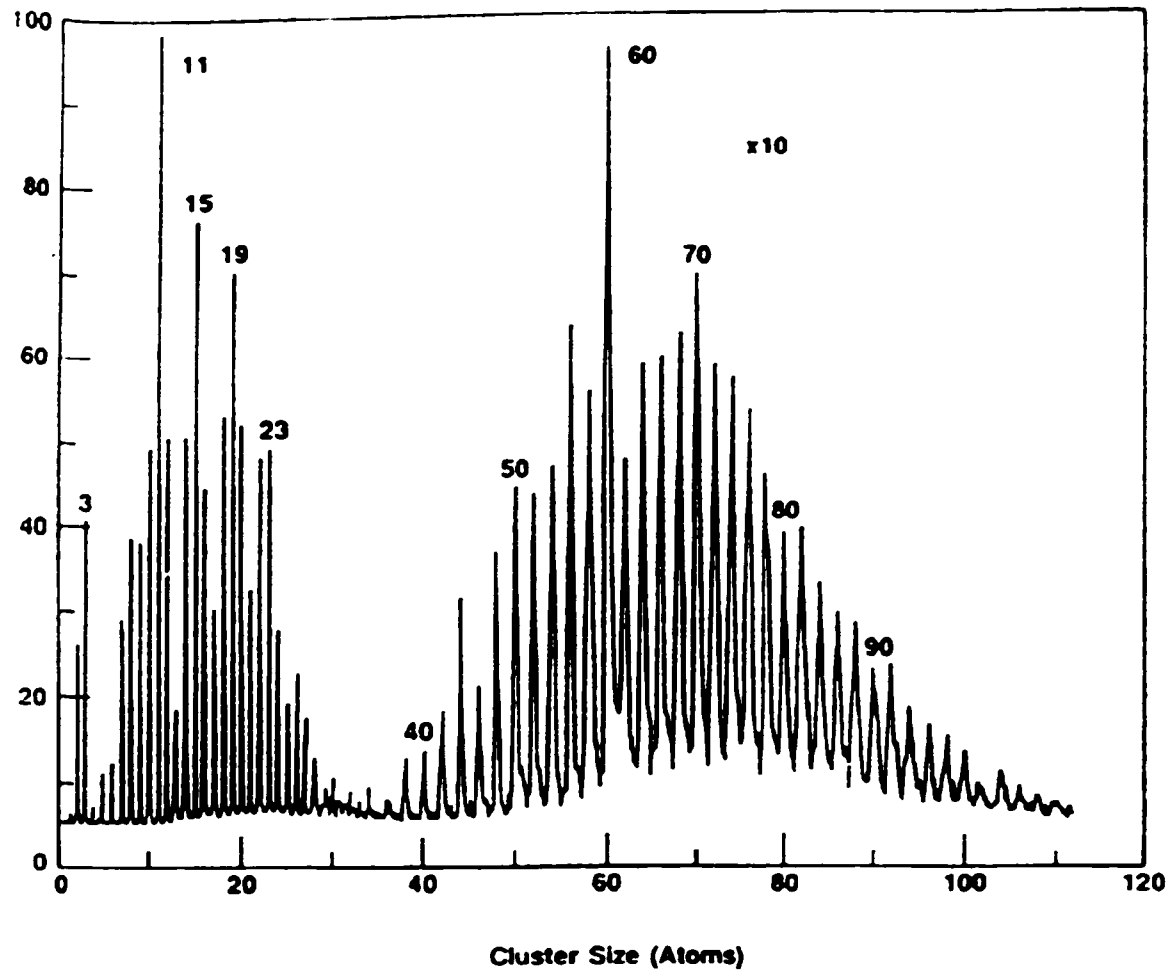

Figure 2.1: Mass spectrum published by Rohlfing, Cox and Kaldor showing peaks which vary by single carbon atoms below C_{30} and by carbon dimers above C_{30}[2]. Also present is an especially large peak at C_{60}. This result is almost identical to the spectra reported by the Smalley group[1]. (Adapted from Ref. [2])

caged structure consisting of 20 hexagons and 12 pentagons with each pentagon surrounded by hexagons. This truncated icosahedral structure is identical to the pattern found on a soccer ball. This proposed molecule was named "buckminsterfullerene" because of it's similarity to the geodesic domes designed by the architect Buckminster Fuller.

2.2 Bulk synthesis

Although some forms of spectroscopy and photofragmentation experiments can be

studied on molecules in the flight tube of a Time of Flight mass spectrometer, the best way to prove the existence of new molecules like Buckminsterfullerene is to synthesize macroscopic quantities and perform a complete chemical characterization. This includes x-ray diffraction (XRD), nuclear magnetic resonance (NMR) and infrared and ultraviolet spectroscopy.

In 1990, five years after the buckminsterfullerene molecule was proposed[1], bulk synthesis was accomplished by Krätchmer, et. al. using a very simple graphite-arc technique[3]. The researchers noticed that soot produced by graphite sublimation in the presence of helium contained unexpected spectral characteristics. The ultraviolet spectrum of the soot contained two very broad absorptions and the infrared spectra showed four prominent, sharp peaks, amidst other minor peaks, indicative of a molecular absorption. The peaks were found to reach a maximum intensity in soot that was sublimated at 100 torr helium pressure. The group lead by Krätschmer and Huffman also discovered that a small fraction of this soot was soluble in benzene and could therefore be purified by dispersing the soot in benzene and filtering. This benzene-soluble fraction which contained much stronger analogs of the optical absorptions observed in the raw soot produced a reddish-brown solution. Mass spectroscopy studies revealed that this material consisted of approximately 90% C_{60} and 10% C_{70}. It was also noticed that this new material crystallized readily upon evaporation of the benzene. Preliminary x-ray diffraction (XRD) analysis indicated that C_{60} tends to form a close-packed van der Waals crystal with both ABCABC.... stacking (face-centered cubic lattice) as well as ABABAB.... stacking (hexagonal close-packed lattice).

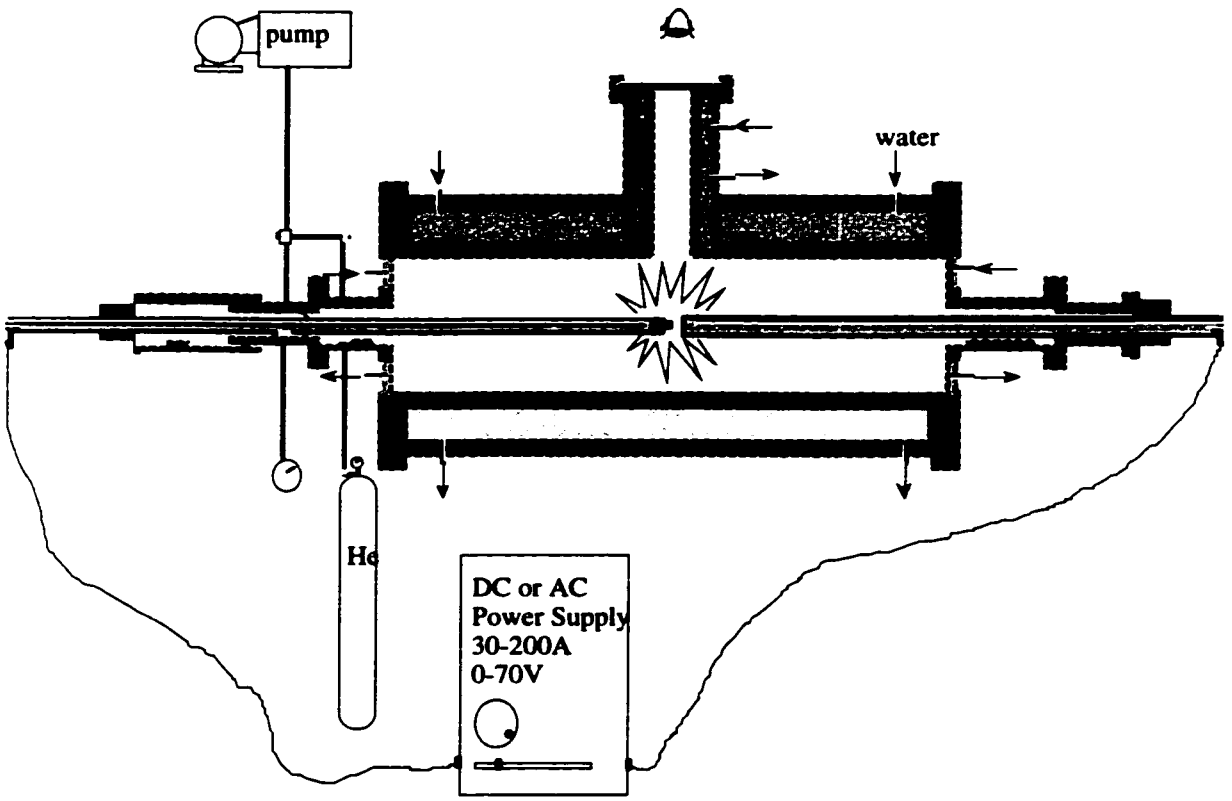

Figure 2.2: Schematic of the Krätschmer-Huffman arc chamber used for producing fullerenes. (Adapted from Ref. [30])

2.3 Details of the Krätschmer-Huffman arc technique

The Krätschmer-Huffman arc technique uses a water-cooled, high vacuum chamber, as shown in fig. 2.2. Two graphite electrodes, approximately 6mm in diameter are affixed to water-cooled copper holders which enter the chamber on opposite sides through dynamic o-ring seals. The chamber is flushed out with helium and pressurized to 100 torr helium for optimum production of C_{60} and higher fullerenes. Graphite sublimation can be obtained in two different ways. One method involves sharpening the graphite electrodes to points which make contact with one another. A large D. C. current on the order of 100 amperes is then put across the electrodes causing the temperature at the narrow tip to exceed 3000° Kelvin. As graphite sublimates from the anode, contact is maintained by

pushing the electrodes together with a small force. Graphite sublimation ceases once the electrodes are no longer sharp, usually after a matter of minutes. In the second, more common method, the ends of the graphite electrodes are left flat. These electrodes are connected to a constant current, D. C. power supply set to approximately 100 amperes. An arc is struck by touching the electrodes together and pulling apart to establish about a 1 mm gap. This gap is maintained by feeding the anode (positive electrode) into the arc. By this method, it is possible to sublimate graphite continuously until the anode is consumed. Typically about 1 - 10% of the anode is converted to fullerenes.

2.4 Superconducting fullerites

In 1991, researchers at AT&T Bell Laboratories discovered that films of C_{60} could be made metallic and even superconducting by intercalation with alkali metals[4]. The first material reported was a film with the stoichiometry K_3C_{60} which has a superconducting critical temperature (T_c) of 19.2° K. This new compound set the record for the highest T_c of any organic superconductor. To date, this record is now held by Cs_3C_{60} which has a T_c of 40° K under pressure[5]. This section will briefly discuss both the theoretical background necessary to understand this new class of C_{60} based superconductors as well as some of the experimental techniques used to synthesize these compounds.

2.5 Theory of superconductivity in fullerenes

The most obvious difference between a single C_{60} molecule and a 60 carbon atom graphite sheet is the fact that the carbon bonds on the C_{60} molecule are not planar. In graphite, the electrons which form the bonds between carbon atoms are in a state which is a superposition of the s, p_x and p_y orbitals of a single carbon atom (the z direction is per-

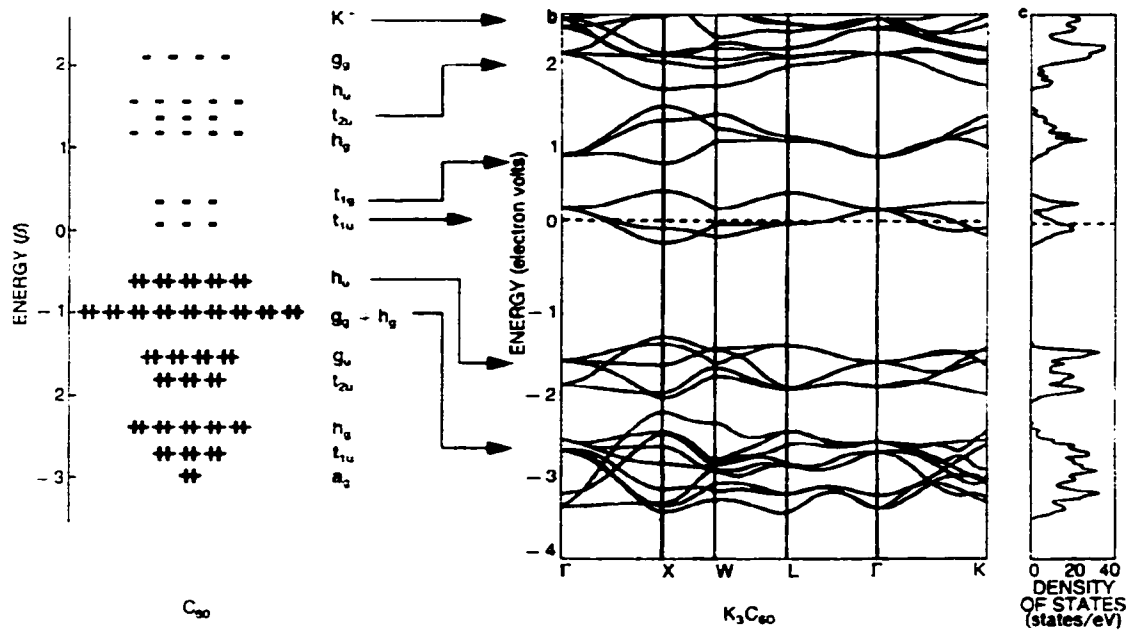

Figure 2.3: Diagram showing how the energy levels of a C_{60} molecule (left) broaden into the energy bands in a K_3C_{60} crystal (right). (Adapted from Ref. [9])

pendicular to the graphite sheet). This type of bond is referred to as sp^2 hybridized. The lobes of the nonbonding p_z orbital extend along the z axis symmetrically above and below the plane of the graphite sheet. It is the overlap of these p orbitals that makes graphite a semimetal. In the case of C_{60}, the symmetry of the p_z orbital is broken by the curvature of the molecule[6]. Here, a larger portion of the p_z orbital extends in the +z direction (outside the molecule) than in the -z direction (inside the molecule). The limiting case would be if the curvature became so great that the bond angles matched those found in diamond. In that case, the bonding wavefunctions would be a hybrid of the s orbital and all three p orbitals (sp^3) with an unpaired electron on the outside. Therefore, the types of bonds in C_{60} can be regarded as a hybrid of sp^2 and sp^3 carbon bonds. One effect of this curvature

is a strong increase in the electronegativity of the C_{60} molecule or it's capacity to be doped with electrons[6].

Higher curvature is also believed to enhance the T_c of a carbon based superconductor[7]. Based on simple arguments, graphite seems likely to have an excellent chance of being a high temperature superconductor. The strength of the carbon bonds within each layer produce a rich spectrum of high frequency phonon modes to couple with electrons. Unfortunately, the planarity of the graphite layers greatly hinders this coupling. From the Bardeen, Cooper, and Schrieffer (BCS) theory of superconductivity, T_c is calculated by the following equation:

$$T_c = 1.14\theta e^{-1/VN[E_f]} \qquad (2.1)$$

Here, V is the electron-phonon coupling constant, $N[E_f]$ is the density of states at the Fermi level and θ is the Debye temperature. V is the sum of all matrix elements which are used to calculate the lowering of energy states at the fermi level due to the lattice distortion caused by each vibrational mode. In graphite, matrix elements vanish for modes perpendicular to the graphite sheet when coupled to electronic states with the same parity. This greatly suppresses the potential T_c of any graphite-based superconductor. For example, graphite can be made superconducting by increasing $N[E_f]$ with potassium doping, but T_c for C_8K is only 150 mK[8]. As the graphitic sheet is curved, symmetry is broken and previously vanishing matrix elements begin to contribute.

A Hückel calculation of a single C_{60} molecule is shown on the left side of fig. 2.3[9]. As C_{60} molecules are packed into a van der Waals crystal with a face centered cubic lattice, these energy levels broaden out into the energy bands shown in the band structure at the right of fig. 2.3. This pure C_{60} solid is a semiconductor with a 1.5 eV

bandgap. The electron accepting nature of the C_{60} molecule along with the great potential for superconductivity lead researchers at AT&T Bell laboratories to examine the possibility of making C_{60} metallic by doping the lowest unoccupied molecular orbital (LUMO). Alkali metals were the obvious choice due to their ability to donate their outer most electron.

Film	Dopant	Maximum Conductivity (S/cm)
C_{60}	Lithium	10
C_{60}	Sodium	20
C_{60}	Potassium	500
C_{60}	Rubidium	100
C_{60}	Cesium	4
C_{70}	Potassium	2

Table 2.1: Maximum conductivity reached in several C_{60} doping experiments conducted at AT&T Bell Laboratories. The phases with the largest conductivity (K_3C_{60} and Rb_3C_{60}) are superconductors at low temperature. (Adapted from R. C. Haddon, et. al., Nature **350**, 320 (1991))

2.6 Description of doping experiment

Figure 2.4 shows a diagram of the experimental cell originally used by Haddon, et. al. for doping thin films of C_{60} with alkali metals[6]. The films of C_{60} had been grown over four metallic pads connected to wires which exit the cell for simultaneous resistance measurements as well as subsequent resistance vs. temperature measurements. A base pressure of alkali metal is obtained by heating the entire cell up to a temperature that exceeds the melting point of the alkali metal being used as the dopant. For example, if potassium is the dopant, the cell is heated to approximately 150°C. An additional heater is

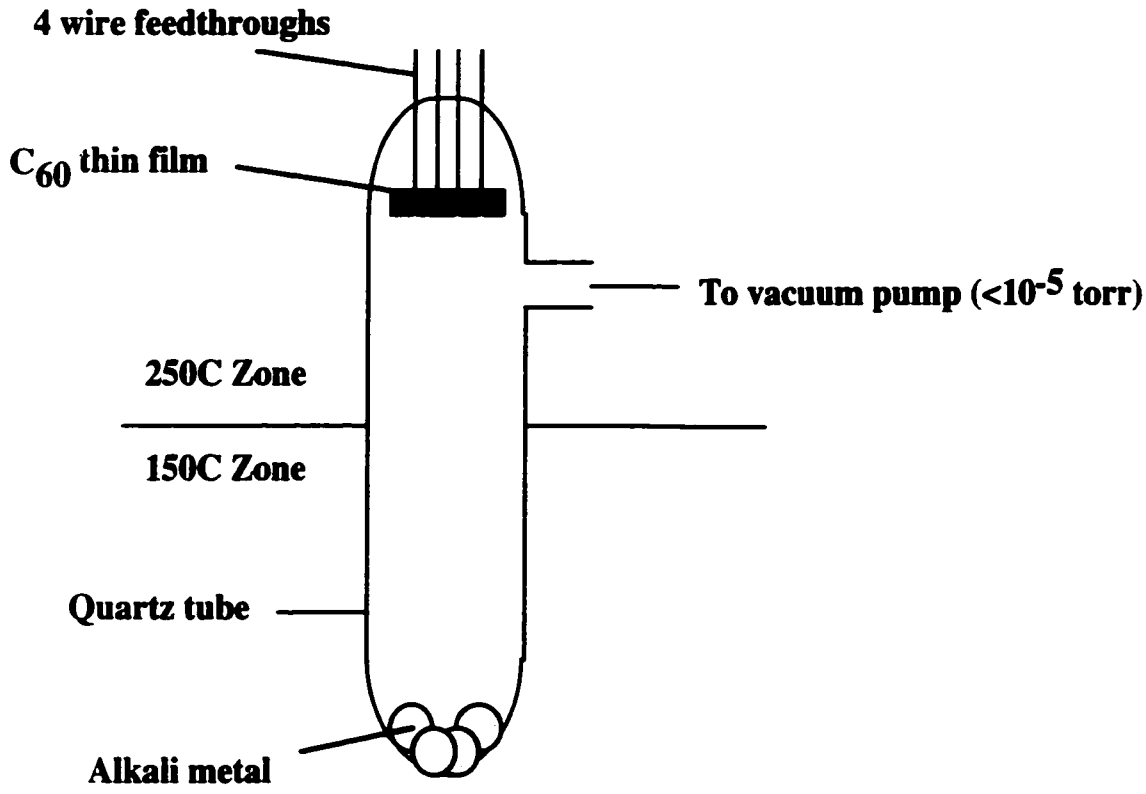

Figure 2.4: Basic design of the doping cell originally used to dope C_{60} thin films[6].

used to heat the C_{60} film to about 200-250° C. This substrate heater serves two purposes. It prevents alkali metals from condensing on the surface of the film and it anneals the film to promote uniform doping. Undoped C_{60} films are electrically insulating as is evident from the 1.5 eV band gap shown in the band structure of figure 2.3. During the alkali doping experiments, it was noticed that the conductivity of the C_{60} films increased by several orders of magnitude to a maximum conductivity, S_{max}. The value of S_{max} is shown for different alkali metal dopants in table 2.1. Further doping caused the resistance of the films to increase and return to an insulating state.

The explanation of this is that three electrons per C_{60} molecule half fills the

M_3C_{60}	T_c(K)	M_3C_{60}	T_c(K)
Li_2RbC_{60}	<2.0	K_2RbC_{60}	23.0
Na_2RbC_{60}	3.5	K_2CsC_{60}	24.0
Li_2CsC_{60}	12.0	Rb_2KC_{60}	27.0
Na_2CsC_{60}	12.0	Rb_3C_{60}	29.0
K_3C_{60}	19.3	Rb_2CsC_{60}	31.3
$K_{1.5}Rb_{1.5}C_{60}$	22.2	$RbCs_2C_{60}$	33.0
KRb_2C_{60}	23.0	Cs_3C_{60}*	40.0

* Cs_3C_{60} phase measured under pressure @12kbar

Table 2.2: A list of most of the superconducting doped phases of C_{60} in order from lowest to highest T_c. (Adapted from M. S. Dresselhaus, et. al., Science of Fullerenes and Carbon Nanotubes. (Academic Press Limited, London, 1996) P. 243)

LUMO band shifting the fermi level in line with a peak in the density of states due to the half filled band. This produces a metallic solid with the conductivity of S_{max}. Further doping completely fills the LUMO moving the fermi level into another band gap causing the solid to become insulating again. Upon the onset of the metallic state, the color of the film turned from brown to magenta.

Table 2.2 lists several of the alkali metal C_{60} phases which have been found to superconduct, along with the corresponding values of T_c. The intra-molecular phonons on the C_{60} molecule are now solely believed to be responsible for producing Cooper pairs, the charge carriers responsible for superconductivity. Therefore, the choice of alkali metal has very little effect on the electron-phonon coupling constant. However, the alkali metal

does determine the lattice constant which is inversely proportional to the band width and proportional to the density of states for the doped phases. Thus the larger alkali atoms will give a larger density of states and a higher T_c, according to equation 2.1. This argument holds provided that the crystal structure remains the same. In fact, most of these A_3C_{60} phases crystallize in a face-centered cubic (fcc) lattice until the size of the alkali metal becomes exceedingly large. For example, Cs_3C_{60} is not believed to be an fcc crystal[5].

2.7 Higher fullerenes

C_{60} wasn't the only fullerene extracted by Krätschmer, et. al.. A variety of other, higher fullerenes is also produced in the arc-discharge technique[10]. Toluene soluble fullerenes up to about C_{100} are extracted by toluene from the bulk soot, most in very low quantities. However, the presence of higher fullerenes is not as simple as a uniform distribution of molecules for every even carbon number. For some carbon numbers such as C_{62}, no fullerenes have ever been extracted or purified. Alternately, for other carbon numbers such as C_{78}, several different molecular isomers have been separated. The theory used to explain this is known as the "isolated pentagon rule"[11,12]. Fullerene structures are closed cages made up entirely of hexagons and pentagons. Euler showed that such structures require exactly twelve pentagons for closure. This rule states that the most stable fullerenes are those which have the minimum number of adjacent pentagons in the fullerene cage. Therefore, no fullerenes are extracted for C_{62}, C_{64}, C_{66} or C_{68} because its impossible to arrange a structure of pentagons and hexagons where all of the pentagons are isolated from one another in these fullerenes. In fact, C_{70} is the first carbon number greater than C_{60} where isolated pentagons are possible. The C_{70} isomer which obeys the

IPR is a slightly elongated C_{60} ball. In other words, the C_{70} molecule can be thought of as having a belt of 10 hexagons capped on either side by C_{60} halves. The abundance of C_{70} in fullerene soot after the arc-discharge is about 1% total or about 10% relative to the abundance of C_{60}.

All fullerenes above C_{70} are found only in minuscule quantities[10]. The next lowest carbon number for which fullerenes are found is C_{76} followed by three different isomers of C_{78}. Next, C_{80} has been found along with three isomers of C_{82} and two isomers of C_{84}. Unfortunately, research into the properties of these molecules has been severely limited due to the challenges of purifying macroscopic quantities. However, some basic chemical characterization has been done such as Optical Spectroscopy and Nuclear Magnetic Resonance (NMR)[10].

2.8 Carbon nanotubes

During arc-synthesis of C_{60}, the graphite anode is slowly consumed. Some of the graphite from the anode sublimes and condenses on the walls of the chamber. This is the soot from which fullerenes are extracted. In addition, some of the carbon in the anode sublimes and collects on the cathode in the form of a cylindrical growth known as a 'boule'. This boule has a hard outer shell surrounding a soft, fibrous inner core. In 1991, Sumio Iijima studied this fibrous inner core with a transmission electron microscope (TEM) and discovered multi-walled carbon nanotubes[13]. As shown in figure 2.5a, These nanotubes consist of many concentric graphite layers wrapped around one another. The spacing between neighboring concentric tubes is 3.4 angstroms, the same as the interlayer spacing in crystalline graphite. Although these tubes are only nanometers in diame-

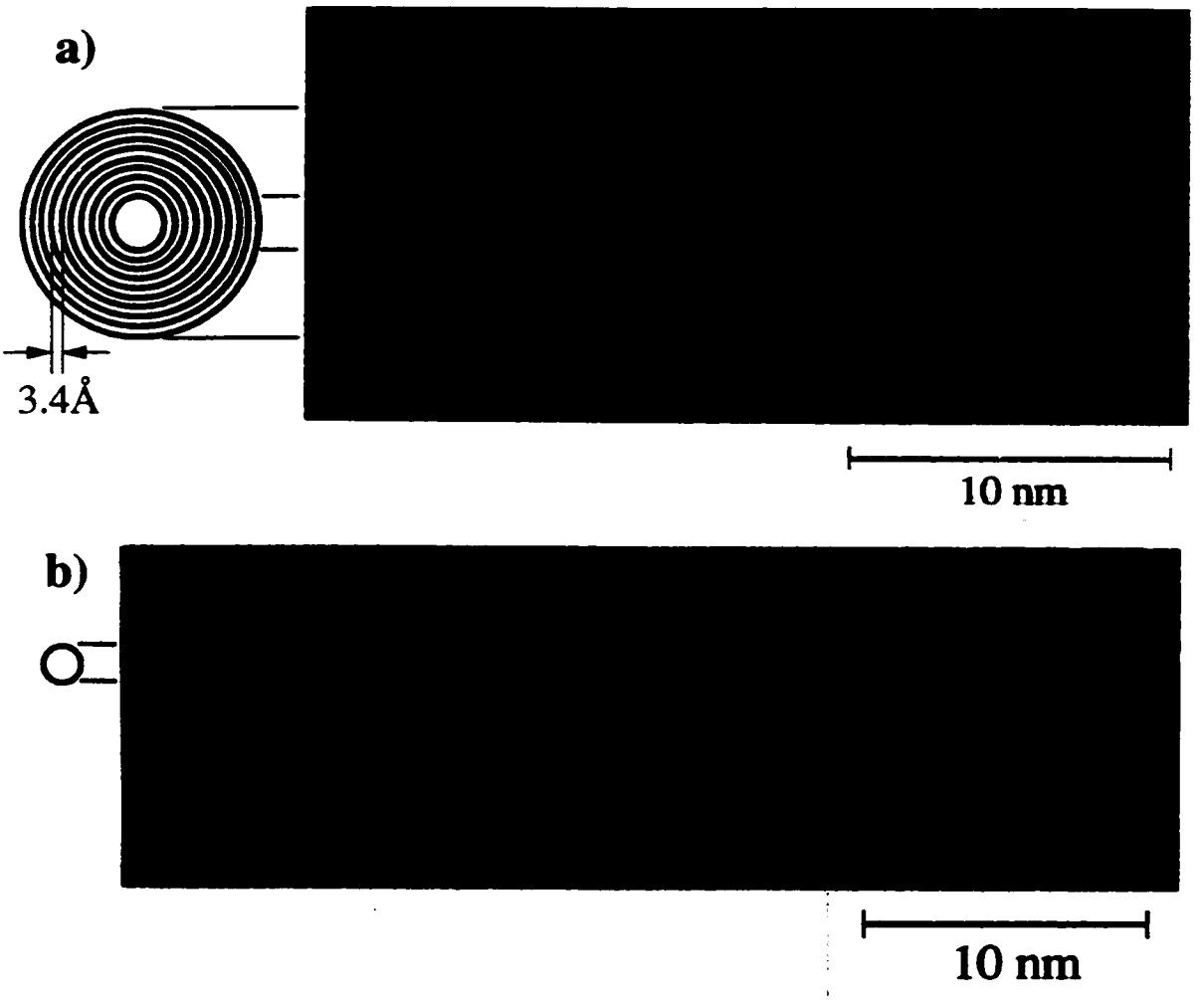

Figure 2.5: Transmission electron micrographs of a) a multi-walled carbon nanotube and b) a single-walled carbon nanotube. (Adapted from Ref. [30])

ter, they can be up to hundreds of microns long.

2.9 Nanotube synthesis

Carbon nanotubes are now commonly synthesized by three very different techniques. These are electric-arc discharge[14,15], laser ablation[16,17] and chemical vapor deposition (CVD)[18-21]. Most of the details of arc-discharge synthesis are identical to the C_{60} production scheme described above, although some minor details are slightly different. For example, optimum nanotube growth is achieved at 650 torr Helium pressure as

opposed to optimum C_{60} growth which occurs at 100 torr Helium pressure. Soon after the discovery of carbon nanotubes, a procedure for arc-synthesizing single-walled nanotubes was found almost simultaneously by Iijima, et. al.[22] and by Bethune, et. al.[23]. In the latter work, this discovery was made while experimenting with packing the graphite anode with cobalt in hope of trapping ferromagnetic atoms of cobalt inside fullerenes. After arcing the composite anode against a graphite cathode, the chamber was full of a rubbery, web-like material, in addition to the boule on the cathode which contained typical multi-walled nanotubes and the soot on the walls which contained fullerenes. A TEM study of this web-like material revealed entangled single-walled nanotubes encompassing cobalt nanoparticles. A TEM micrograph of a typical single-walled nanotube is shown in figure 2.5b. These nanotubes have a diameter of approximately 1.2 nanometers, significantly smaller than a typical multi-walled nanotube. Also, the diameter distribution of the tubes is sharply peaked, as opposed to multi-walled tubes which cover a wide range of diameters.

Another method of synthesizing carbon nanotubes involves laser ablation of a graphite target. Just as with arc-synthesis, laser ablation of a pure graphite target produces multi-walled tubes while laser ablation of a graphite composite containing cobalt and nickel catalysts produces single-walled nanotubes. The single-walled tubes synthesized by this method close-pack together into bundles of several hundred tubes. This method has been refined to produce very high purity single-walled nanotubes[16]. As shown in figure 2.6, the experimental setup consists of a one inch diameter quartz tube placed in a 1200 C oven. The graphite composite target containing 1% nickel and 1% cobalt is positioned near the end of the oven. The target is ablated with either one or two Nd:YAG

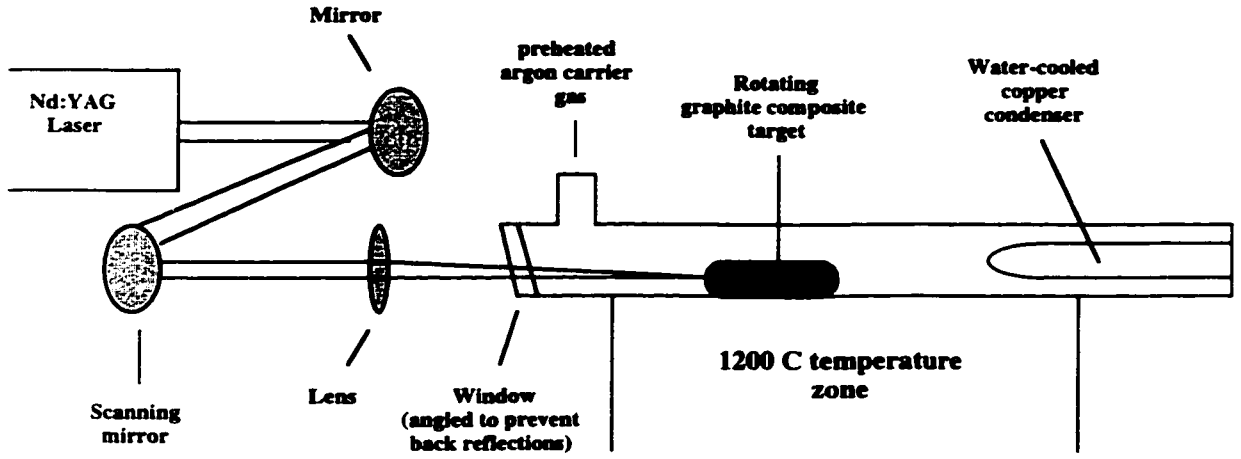

Figure 2.6: Schematic of the laser ablation setup for producing high purity single-walled carbon nanotubes.

pulsed lasers operating at about 300-1000 millijoules per pulse. The frequency of the first laser's pulse is doubled to 532 nm while the second laser's pulse, which trails the first by tens of nanoseconds, has the wavelength of the laser's natural harmonic, 1064 nm. The purpose of the first laser is to ablate the sample while the second laser anneals the plume. A preheated argon gas flow carries the plume through the oven for further annealing before finally collecting on a copper condenser on the other end of the tube. The laser is designed to raster over the target so that the surface remains smooth. When optimized, this technique has been shown to produce high quality single-walled carbon nanotubes at a purity of approximately 90%. However, yield and purity are very sensitive to several parameters making reproducibility difficult.

The third most common technique for producing carbon nanotubes is by chemical vapor deposition (CVD)[18-21]. Here, a transition metal catalyst such as cobalt, nickel or iron is chemically prepared in the form of nano-sized islands supported on a substrate, usually alumina or silica. This catalyst bed is placed in a quartz tube inside a tube furnace that can be heated between 600 and 1200 C. Once at high temperature, a hydrocarbon

such as methane, ethylene or acetylene is allowed to flow through the oven. The hydrocarbon breaks down on the surface of the catalyst and the carbon dissolves in the metal forming a molten metal carbide solution. As more carbon is added to the catalyst particle, the carbon solution becomes saturated and a graphite coating begins to precipitates on the surface. This coating grows away from the catalytic particle in the form of a single-walled carbon nanotube. Parameters such as the size of the catalyst, the type of hydrocarbon used and the temperature of the oven determine if this technique produces single-walled tubes, multi-walled tubes, amorphous carbon filaments or carbon fibers.

2.10 Carbon nanotube theory and applications

Carbon nanotubes are of interest for several unique electronic and mechanical properties. Perhaps the most interesting property of a nanotube is that it can be either semiconducting or metallic, depending on the exact diameter and chirality of the molecule[24-27]. This is due to the fact that there are only discrete k-points in the graphite Brillioun zone which cross the fermi level. Also, the allowed k-points for a nanotube is significantly reduced by the boundary condition that require the electronic wave function to repeat for every complete rotation about the nanotube's circumference. If this reduced set of k points includes a k-point at the fermi level, the tube is metallic. However, if this is not the case, the tube is semiconducting with a band gap determined by the closest k-points above and below the Fermi level.

The fact that carbon nanotubes have such diverse electronic properties opens up a world of possibilities in the field of nanoelectronics. Perhaps the most basic problem that nanotubes solve is how to fabricate a metallic nanowire. Metallic nanotubes may be the smallest, free-standing, metallic wires possible. Also, nanotubes with different chiralities

can be joined together with the addition of a certain type of defect consisting of a five fold ring fused to a seven fold ring. If this junction connects a metallic tube to a semiconducting tube, the result is a nanoscale Schottky diode with a rectifying current-voltage characteristic[28-30]. Although it may take years until the technology is developed to fabricate such a device, these diodes have already been shown to exist in bulk samples of single-walled nanotubes[31,32]. Usually these junctions can be seen in TEM images as sharp kinks in a single-walled nanotube.

Other favorable properties of carbon nanotubes includes the high strength that nanotubes exhibit along the axial direction. This is due to the fact that the sp^2 carbon bond is one of the strongest in nature. The Young's modulus of a carbon nanotube has been measured to be on the order of 1 TPa[33,34]. This suggests that nanotubes may some day be a key ingredient in the fabrication of ultra high strength composites. Another useful property of nanotubes involves electronic field emission. Nanotubes have been shown to have excellent field emission characteristics due to the nanometer scale radius of their tips[35-39].

2.11 Lower fullerenes

Lower fullerenes refer to the set of all caged carbon structures comprised of hexagons and pentagons with less than sixty carbon atoms. According to the book, 'An Atlas of Fullerenes', 512 of these structures are mathematically possible[40]. Since the discovery and isolation of C_{60} and higher fullerenes, there has been much speculation by theorists on the stability of lower fullerenes. From figure 2.1, it is evident that carbon clusters with less than sixty atoms have been produced in the Smalley laser ablation system. However, it is not known whether these clusters are chains or rings of carbon or fullerenes.

Theorists predict that rings and chains of carbon are the most stable structures below C_{20} while tangled poly-cyclic structures are most stable in the range between C_{20} and C_{30} and fullerenes are most stable above C_{30}[41].

Despite the observation of these molecules in the mass spectra, lower fullerenes were not isolated in the original graphite-arc technique that produced C_{60}[3]. This could be due to a number of reasons. One possibility is that all of the lower fullerenes are unstable molecules and thus cannot be formed under any condition. Another possibility is that the exact conditions under which C_{60} is made may not be optimal for lower fullerenes. Such parameters include the type of buffer gas used and the pressure of the buffer gas in the arc-chamber. Lower fullerenes may even require a completely new synthesis technique such as laser ablation or flame synthesis. A third possible explanation is that the chemical properties of lower fullerenes may be very different from higher fullerenes. For example, lower fullerenes may not be soluble in the same solvents as higher fullerenes. This would prevent these fullerenes from being extracted and isolated. The work discussed in the remainder of this thesis will show that the lower fullerene C_{36} is stable and does require special synthesis methods and handling techniques for isolation and study.

Chapter 3.

Carbon 36

3.1 Nitrogenated fullerenes

Our investigation of lower, pure carbon fullerenes arose from a joint experimental/ theoretical investigation of highly nitrogenated fullerenes. Theoretical input was provided by Professors M. L. Cohen and S. G. Louie and associates Dr. J. C. Grossman and M. Côté. As discussed in Chapter 2, the bonds in fullerenes are curved analogs of the planar sp^2 bonds in graphite. Graphite is known to accept high levels of boron and nitrogen in place of carbon atoms in the lattice. For example, materials such as BC_2N and BC_3 have been synthesized and characterized[42]. Other C_xN_y, graphite-like crystals have been synthesized but the position of the nitrogen atoms is not well ordered in the crystal lattice[43].

The term used to describe the replacement of a carbon atom in a fullerene molecule with another kind of atom is on-ball doping. In theory, nitrogen ought to be an excellent choice for on-ball doping of fullerenes. The bond angles in 3-fold coordinated nitrogen compounds such as ammonia are bent from planar due to the stable lone pair of electrons. These bond angles are very similar to the carbon bond angles in fullerenes. Previously, Wudl, et. al. succeeded in synthesizing $C_{59}N$ by replacing one of the carbon atoms on the C_{60} molecule with nitrogen[44]. This replacement was done using standard, wet chemistry methods starting with samples of pure C_{60}. One could argue that this procedure is even more complicated than the synthesis of the C_{60} starting material. Certainly,

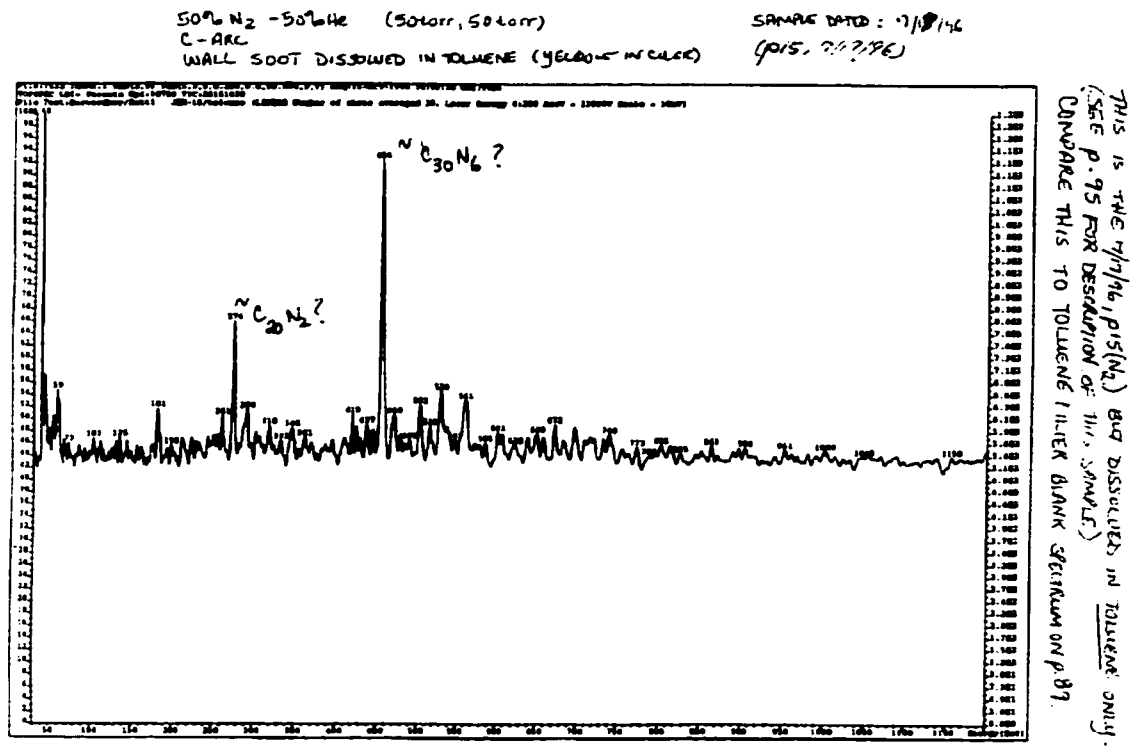

Figure 3.1: Notebook page (JBH notebook #1) showing mass spectrum of graphite sublimation product formed in nitrogen. The major peak was preliminarily assigned to $C_{30}N_6$

the further addition of nitrogen atoms to specific sites relative to the first nitrogen atom and the purification of such molecules seems nearly impossible. A simpler alternative might be to have nitrogen present during fullerene growth and allow the most energetically favorable carbon-nitrogen fullerenes to form. This method has the possible advantage of producing nitrogen doped fullerenes, other than Buckminsterfullerene, that may only be stable with nitrogen doping. Motivated by theoretical suggestion, a series of these types of experiments was performed.

The standard arc chamber described in section 2.3 was filled with a mixture of 50

torr N_2 and 50 torr He gas. A 6 mm diameter graphite rod was arced against a grounded 12 mm rod using a voltage of 20-30 volts and a current of approximately 100 amperes. The entire rod was sublimed by maintaining an arc gap of about 1-2 mm. Afterwards, the chamber was opened and the sublimation product was scraped from the walls. This product was sonicated in toluene to determine if any toluene soluble species were present. After filtration, it appeared as though some of the soot did dissolve in the toluene. This toluene soluble fraction was concentrated and run on the chemistry department's Laser Desorption/Ionization Time of Flight (TOF) Mass Spectrometer. The spectrum is shown in figure 3.1.

This mass spectrum shows a very strong peak at 454 amu. This peak was believed to be due to some lower fullerene with a high level of nitrogen doping. While investigating possible 36 atom caged structures with ball and stick models, one structure stood out as being highly symmetric. The structure, shown in figure 3.2 with nitrogen doping, con-

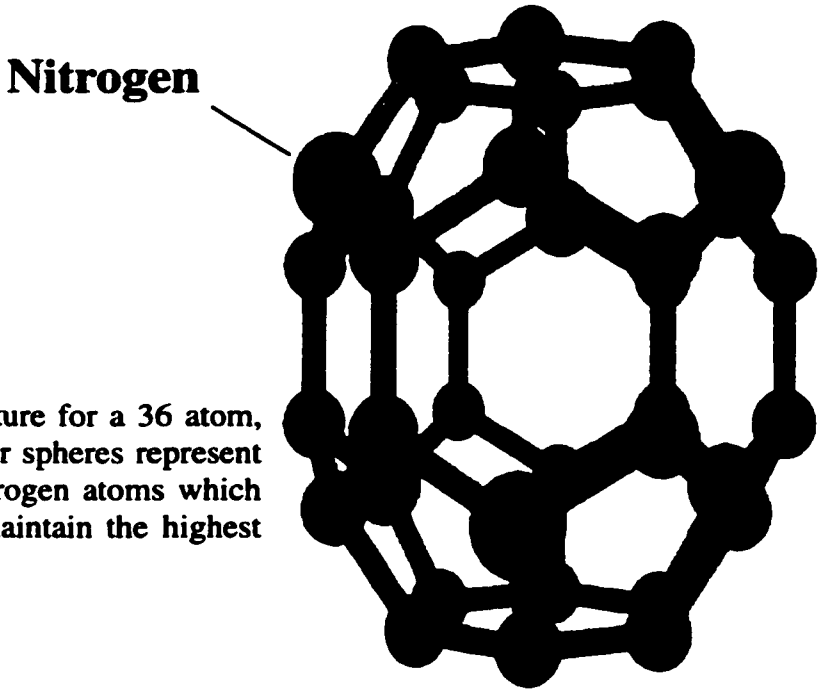

Figure 3.2: Proposed structure for a 36 atom, caged molecule. The larger spheres represent the proposed sites of 6 nitrogen atoms which have been spread out to maintain the highest level of symmetry possible.

sists of hexagonal faces on the top and bottom and a belt of six hexagons running around the middle. These hexagons around the waist are connected to the top and bottom hexagons by rings of six fused pentagons. The symmetry of the pure carbon C_{36} molecule with this structure is D_{6h} because the vertical (z) axis has six fold symmetry and a mirror plane lies in the x-y plane running through the middle of the molecule. The larger spheres in figure 3.2 represent proposed locations of 6 additional nitrogen atoms with maximum separation.

In parallel with experimental investigations, the theoretical arm of this project investigated the C_{36} molecule as well as various nitrogen doped analogs such as $C_{30}N_6$ and $C_{24}N_{12}$. One of the most promising calculations performed by Grossman, et. al. was of the electron-phonon coupling constant in the C_{36} molecule. This was found to be much larger than in the C_{60} molecule. From equation 2.1, this suggests that a properly doped C_{36} solid could be superconducting at high temperatures. The details of these calculations will be presented in the next chapter.

3.2 Synthesis of C_{36}

Motivated by the promising theoretical results on C_{36}, a technique was developed to synthesize bulk quantities of this fullerene with no nitrogen doping. Like other fullerenes in the range between C_{20} and C_{50}, C_{36} had been detected in mass spectra taken during graphite laser vaporization experiments[45]. However, these were all vapor phase experiments confined to a high vacuum chamber. No one had ever produced bulk quantities of a fullerene smaller than C_{60} and extracted them under ambient conditions.

Starting with the standard Krätschmer-Huffman arc-synthesis method, 6 mm

graphite rods were sublimated under a variety of helium pressures ranging from 50 torr to 1400 torr. All other parameters were kept the same as in C_{60} production (see section 2.3). At each pressure, a mass spectrometry probe was placed in the chamber behind a closed shutter. After the graphite arc was initiated and sufficiently stable, the shutter was opened and a thin film of carbon coated the target. The target was subsequently removed and placed in the TOF mass spectrometer for analysis. This spectrometer was operated by J. O'Lear in the College of Chemistry's Mass Spectroscopy Facility. Figure 3.3a shows the mass spectrum obtained from graphite evaporated at 400 torr helium pressure[46]. As expected from carbonaceous soot, this spectrum is full of peaks that are most likely due to fragments of higher order carbon clusters and amorphous carbon. These fragments are broken off as the mass spectrometer's laser desorbs material from the film. Above this noise, two very prominent peaks can be observed. One is for C_{60} and the other for C_{36}. This spectrum provided strong evidence that a 36 carbon atom' fullerene was present in soot evaporated at 400 torr helium and the next step was to develop a method of isolating this material.

The first step of this purification process was to extract C_{60} and higher order fullerenes from the soot with toluene. The soot was loaded into a standard Soxhlet extractor and toluene was refluxed through the soot for several hours until the toluene running out of the extractor was colorless. A mass spectrum taken on the toluene soluble portion revealed no C_{36}. Next, the soot was dried under vacuum and ground to a fine powder. At this point, the strategy was to evaporate C_{36} which should have a relatively high vapor pressure from the graphite and amorphous carbon which has almost no vapor pressure below 2000°C.

A small amount of the powder was loaded into the tungsten filament of a thermal evaporator. A mass spectrometry target was suspended 5 cm above the tungsten filament and the chamber was pumped down to $<10^{-6}$ torr. Next, the tungsten boat was rapidly heated to approximately 1500°C for about 20 minutes. A thin film coated the target which was subsequently analyzed in the same mass spectrometer. The mass spectrum of this film is shown in figure 3.3b. This spectrum contains one major peak at 438 amu, 6 amu higher than the mass of C_{36}. This extra mass could be explained by a number of possibilities. The most likely explanation is that the extra mass is due to the molecule becoming partially hydrogenated either by a reaction with steam during the high temperature evaporation step or with hydrogen desorbed from the stainless steel surface during the laser desorption/ionization step in the mass spectrometer.

3.3 Predicting which fullerenes will form

The term "lower fullerene" refers to any pure carbon-caged molecule with hexagonal and pentagonal faces in the mass range between C_{20} and C_{60}. The compelling evidence that bulk quantities of C_{36} have been synthesized begs the question of why the Krätschmer-Huffman arc technique produces this fullerene in significant quantities over the 511 other lower fullerenes[40]. One way to begin answering this question is to look at which lower fullerenes are the lowest in energy and, therefore, most likely to be stable. Kroto proposed a set of simple, empirical arguments for determining the most stable fullerene[11]. The first argument is the molecule's stability is inversely related to the number of adjacent pentagons in the structure. Secondly, stability is directly related to the degree of symmetry of a fullerene. The reasoning is that the strain resulting from the bent sp^2 bonds is better distributed in fullerenes with high symmetry. The third condition is

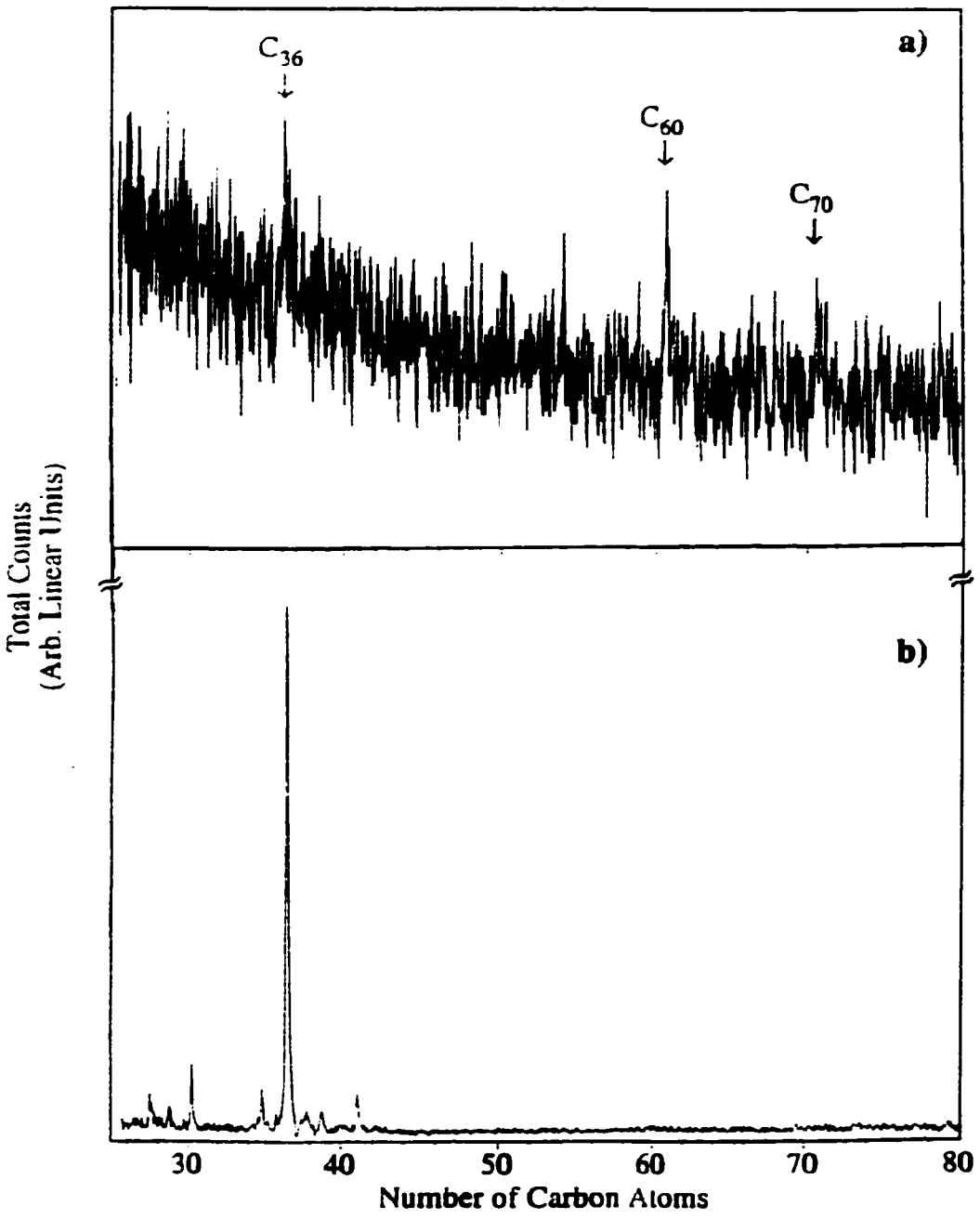

Figure 3.3 a) Mass spectrum of raw soot from graphite arc at 400 torr He. Among the peaks rising above the noise level is C_{36} along with the well known fullerenes, C_{60} and C_{70}. b) Mass spectrum of a film evaporated from the soot of figure 3.3a after C_{60} and higher fullerenes had been extracted with toluene. Spectra are courtesy of J. O'Lear and the College of Chemistry's Mass Spec. Facility. (Adapted from Ref. [46])

that fullerenes with closed electronic shells are more stable than open-shelled fullerenes.

Figure 3.4 shows simple diagrams of all 15 possible fullerene isomers for C_{36}[40]. The table included in the figure lists the symmetry point group and the predicted Nuclear Magnetic Resonance (NMR) pattern. The NMR pattern indicates the number of non-equivalent carbon atoms in the structure. For example, isomer 36:4 has the NMR pattern 6X1, 15X2. This means there are 6 nonequivalent sites all occupied by a single carbon atom and 15 nonequivalent sites all occupied by two carbon atoms. In general, higher symmetry structures have the lowest number of nonequivalent sites. Of these structures, isomer 36:14 and isomer 36:15 have the fewest number of adjacent pentagons while isomer 36:15, the pure carbon analog of the structure shown in figure 3.2, has the highest symmetry. Also, calculations have been done showing that both of these molecules have a closed electronic shell. Therefore, isomer 36:15 fulfills all of the above requirements when compared to other C_{36} isomers. A detailed calculation by Grossman, Côté, Cohen and Louie using a pseudopotential density functional method did find isomer 36:15 to be the lowest energy C_{36} structure. However, isomer 36:14 which differs from 36:15 by a single bond rotation is isoenergetic (see chapter 4).

The most energetically favorable isomer of C_{36} has now been determined, but this doesn't explain why C_{36} production is favored over C_{32}, C_{34}, C_{38}, C_{40}, etc.. From an energetics standpoint, larger fullerenes are generally more stable than smaller fullerenes due to the reduction in curvature. For example, the most energetically favorable isomer of C_{44} is lower in energy than isomer 36:15[47]. Therefore, if energetics were the only factor determining fullerene production, one would expect a distribution of lower fullerenes to be produced with a yield that increases with carbon number.

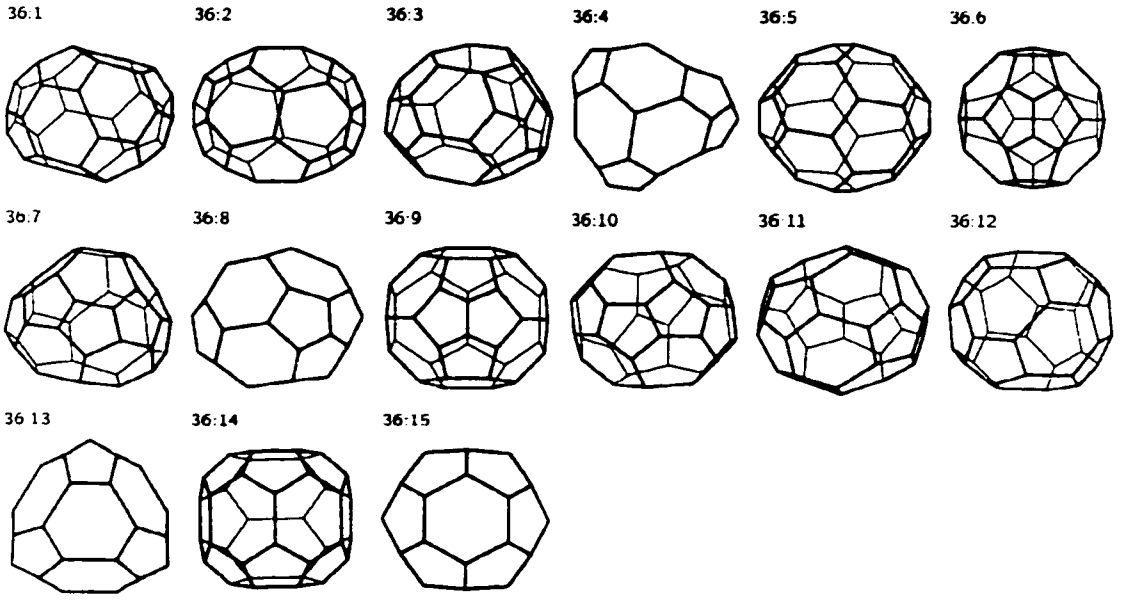

Isomer	Point group	NMR pattern	Isomer	Point group	NMR pattern
36:1	C_2	18X2	36:9	C_{2v}	4X2,7X4
36:2	D_2	9X4	36:10	C_2	18X2
36:3	C_1	36X1	36:11	C_2	18X2
36:4	C_s	6X1,15X2	36:12	C_2	18X2
36:5	D_2	9X4	36:13	D_{3h}	2X6,2X12
36:6	D_{2d}	3X4,3X8	36:14	D_{2d}	1X4,4X8
36:7	C_1	36X1	36:15	D_{6h}	3X12
36:8	C_s	4X1,16X2			

Figure 3.4: Pictures of all possible C_{36} isomers consisting exclusively of pentagons and hexagons. The table shows the symmetry point group along with the predicted nuclear magnetic resonance (NMR) pattern. The first number represents the number of non equivalent carbon atoms while the second number shows how many carbon atoms share each chemically equivalent site. (Adapted from Ref. [40])

Obviously, if C_{36} is the dominant lower fullerene, kinetics must also play a role in the arc synthesis of lower fullerenes. Currently, there are two major growth models for fullerenes, the pentagon road[48] and the fullerene road[49]. In the pentagon road model, fullerenes begin as small graphite sheets that grow by adding carbon atoms to their edges. Closure occurs through the random formation of pentagons in the sheet which are favored over dangling bonds. The fullerene road model assumes that all fullerenes begin as lower fullerenes around C_{30}. These lower fullerenes grow by absorbing carbon atoms from the vapor and annealing to redistribute the pentagons into the most thermodynamically stable structure. Neither of these theories sufficiently account for a relatively high abundance of C_{36}.

3.4 Clathrin

A certain type of protein known as clathrin serves as an excellent model for predicting the behavior of fullerenes and nanotubes. Clathrin is a long, rigid molecule with a molecular weight of about 180,000 a.m.u.. It is observed to link together into a hexagonal, graphite-like network on the surface of vesicles inside various animal cells[50]. Normally, clathrin coats flat surfaces with a graphite-like, hexagonal lattice. However, it does tend to wrap around spherical vesicles by forming pentagons similar to the way carbon forms fullerenes. Also, clathrin mimics the various chiralities and end caps of carbon nanotubes when coating cylindrical vesicles.

Figure 3.5 shows a chart of several "fullerene like" clathrin structures that have been observed in various animal cells. The truncated icosahedron found in brain cells has the same structure as buckminsterfullerene. Larger clathrin structures such as the analog for C_{82} is an isolated pentagon structure identical to the isomer of C_{82} that has been syn-

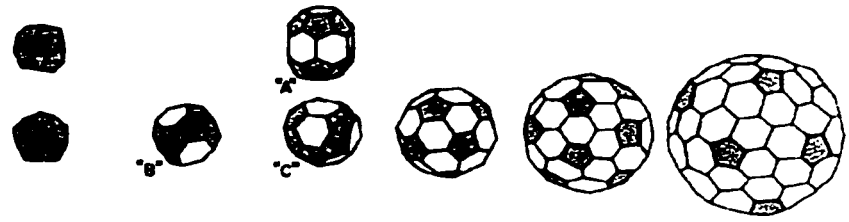

	Dodecahedron	Type "B"	Types "A" and "C"	Truncated icosahedron (brain)	(Liver)	Full icosahedron (fibroblasts)
No. of hexagons	0	4	8	20	30	60
No. of vertices	20	28	36	60	82	140
Predicted diameter (nm)	40	50	60	76	90	120
Predicted weight (MD)	13	18	23	38	53	77
No. of "facets" in deep etch	3–4	4–5	7–8	10	14	24
No. of "spikes" in neg. stain	4–5	5–6	6–8	8	12	16–17

Figure 3.5: A chart showing the most common spherical clathrin molecules observed. Structures "A" and "C" are analogs of the two lowest energy C_{36} isomers (36:15 and 36:14). Also present are analogs of well known fullerenes. The Truncated icosahedron is C_{60} and the structure to the right is C_{82}. (Adapted from Ref. [50])

thesized in limited quantities. The fact that clathrin structures which are analogs of higher fullerenes have only been observed with isolated pentagons leads to the conclusion that clathrin structures must be under the same curvature constraints as fullerenes. These molecules seem to be arranging in ways that minimize and distribute the strain that results when the hexagonal network deviates from planarity.

Given the consistency with which clathrin molecules match higher fullerenes, one should expect similar consistency between clathrin and lower fullerenes. Although there are 512 possible lower fullerene-like structures, clathrin is only known to form 4 of these structures. These are analogs of C_{20} (Dodecahedron), C_{28} (Type "B") and two isomers of C_{36} (Types "A" and "C"). Sure enough, the isomers of C_{36} are the two that were predicted

to be lowest in energy by Grossman, Côté, Cohen and Louie. Type "A" is identical to isomer 36:15 and type "B" is identical to isomer 36:14 in figure 3.4. Although it would be difficult to make quantitative arguments about the formation of C_{36} by this comparison, Clathrin does seem to indicate that nature has a preference for these C_{36} isomers just as it does for buckminsterfullerene.

Chapter 4.

C_{36} theory

4.1 Introduction

This chapter summarizes the theoretical work performed by Grossman, Côté, Cohen and Louie on the structure, stability, electronic properties and bonding characteristics of C_{36}. The chapter is divided into several sections. The first section shows calculations done to characterize the C_{36} monomer. This includes calculations on the most stable isomers and the predicted electronic structure of these isomers. The second section looks at the reaction pathway and intermolecular bonding of C_{36} dimers and trimers. Section 3 extends these calculations into the predictions for the most stable continuous solids of C_{36} and their electronic properties including the possibility of high temperature superconductivity. Finally, the last section summarizes predictions made on doped C_{36} molecules. This includes substitutional doping with nitrogen to $C_{24}N_{12}$, endohedral doping such as $Mg@C_{36}$ and C_{36} Molecules and interstitial doping as in the case of Na_2C_{36}.

4.2 C_{36} molecule

A molecule comprised of 36 carbon atoms could have a variety of possible structures. Grossman, et al. chose to investigate 6 of these structures which appeared inherently stable[51]. Of these structures shown in figure 4.1, four are fullerenes, one is a bowl

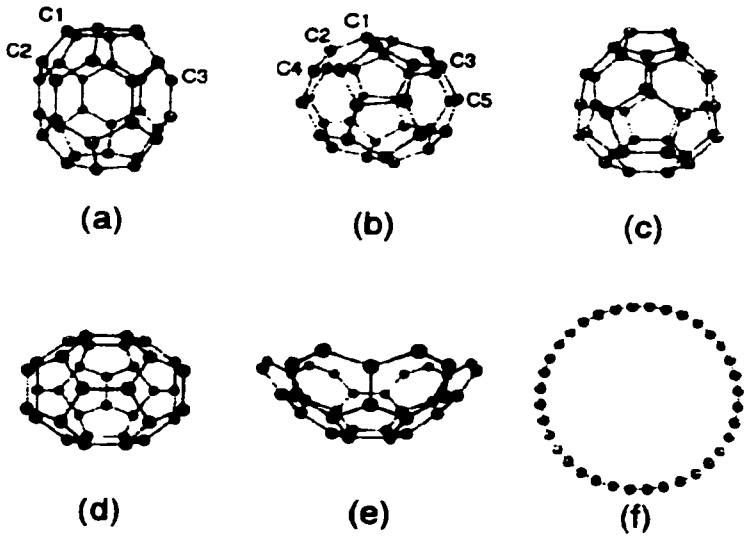

Figure 4.1: Six isomers of C_{36} investigated by Grossman, et. al.. These are fullerenes with (a) D_{6h}, (b) D_{2d}, (c) C_{2v} and (d) D_{3h} symmetry, (e) a C_{3v} bowl and (f) a D_{18} ring. Adapted from Ref. [51]

and one is a ring. The four fullerenes were chosen because they are either the most symmetric or they possess the fewest number of adjacent pentagons of the fifteen possible C_{36} fullerene isomers[40]. Grossman, et. al. used two computational methods to calculate the lowest energy structures. These were the Local Density Approximation (LDA) and the Generalized Gradient Approximation (GGA). Both methods were in agreement that the lowest energy structures were the D_{6h} and D_{2d} fullerenes, which are isoenergetic. LDA was also used to calculate the energy gap between the highest occupied molecular orbitals (HOMO) and the lowest unoccupied molecular orbitals (LUMO). This was found to be .5 eV for the D_{6h} isomer and .4 eV for the D_{2d} isomer.

Although the D_{6h} and D_{2d} symmetry isomers are isoenergetic, Côté, et. al. chose to focus on the D_{6h} symmetry isomer for a number of reasons all relating to it's higher symmetry[52]. One reason is that the six fold symmetry about the molecule's long axis makes

it ideal for forming close-packed solids. Secondly, the higher symmetry leads to more degeneracy among the electronic energy levels which could potentially produce solids with very large peaks in the density of states. If the Fermi level happened to lie on one of these peaks, the C_{36} based solid would be an excellent metal and could possibly exhibit superconductivity. Grossman, et. al. found the fully relaxed D_{6h} C_{36} structure to be 5.2 Å high and 4.9 Å wide as measured from the atom's positions. The details of the structure are discussed in section 3.1 and shown in figure 3.1.

Côté, et. al. also used LDA to calculate the symmetry, degeneracy and energy levels of the molecular orbitals for the D_{6h} fullerene[52]. They found the HOMO to be a singlet state with B_{1u} symmetry that is filled with 2 electrons. However, the second HOMO level, a doublet state with E_{1g} symmetry is nearly degenerate with the HOMO. Other computational methods have shown the lowest energy state of C_{36} to be the D_{6h} isomer where the HOMO is a partially filled triplet state[53].

4.3 C_{36} dimers

Because of the high curvature of the C_{36} molecule, it is expected that certain carbon atoms on the molecule will be highly reactive and will tend to form covalent bonds with neighboring molecules. Researchers in professor Cohen and professor Louie's group investigated several dimer and trimer configurations to determine which would be the most energetically favorable[54]. Figure 4.2 shows three of these dimers and one of the trimers that were studied along with the reduction in the total energy of each C_{36} molecule due to dimer formation. The dimer with D_{2h} symmetry was found to reduce the total

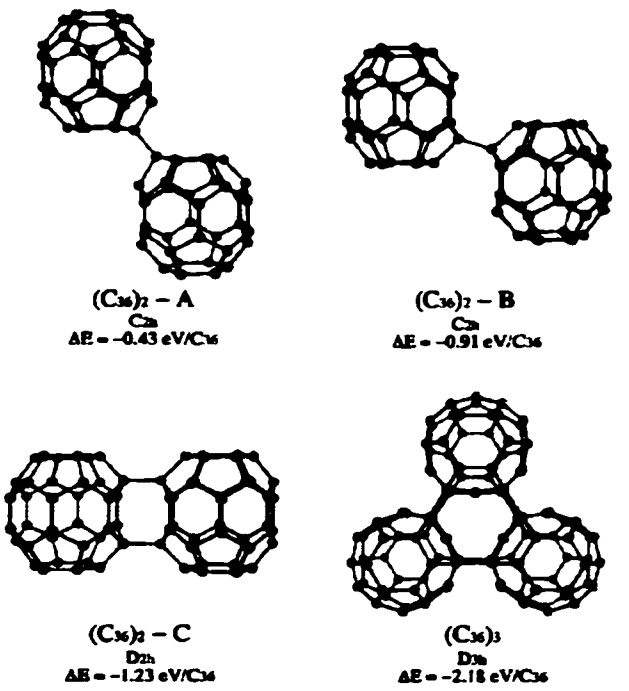

Figure 4.2: Several dimers and one of the trimers studied by Grossman, et. al.. The binding energy is listed below each dimer in terms of eV/C_{36} relative to the unbonded molecules. Adapted from Ref. [54]

energy of the molecule by the largest amount, 1.23 eV/C_{36}. This result was confirmed by Jagadeesh, et. al. using an ab initio approach[53]. They found that the intermolecular bond distance to be 1.59 Å which is in excellent agreement with the result of 1.56 Å found by Collins, et. al.[54].

Additionally, Grossman, et. al. studied the reaction pathway to dimer formation to determine if these molecules could ever be stable at the van der Waals distance[55]. To do this, the positions of the four carbon atoms involved in the intermolecular bonds were constrained at various distances along the direction of the reaction coordinate. At each point, the structure was relaxed and the total energy of the system was calculated relative to the energy of the two molecules at an infinite separation. This calculation was performed for both neutral C_{36} molecules as well as C_{36}^{-1} anions. Figure 4.3 shows the

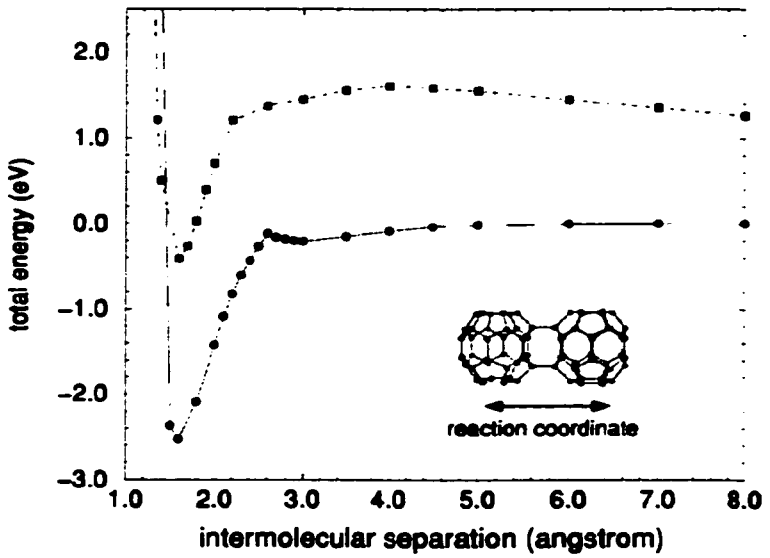

Figure 4.3: Reaction pathway for two neutral C_{36} molecules (lower curve) and two C_{36}^{-1} anions (upper curve). Adapted from Ref. [55].

results of these calculations. In the case of neutral C_{36} molecules, there is no barrier to the formation of the dimer. Although there is a small local maxima at approximately 2.6 Å, this peak is below the energy of the isolated molecules. Thus it is too low to act as a potential barrier. This is in great contrast to C_{60} for which a similar calculation was performed. C_{60} was found to have a potential barrier of 2.2 eV at the van der Waals distance.

The upper curve in figure 4.3 shows the results of the same calculation on C_{36}^{-1} anions. Here, there is a significant barrier to polymerization, but no stable minimum at the van der Waals distance of approximately 3 Å. This curve has been interpreted as being a modification of the lower curve by the electrostatic interaction of the extra electrons on each fullerene. As one might expect, the calculations show that the center of extra charge shifts from the center of the fullerene to the side that is opposite the other C_{36} molecule. This shift increases as the reaction coordinate is reduced. This calculation was performed to compliment experiments described in section 5.2 where reduction of C_{36} with potas-

sium enabled single C_{36} molecules to be measured in a time of flight mass spectrometer. The reduction of the potential well from 2.5eV to .4 eV is consistent with the fact that it was possible to laser desorb single C_{36} molecules from a surface after doping with potassium.

4.4 C_{36} solids

Grossman, et. al. compared several crystal structures all based on two different ways that C_{36} molecules can be arranged in a plane with the long axis of the molecule oriented perpendicular to the plane[55]. These arrangements were labeled S1 and S2. Both

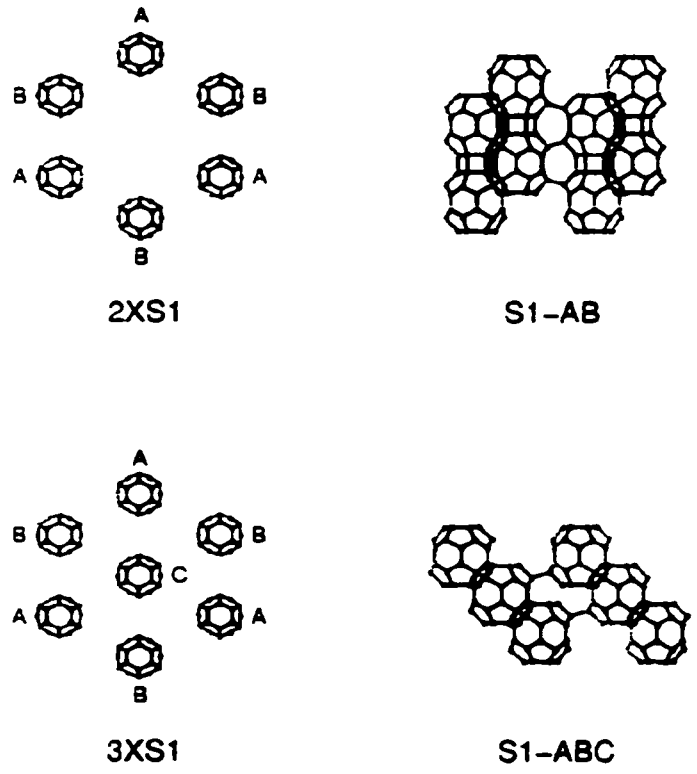

Figure 4.4: two C_{36} crystal structures proposed by Grossman, et. al. with top views on the left side and side views on the right side. The S1 planar configuration is represented by the molecules labeled A in the pictures on the left. Molecules labeled B and C represent the second and third stacking layers, respectively. Adapted from Ref. [55].

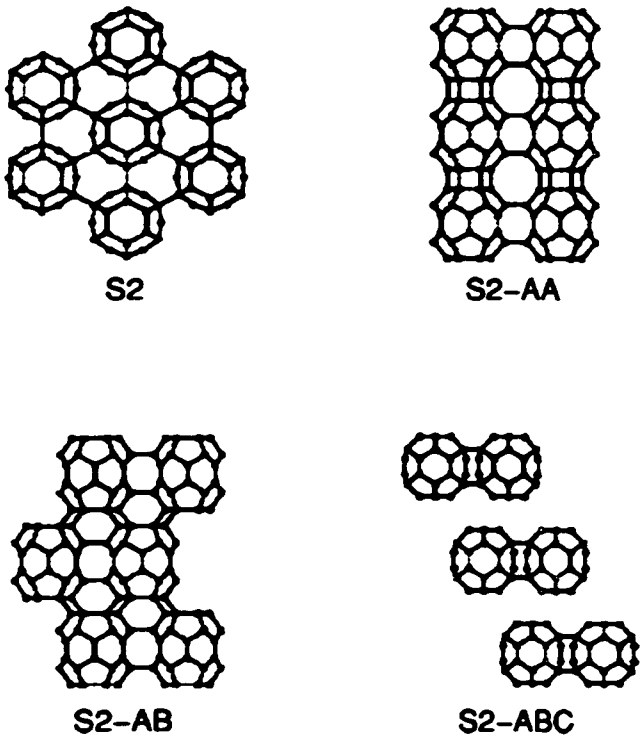

Figure 4.5: Diagram of the top view of the S2 planar configuration along with side views of three possible crystal structures studied by Grossman, et. al. based on various ways that S2 planes can be stacked. The S2-AB hexagonal structure was found to be the most energetically favorable. Adapted from Ref.[51]

arrangements have a triangular, six-fold lattice. The differerence is that in the case of S1, the molecules are sufficiently separated so that intermolecular bonds don't form between neighboring molecules in the plane. As shown in figure 4.4, this forces covalent bonds to form between molecules in neighboring planes. Originally, it was believed that the S1-ABC crystal which has a rhombohedral structure was most stable with a binding energy of 3.53 eV/C_{36}[52]. However, we later considered a rhombohedral structure based on the fully cross-linked planar configuration labeled S2 in figure 4.5[55]. The intermolecular bonds in this planar network are the same as in dimer C of figure 4.2. The rest of figure 4.5 shows three different stacking possibilities for the S2 sheets. Of these, the crystal with the highest binding energy is the S2-AB crystal which has a binding energy of 7.71 eV/

C_{36}. Grossman, et. al. proposed this hexagonally symmetric structure to be the preferred crystal structure for C_{36} molecules[55].

The electronic properties were also found to vary significantly with crystal structure. The rhombohedral structure was calculated to be metallic[52] while the proposed hexagonal structure was calculated by Grossman, et. al. to have a band gap of 0.61 eV[56]. The band structure calculation shows a large peak in the density of states approximately .3 eV above the fermi level. The presence of this level allows for the possibility of producing a metallic solid by doping this crystal with alkali metals.[55]

4.5 Superconductivity

As discussed in Chapter 2, C_{60} can be intercalated with alklali metals to produce superconducting solids with transition temperatures that exceed 40K[9]. From the argument stated in section 2.5, the increased T_c for C_{60} based solids over graphite intercalation compounds can be attributed to the curvature of the C_{60} molecule[7]. By this reasoning, smaller, more highly curved fullerenes such as C_{36} ought to superconduct at even higher temperatures.

Grossman, et. al. calculated V, the electron phonon coupling constant, from equation 2.1 in both the C_{36} and C_{60} molecules for comparison[52]. This calculation was carried out using the phonon modes and electronic states of an isolated C_{36} molecule. This procedure has been reliable in predicting T_c for C_{60} intercalated solids. However, in the case of C_{60}, the van der Waals interaction between molecules gives rise to very weak phonon modes and a very narrow broadening of molecular energy levels in the band struc-

ture of the solid[9]. It is still unknown how the covalent nature of the C_{36} crystal will modify the phonon and electronic spectra of the isolated molecule.

Côté, et. al. calculated V for all electronic states within 1 eV of the Fermi energy[52]. They found exceptionally large values of V, particularly for the second LUMO level. this doubly degenerate state with E_{2g} symmetry was found to couple to the E_{2g} phonon mode with an interaction potential (V) of 154 meV. For comparison, V was also calculated for the triply degenerate T_{1u} LUMO electronic state in C_{60} using the same computational method. This was found to couple to the H_g phonon mode with an interaction potential of 63 meV. The larger interaction potential calculated for C_{36} implies that this material may form a superconductor with a T_c greater than those found in alkali intercalated C_{60} superconductors. However, the material would first need to be intercalated with an n type donor to fill the LUMO and half fill the second LUMO with electrons. T_c could then be calculated for this compound using the Eliashburg equations which involves the following parameters: V, the electron-phonon interaction potential discussed above, μ^*, the Coulomb electron-electron interaction parameter and N(0), the density of states at the Fermi level [57]. Unfortunately, the second two parameters listed above are not currently known. In a simple approximation, values of μ^* and N(0) can be taken to be the same as in the compound K_3C_{60} which has a T_c of 18K[9,58]. From this approximation, it was found that $T_c(C_{36}) \approx 6T_c(C_{60})$.

4.6 Doping of C_{36}

Grossman, et. al. investigated three types of doping for the C_{36} fullerene: substitu-

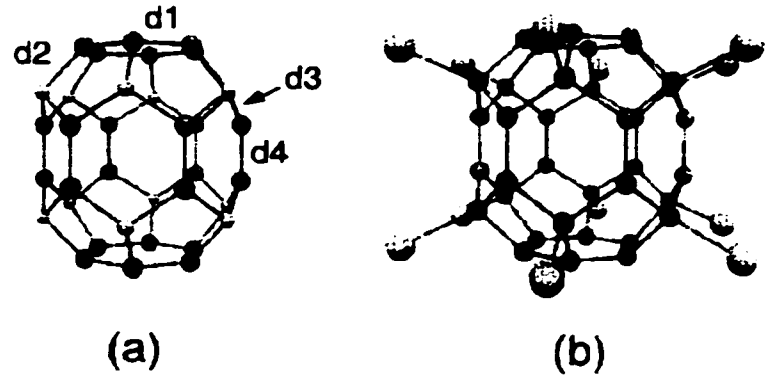

Figure 4.6: a) C_{36} D_{6h} isomer showing labels for non equivalent bonds on the molecule. The d4 bonds become shorter and stronger when C2 atoms are replaced with nitrogen. b) another way to accomplish this is by attaching chlorine to the carbon atoms at these sites. Adapted from Ref.[51].

tional, endohedral and interstitial. For substitutional doping, they studied the effects of replacing carbon atoms on the ball with nitrogen. The history of substitutional nitrogen doping of graphite and C_{60} has been covered in section 3.1. In this work, three stoichiometries were considered: $C_{34}N_2$, $C_{28}N_8$ and $C_{24}N_{12}$[51]. In each case, it was found that the most energetically favorable arrangement was also the most symmetric. Also, configurations where there were no neighboring nitrogen atoms were found to be much more stable. For example, in the case of $C_{34}N_2$ there is a decrease of 3 eV in the binding energy when the nitrogen atoms are placed next to one another on the molecule.

One interesting effect was observed in the case of $C_{24}N_{12}$. In this case, the most stable configuration was found to be the one where the 12 sites equivalent to C2 in figure 4.1 were replaced with nitrogen. This had the effect of reducing the bondlength of the carbon-carbon bond, d4, in figure 4.6 from 1.43 Å to 1.33 Å. This can be understood by using charge transfer arguments. The nitrogen atoms have excess charge which repels the charge from the carbon atoms which make up the d4 bonds. This causes more charge to pile up between these carbon atoms which increases the strength and decreases the length

	Mg	Ca	Ge	Si	Zr	Sr
ΔE ($C_{36}D_{6h}$)	+0.9	+4.7	+1.2	+1.4	+6.7	+4.2
ΔE ($C_{36}D_{2d}$)	+0.3	+4.2	+0.7	+0.9	+6.1	+4.9
$\Delta E(C_{28})^*$	-1.6	-4.5	—	-7.8	+2.8	—

Table 4.1: Binding energies, ΔE, of endohedrally doped atoms in C_{36} for both D_{6h} and D_{2d} molecules and C_{28}. Adapted from Ref.[51]

* Ref. [59]

of the d4 bond. This effect could have interesting applications. For example, it could serve to strengthen phonon modes and increase T_c in C_{36} based superconductors. Also, it could also have positive mechanical effects such as an increase in the bulk modulus. The effect was also observed when chlorine was attached to all of the C2 equivalent sites (figure 4.6).

The next type of doping explored by Grossman, et. al. was endohedral doping where atoms are trapped inside the fullerene. The standard convention for indicating that a metal, M, has been endohedral doped inside C_{36} is $M@C_{36}$. The first of this class of materials was $La@C_{60}$ discovered in mass spectrometry experiments and later in bulk quantities[60]. Table 4.1 lists the binding energy of C_{36} calculated by Grossman, et. al. with selected metal atoms trapped inside[51]. The energies are given in terms of the difference between the metal being inside and outside the cage. That is, $\Delta E = E(M) + E(C_{36}) - E(M@C_{36})$. Table 4.1 also includes similar data calculated on C_{28} by Guo, et. al. [59]. Notice that for all of the elements studied, endohedral doping is energetically favorable in both the D_{6h} and D_{2d} structures. The same cannot be said for C_{28} since only Zirconium is

favored for endohedral doping. Therefore, C_{36} appears to be unique in it's capability of trapping a broad range of elements. This property is favorable in a number of applications such as the trapping of radioactive atoms for medical diagnostics or magnetic atoms for data storage.

The third type of doping investigated by Grossman, et. al. is interstitial doping. This is the kind of doping that occurs in alkali doped C_{60} such as the superconducting K_3C_{60} phase[9]. It was noticed that the proposed S2-AB crystal structure shown in figure 4.5 has pockets of empty space both above and below each C_{36} molecule. The volume of these spaces is approximately 6.2 $Å^3$. This is large enough to accomodate Na and possibly K which have ionic volumes of 2.84 $Å^3$ and 5.56 $Å^3$, respectively.

Grossman, et. al. carried out LDA calculations to relax the structure of Na_2C_{36} and K_2C_{36}[55]. The results are shown in figure 4.7. As is clear from the figure, Na_2C_{36} was able to maintain the S2-AB structure, but K_2C_{36} underwent a structural transition due to

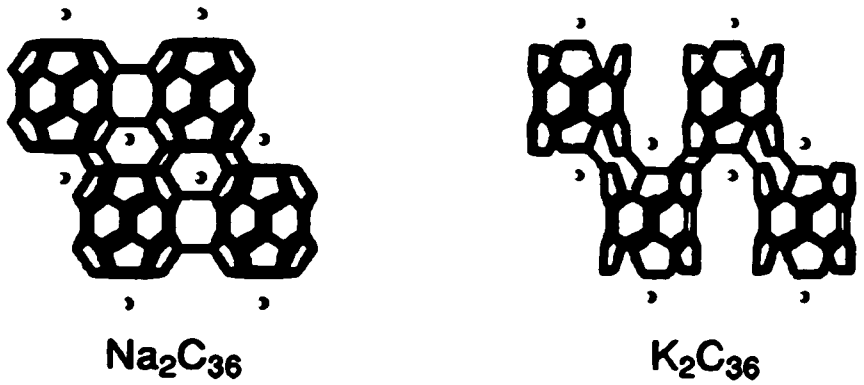

Figure 4.7: Fully relaxed C_{36} solids in the proposed hexagonal crystal structure with sodium and potassium dopants. The sodium doped crystal maintains its structure while the potassium doped crystal undergoes a structural rearrangement. Adapted from Ref.[55]

the additional strain. In this transition, the intermolecular bonds which formed the dimers in the S2 plane are broken and the ends of the molecules open up to form new intermolecular bonds between the planes.

Because Na_2C_{36} maintains the original crystal structure, the density of states for this compound was calculated to determine how the electronic structure had been modified after doping[55]. There was found to be some broadening of the energy states and, as expected, the fermi level shifted beyond what was formerly the LUMO. In the single molecule, this level is a singlet with B_{2g} symmetry. Therefore, this level is completely filled with two electrons from the two sodium atoms. The energy gap in this material was found to be only about .2 eV. Further doping will fill the next level which should lead to a metallic solid. Since this level is a doublet, two additional electrons per C_{36} would be most ideal.

4.7 Other properties of C_{36}

To help with chemical characterization and determination of the exact isomer of C_{36} that has been isolated, Grossman et. al. calculated the ^{13}C nuclear magnetic resonance (NMR) chemical shifts for the carbon atoms on C_{36} as well as the infrared (IR) active modes to be observed by infrared spectroscopy. Table 4.2 shows the calculated chemical shifts relative to tetramethylsilane[51]. The higher symmetry D_{6h} structure is expected to show 3 peaks because it has three nonequivalent carbon atoms. These peaks should all have equal intensities since for all three nonequivalent sites there are 12 carbon atoms on the molecule which occupy these sites. However, two of the three peaks are within half of a part per million (ppm). Therefore, if the peaks are broadened such as in solid state

Table 4.2: NMR shifts and normalized intensities for the two lowest energy C_{36} isomers as calculated by Grossman, et. al. The labels C1 through C5 are graphically shown in figures 1a and 1b. Adapted from Ref.[51]

molecule	atom	δ_{TMS}	intensity
C_{36} (D_{6h})	C1	137.5	1/3
	C2	159.4	1/3
	C3	160.0	1/3
C_{36} (D_{2d})	C1	151.8	1/9
	C2	160.5	2/9
	C3	150.3	2/9
	C4	139.3	2/9
	C5	135.7	2/9

NMR, these two peaks may appear as a single peak with twice the intensity. The less symetric D_{2d} isomer is expected to have 5 peaks. 4 of these peaks which are due to eight equivalent carbon atoms should all have the same intensity while one of the peaks which is due to four equivalent atoms should have half the intensity relative to the others.1

Grossman, et. al. also calculated the infrared (IR) active modes expected for both the D_{6h} and D_{2d} isomers of C_{36}. These calculations showed that the D_{2d} has 37 IR active modes while the more symmetric D_{6h} structure has only 13 in the range between 400 and 1600 wavenumbers. Figure 4.8 shows the expected IR absorption spectrum obtained by plotting the calculated peak positions and intensities and applying an artificial broadening to simulate interactions within the solid. As is clear from the figure, the D_{6h} isomer produces fewer and much more intense peaks than the D_{2d} isomer.

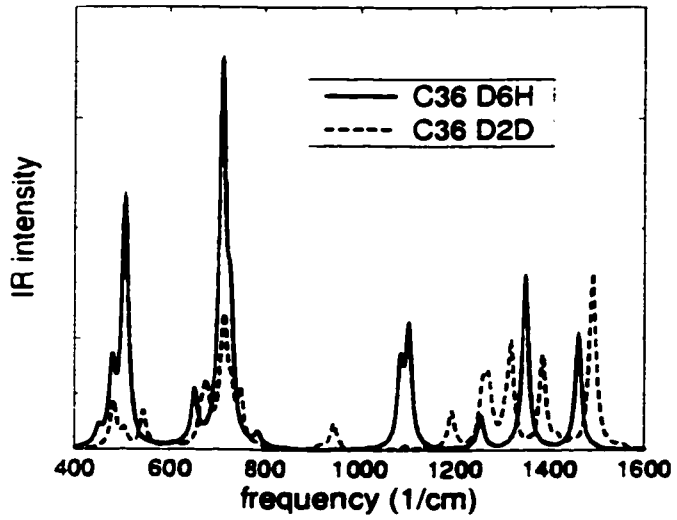

Figure 4.8: **Predicted IR absorption spectra for D_{6h} and D_{2d} symmetry isomers of C_{36}. Adapted from Grossman, Côté, Cohen and Louie, unpublished work.**

Chapter 5.

C_{36} experiment

5.1 Solubility and air sensitivity

The thin film of C_{36} grown in section 3.2 was washed in several solvents to determine solubility. The film was found to be soluble in both pyridine (C_5H_5N) and carbon disulfide (CS_2), two very polar organic solvents. The color of the C_{36} solution was yellow-brown as opposed to C_{60}/C_{70} solutions that are reddish-brown in color. Although the exact solubility of C_{36} in these solvents was never determined, it appeared to be on the order of a few grams per liter, similar to the solubility of C_{60} in toluene. As a result of this finding, bulk quantities of material containing C_{36} were produced[46]. First, the soot produced by arcing graphite at 400 torr He pressure was placed in a soxhlet extractor and higher fullerenes were extracted with toluene. Next, the extracting solvent was switched to pyridine and C_{36} was extracted. This pyridine soluble portion made up about 1% of the original soot.

Interestingly, the C_{36} material would remain in the pyridine solution indefinitely. However, if the pyridine was allowed to evaporate and the powder was dried under ambient conditions, it could not be redissolved. This is consistent with the prediction that C_{36} forms covalently bonded solids (see section 4.5). Also of concern was the possibility that atmospheric impurities could be catalyzing this irreversible polymerization. Therefore, the entire synthesis process was converted to completely eliminate air exposure.

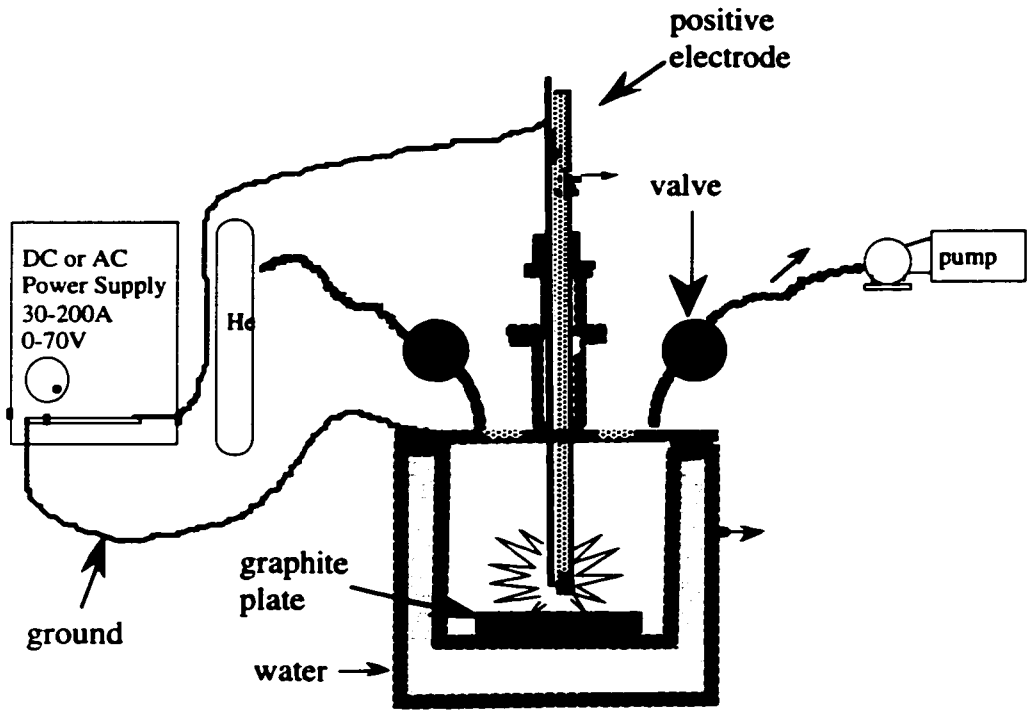

Figure 5.1: Schematic of a new arc chamber designed to be transferred into an argon glovebox prior to opening.

Figure 5.1 shows a schematic of an arc chamber that I designed to be transferred into an argon atmosphere glovebox prior to opening. This system which was built by machinists in the Berkeley Physics Department consists of an inner chamber where the arc takes place and an outer chamber which houses the water cooling bath. For the arc synthesis procedure, the inner, stainless steel chamber is bolted to an o-ring flange on the top of the outer chamber and water is circulated in the outer chamber keeping the walls of the inner chamber cool. To eliminate one of the electrodes, the stainless steel chamber is used to ground a graphite plate at the bottom of the inner chamber which provides a surface to arc the1/4 inch graphite annode against. Prior to the arc run, the graphite annode is carefully degassed by contacting the graphite plate and sending about 100 amperes through the rod with the chamber under vacuum. This procedure is continued until the pressure drops

down to the base pressure of the system. After the arc run, the inner chamber is removed from the outer chamber while keeping the inner chamber completely sealed. The valves are closed and the inner chamber is disconnected from the vacuum pump and helium cylinder. After drying the exterior, the inner chamber is then transferred into an argon glovebox. Once inside the glovebox, the inner chamber is opened and the soot is brushed into a jar for storage.

To extract fullerenes from this graphite-arc soot under inert conditions, I designed a new type of extractor which was built in the College of Chemistry's glass shop. The schematic for this extractor is shown in figure 5.2. The main modifications of this extractor are the use of high vacuum teflon stopcocks both at the bottom and on the side tube. Also, a water jacket has been built around the extractor to eliminate the need for a condenser on the top. This significantly reduced the overall length of the extractor allowing it to be easily transferred in and out of the glovebox. In practice, the extractor was dried by baking at 160°C for at least 24 hours prior to use. The extractor was removed from the oven and immediately transferred into the glovebox before it had time to cool down. Inside the glovebox, the extractor was loaded with about 10-20 grams of soot from the arc chamber. The extractor was then sealed by closing both high vacuum valves and placing a glass fitting on top which went to a closed ground-glass stopcock for pressure regulation.

Outside the glovebox, a clean, dry 1 liter Schlenk flask was sealed to the bottom of the extractor and the flask was purged with argon. Approximately 500 ml of dry toluene was transferred via cannula under argon. The toluene had previously been dried by distilling over potassium metal. The higher fullerenes were extracted by refluxing the toluene through the soot. After the toluene coming through was colorless, a new Schlenk flask

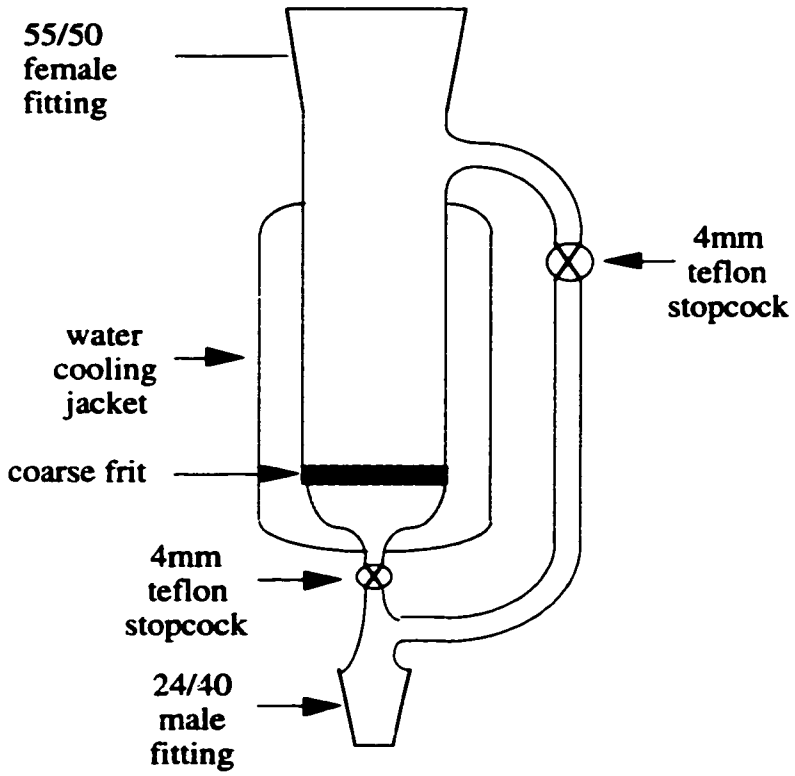

Figure 5.2: Schematic of the extractor used to extract C_{36} under inert conditions. The extractor was built by Tom Lawhead in the College of Chemistry Glass Shop.

containing dry pyridine that had been distilled over sodium was attached to the bottom of the extractor under an argon purge. The C_{36} was then extracted from the soot. Next, the C_{36} solution was transferred via cannula under argon to a dry 500 ml Schlenk tube where almost all of the pyridine was pumped out under vacuum. To eliminate the possibility of vacuum grease contamination, the C_{36} was precipitated out of the pyridine by the addition of 500 ml dry hexanes. This solvent mixture was removed with a filter cannula and the C_{36} precipitate was scraped into a bottle inside the glovebox.

Unlike air exposed C_{36}, Samples of C_{36} prepared by this method could be redissolved in dry pyridine repeatedly indicating that air exposure does play a role in polymer-

ization. Some of the experiments presented in this chapter were performed on C_{36} prepared under the inert conditions described above while earlier experiments were performed on C_{36} exposed to air during synthesis. This difference will be noted for each separate result.

5.2 Mass spectrometry of pyridine extract

The material extracted with pyridine has yet to be characterized. Our only evidence at this point that this material contains C_{36} is the fact that C_{36} is believed to be soluble in pyridine. However, any other pyridine soluble components in the soot may be present in this extract. Also, C_{36} may be present in the form of derivatives such as $C_{36}H_6$ or in the form of dimers and trimers. Mass spectrometry was done on this material using a Laser Desorption/Ionization Time of Flight mass spectrometer in the Zettl laboratory. The samples were prepared under the inert conditions described in section 5.1. The mass spectrum is shown in figure 5.3a. This spectrum shows a broad distribution of carbon species ranging from C_{80} to C_{160}. A similar spectrum had been published previously and attributed to the presence of higher fullerenes [61]. However, it was hypothesized that the mass spectrometry laser was completely polymerizing the C_{36} molecules and then desorbing large, higher mass fragments of this polymerized solid. To prove this, The material was doped with potassium metal in an attempt to reduce the intra-molecular binding energy.

In order to dope the pyridine extract, about 100 mg was added to a dry Schlenk flask inside the argon atmosphere glovebox along with about 20 mg of high purity potassium metal. This flask was sealed, removed from the glovebox and attached to the Schlenkline and evacuated. The atmosphere was replaced with ammonia and the bottom of the

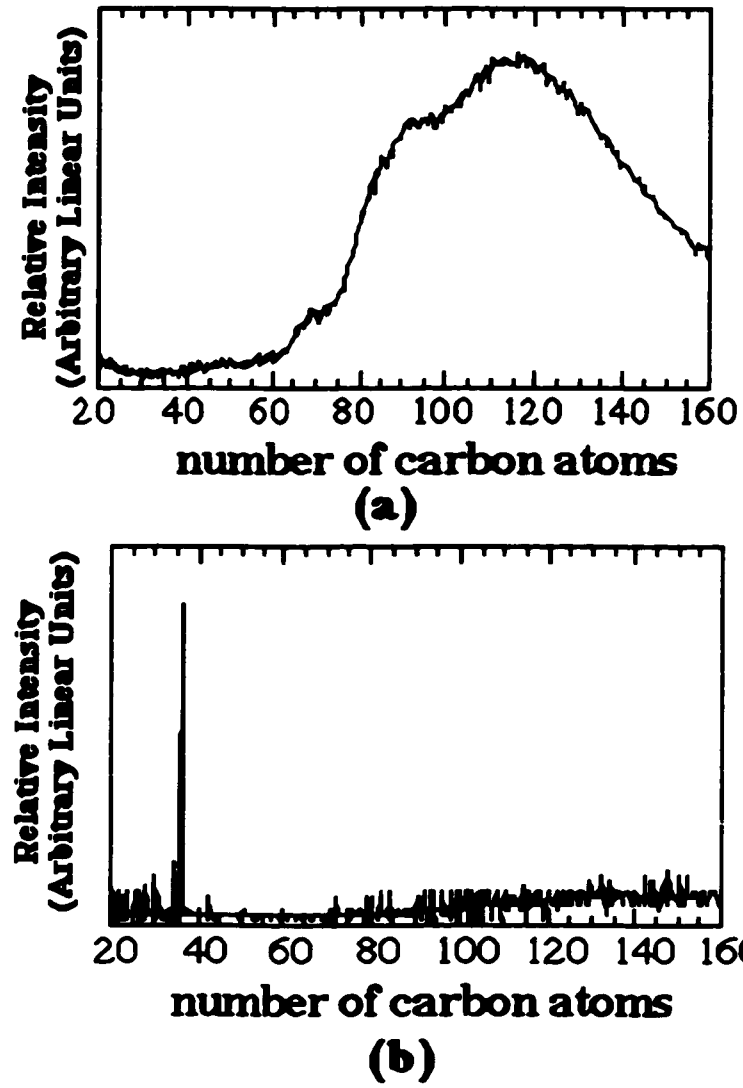

Figure 5.3: a) Time of Flight mass spectrum of the pyridine soluble extract. b) Time of flight mass spectrum of the same material after reduction with potassium metal in liquid ammonia. Spectra aquired with the Zettl group's Jordan Time of Flight Mass Spectrometer.

flask was cooled down in a dry ice/acetone bath. About 200 ml of liquid ammonia was distilled into the flask before returning the system to an argon atmosphere. Both the pyridine extract and potassium metal went into solution in the ammonia. This mixture was stirred for about 4 hours allowing the reaction to proceed towards forming what should presumably be a $K^+ C_{36}^-$ charge transfer compound. This material was dried and scraped

out in the argon glovebox and a small amount of the powder was glued to a mass spectrometry target. The target was quickly transferred in air into the mass spectrometer. The spectrum of this material is shown in figure 5.3b. This spectrum shows a single peak at 36 carbon atoms and no signal in the higher mass end of the spectrum. This demonstrates that the pyridine extract is mostly composed of C_{36} molecules which are polymerized by the laser pulse in the neutral state and photodissociated by the laser pulse in the charged state.

5.3 Electron diffraction

Electron diffraction studies were performed on the solid C_{36} obtained from the pyridine extraction performed in air as well as material scraped from the evaporated film described in section 3.2[46]. In both cases, a small amount of the material was ground up, dispersed on a holey carbon grid, and inserted it into a JEOL 200 CX transmission electron microscope (TEM). The sample was observed to be mostly amorphous with a few isolated crystallites. The grain size of these crystallites was about 100 nm. Using a field limiting aperture, I recorded the diffraction pattern of selected crystallites.

Figure 5.4 shows a TEM diffraction pattern for one of these C_{36} crystallites. The hexagonal diffraction pattern suggests a close packing arrangement perpendicular to the zone axis. This pattern is reminiscent of diffraction patterns observed for C_{60} and C_{70}. However, the d-spacing measured from this diffraction pattern for the first order diffracted spots is 6.68 Å, significantly less than the (100) d-spacing of 8.7 Å reported for C_{60}[3]. This d-spacing is consistent with the predicted d-spacing of 6.55 Å for the lowest energy S2-AB C36 crystal structure (see Chapter 4). Unfortunately, because the C_{36} crystallites

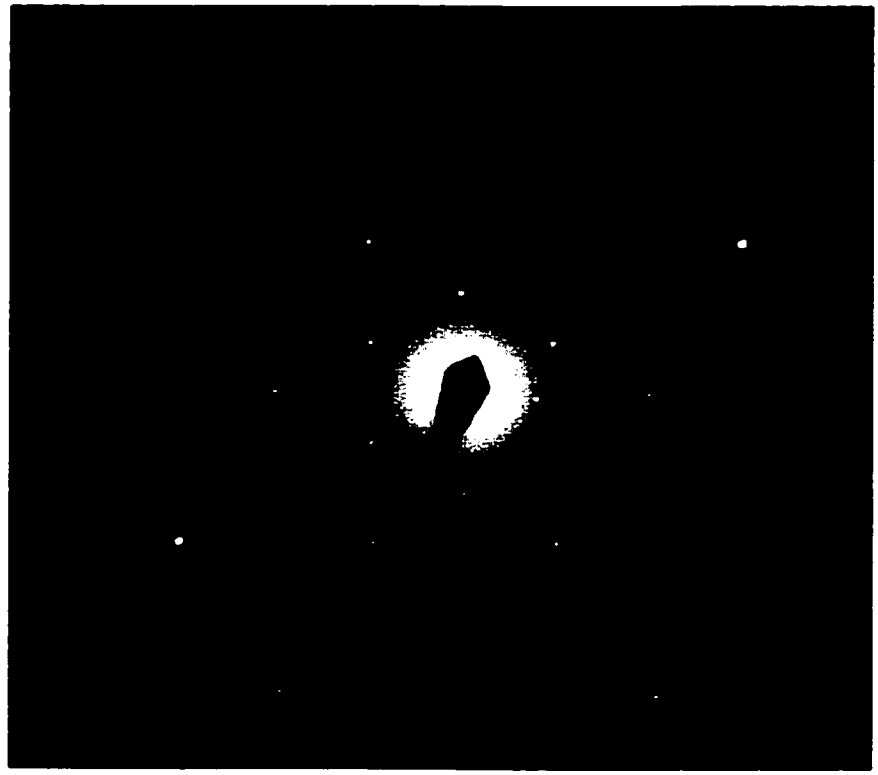

Figure 5.4: Electron diffraction pattern of a C_{36} crystallite. The pattern is hexagonal with a calculated d-spacing of 6.68 Å. (Adapted from Ref. [46])

are platelets with high aspect ratios, this was the only zone axis along which the crystallites were thin enough to allow useful TEM imaging, and thus determination of the detailed C_{36} crystal structure was not possible.

Like C_{60}, C_{36} appears to suffer some TEM-induced damage at an electron beam energy of 200 keV. Under continuous TEM observation, the sharp crystalline diffraction patterns were found to deteriorate for extended irradiation times. Additional studies were performed to investigate the long-term stability of solid C_{36} subject (only) to high ambient temperatures. C_{36} powder was heated in vacuum to 1350 C for 48 hours and then characterized by TEM imaging. Over 50% of the diffraction patterns obtained for the heat-treated material were graphitic, indicating that a large amount of the material had con-

verted to the energetically more favorable graphite.

5.4 Scanning tunneling spectroscopy

The molecular levels of C_{36} thin films have also been studied by Scanning Tunneling Spectroscopy (STS) which was performed by P.G. Collins, M. Ishigami, et. al.[54]. The measured local density of electronic states N(E) has been compared to a predicted density of states for the C_{36} monomer as well as several C_{36} dimer and trimer configurations. C_{36} films were grown using two separate methods, thermal evaporation and solution deposition. For thermal evaporation, the pyridine solubie extract described in section 5.1 was dried and thermally evaporated from a tungsten filament at approximately 10^{-6} torr onto a substrate which was suspended above the filament. This C_{36} powder came from an earlier sample which had been exposed to air during extraction. In order to minimize thermal decomposition of the material, the filament was heated very quickly and the films were grown in a matter of seconds. A shutter was used between the source and the substrate to control the film thickness. Films of thicknesses on the order of 0.1 monolayers to 1 monolayer were grown. Alternatively, films were grown by simply depositing a dilute solution of the pyridine extract onto the substrate and allowing the solvent (carbon disulfide) to evaporate. Two substrates were used in this study, an atomically flat gold (111) film grown on mica and the (001) surface of a highly oriented pyrolytic graphite (HOPG) crystal.

Each of these films were immediately loaded into a room temperature scanning tunneling microscope (STM) using a Pt-Ir tip and Oxford instruments TOPS3 controller. For all samples it was found that the C_{36} film tended to aggregate into islands approximately 10 to 50 nanometers in diameter and 10 to 20 Å high. This clustering is consistent

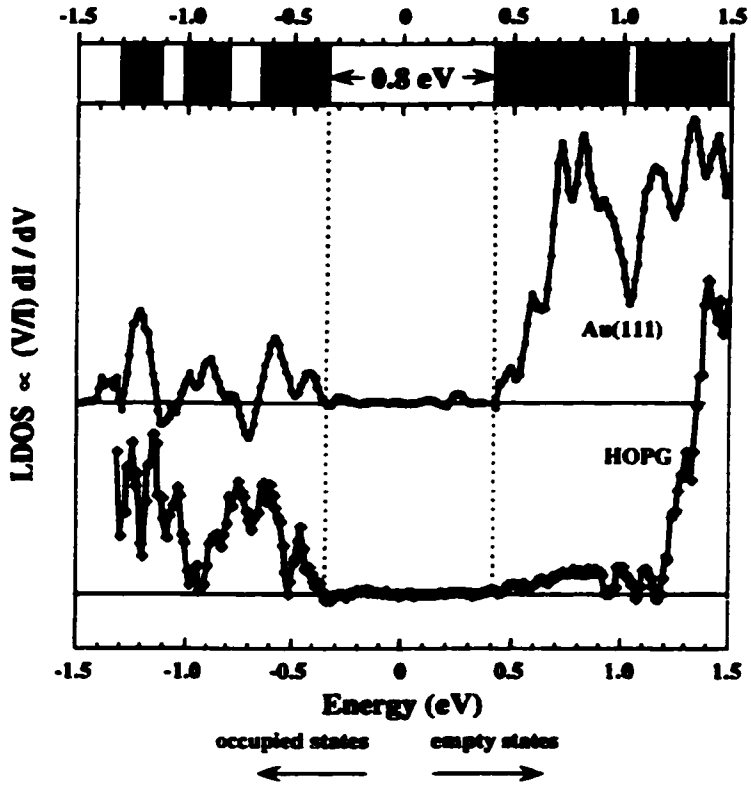

Figure 5.5: N(E) for C_{36} as measured on Au (111) and HOPG substrates. The most reproducible states on both substrates are indicated at the top by black lines with the measured broadening shown in gray. Experiment performed in collaboration with P. G. Collins and M. Ishigami. (Adapted from Ref. [54])

with the predicted tendency of these molecules to covalently bind together. Figure 5.5 shows the STS density of states ((V/I)dI/dV) plot vs. tip bias voltage obtained by placing the tip at a fixed height above a C_{36} island for both substrates. A similar measurement performed above the clean substrates produced the flat line at zero on this plot. Here, several sharp peaks can be seen which indicate resonant tunneling through discrete molecular states. No differences between the thermally evaporated films and the solution grown films could be found. Both spectra indicate the presence of a 0.8 eV gap. There appears to be a slight discrepancy in the features of these graphs which may be explained by the possibility that the surface is influencing the electronic structures of the clusters. Neverthe-

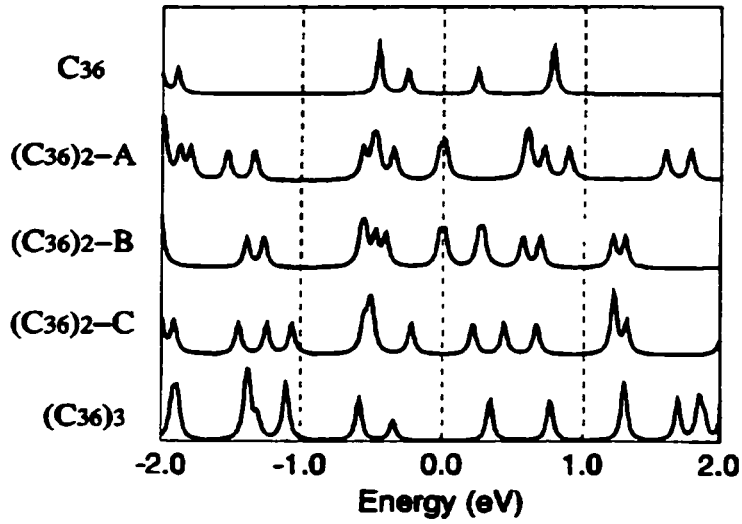

Figure 5.6: Theoretical electronic spectra for five different configurations of C_{36} molecules illustrated in figure 4.3. $(C_{36})_2$-C and $(C_{36})_3$ provide the best match for the experimental spectrum. (Adapted from Ref. [54])

less, the features which are most reproducible on both substrates have been indicated by black strips at the top of the figure with the peak widths shown in gray.

The theoretical LDA calculations for isolated D_{6h} symmetry C_{36} molecules compare favorably with these results and are reproduced at the top of figure 5.6. After accounting for the standard LDA underestimation of the energy gap, the experimental and theoretical spectra match closely near the Fermi level. The theoretical energy spacing between the two lowest unoccupied and two highest occupied molecular levels, as well as the relative spectral weights of these levels, are all reproduced by the experimental data.

However, there is serious disagreement between experiment and theory further from the Fermi level: in LDA, the isolated molecule has no eigenvalues in the +1.0 to +2.0 eV and the -1.0 to -2.0 eV and the -1.0 to -2.0 eV energy ranges, while a number of states appear to be present experimentally. There are a number of effects which may explain

such a discrepancy, including bonding between C_{36} units, impurities in the sample, and passivation of the C_{36} molecules by other species. As has already been discussed, C_{36} molecules are predicted to be more reactive than larger fullerenes like C_{60}, even to the extent that stable covalently-bonded crystals may be formed. Although impurities and passivation cannot be absolutely ruled out, the vacuum environment in which the samples were produced would favor intermolecular bonding as the most likely cause of deviation from isolated-molecule behavior, particularly considering that the molecules are mobile enough to cluster into islands.

To investigate the possible effects of intermolecular bonding, the energy spectra for the dimers and the trimers considered in section 4.2 has been calculated by Grossman, et. al.. The resulting molecular orbital energy spectra shown in figure 5.6 indicate how sensitive the eigenvalue spectrum is to the nature of the intermolecular bonding. To facilitate comparison with the experimental results, a small, unweighted Lorentzian broadening is employed and each spectrum has been shifted so that the middle of the HOMO-LUMO gap lies at 0 eV. Doubly degenerate levels are counted twice so that relative peak heights are meaningful. In dimers A and B, a small gap (0.01 eV) results in a metallic eigenvalue spectrum. Dimer C, on the other hand, has a gap that is roughly the same as in the isolated molecule, shown at the top of the figure. Dimers A, B, and C are all pictured in figure 4.2.

The experimental data in figure 5.5 may now be directly compared to the various theoretical spectra of figure 5.6. Neither dimers A nor B have the appropriate gap, as found for the isolated C_{36} molecule or dimer C. Although the isolated molecule fits the experimental data reasonably, as described above, dimer C possesses a more even distribution of states in the range of 1 to 2 eV above or below the Fermi level. This particular

dimer, therefore, resolves the primary discrepancy between the experimental data and the isolated-molecule energy spectrum. Since it is also considerably well bound energetically, it strongly suggests that the C_{36} molecules are dimerized rather than isolated in this study.

5.5 Infrared spectroscopy

To investigate the infrared spectrum of C_{36}, a small amount of powder from the pyridine extract prepared under inert conditions was ground up. This powder was mixed with dry potassium bromide (KBr) inside the argon atmosphere glovebox. The mixture was then pressed into a thin disk that filled the center of a small brass washer. This washer was then transferred out of the glovebox and mounted in a Mattson Fourier Transform Infrared (FTIR) spectrometer by M. C. Martin at the Advanced Light Source (ALS) in the

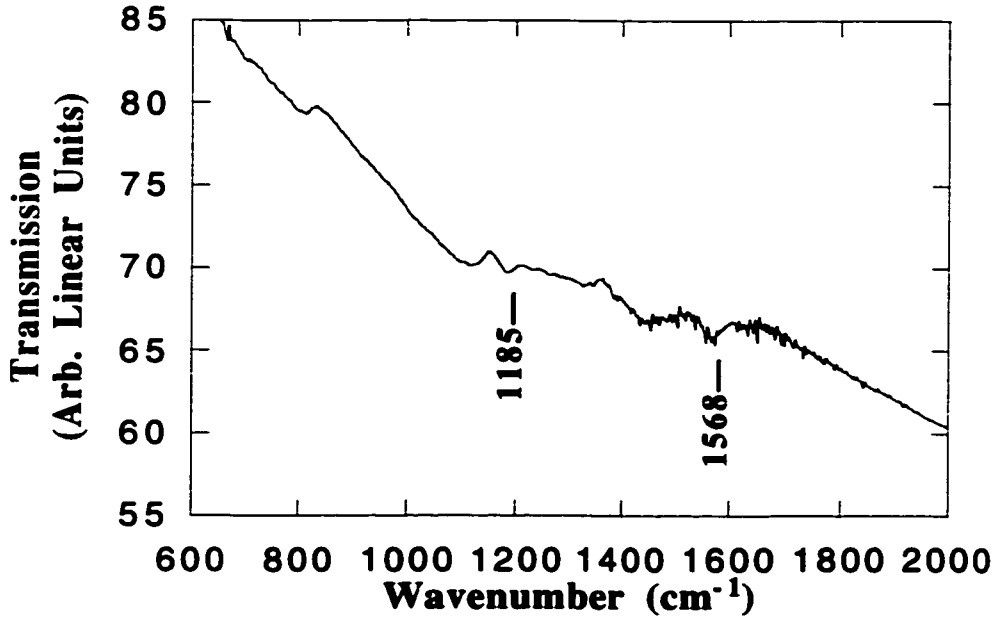

Figure 5.7: Infrared spectrum of the pyridine extract after baking at 225° C overnight in vacuum to remove adsorbed pyridine. The two peaks not accounted for by contaminants are labeled. Spectrum obtained in collaboration with M. C. Martin

Lawrence Berkeley National Laboratory (LBNL). The spectrum showed several strong peaks that were due to residual pyridine remaining in the powder from the extraction process. Therefore, the process was repeated with the additional step of annealing the powder at 225°C overnight in vacuum prior to mixing with the KBr. The resulting IR spectrum from which a pure KBr background has been subtracted is shown in figure 5.7. This spectrum is relatively featureless with a few small absorptions. Some of these peaks are due to a trace amount of vacuum grease that was trapped in the material during extraction. However, there are two peaks that cannot be accounted for by any known impurities. These are at 1185 cm^{-1} and 1568 cm^{-1}. This spectrum does not appear to match the predicted spectrum for isolated C_{36} molecules with either D_{6h} or D_{2d} symmetry (see section 4.7). This further supports the idea that C_{36} molecules are polymerizing in these samples. This polymerization is expected to cause a loss of single molecule vibrational modes leaving only small, broad absorptions in the spectrum.

5.6 Transport measurements

To investigate the possibility that C_{36} may form a superconductor, a small flake of the pyridine extract was wired by gluing on .5 mil gold wires with silver paint in a 4-probe configuration. That is, four wires were glued in a row on a long, thin sample with the outer contacts for sourcing current and the inner for measuring the voltage drop. This technique is advantageous because it eliminates contact resistance. This early transport experiment was performed on material that was synthesized in air. The sample was found to be insulating at room temperature and some slight conductivity was observed at elevated temperatures (>200°C). It was decided to try intercalation with alkali metals to increase the conductivity and possibly form a superconducting compound.

To intercalate the material, a doping cell was used similar to the one drawn in figure 2.4. After heating the sample to 250° C and the rest of the cell to 150° C, the resistance of the sample began dropping. The resistance dropped a total of 3-4 orders of magnitude before leveling off in the kiloohm range. The sample was then cooled down gradually to 4.2 K as resistance data was recorded. For samples intercalated with either sodium or potassium, the resistivity, ρ, as a function of temperature obeyed the functional form,

$$\rho \propto \exp\left[T^{-\frac{1}{3}}\right]$$

a behavior typical of variable range hopping. This may indicate that the sample was not forming a homogeneous compound.

Later, this transport experiment was repeated with a sample that had been doped by the liquid ammonia method described in section 5.2. This time, the starting material had been synthesized and extracted using the air sensitive technique of section 5.1. By intercalating in solution rather than the solid state, the hope was that a more homogeneous phase would be produced. To avoid air exposure, the product was scraped out inside the argon glovebox and loaded into a diamond anvil cell by K. Bradley. This setup uses two diamond surfaces to sandwich the sample under pressure and 4 wires are placed at the interface to measure resistivity in a square configuration. The advantages of the diamond anvil cell in this experiment were twofold. First, it served to keep the sample sealed after transferring out of the glovebox. Second, the high pressure could be used to force the conducting grains in the sample closer to produce a lower resistivity.

Figure 5.8 shows the resistance vs. temperature of a sample of potassium doped C_{36} in the diamond anvil cell at a pressure of 37 kbar. For this data, the log of the resis-

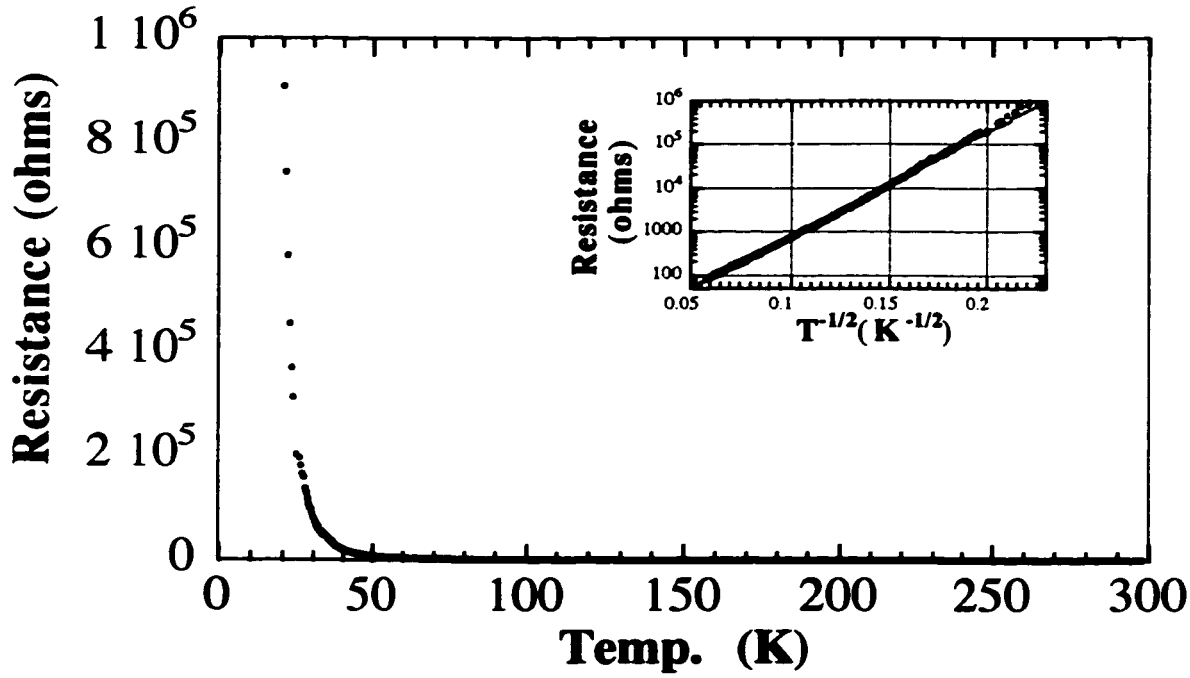

Figure 5.8: Resistance vs. Temperature of a potassium doped C_{36} sample under 37kbar pressure. The inset shows the fit for variable range hopping. Data taken in collaboration with K. Bradley

tance is proportional to $T^{-1/2}$ as shown in the inset. Unfortunately, this suggests that the system is still dominated by variable range hopping. The exact electronic nature of this sample that gives rise to this type of conductivity is difficult to infer due to the poor crystallinity of the sample and the fact that the purity level of the C_{36} in this material is still unknown.

During measurement of current-voltage (I-V) curves with this sample, an interesting effect was observed. Figure 5.9 shows several I-V sweeps taken at 30 K. For each sweep, the sample started out in a low resistance state at low current and then jumped to a higher resistance state at some current, i_c, approximately 100 nanoamperes. Upon ramping down the current, the sample returned to the low resistance state at a current below i_c. For each sweep, the value of i_c changed slightly. This effect was only observed at low

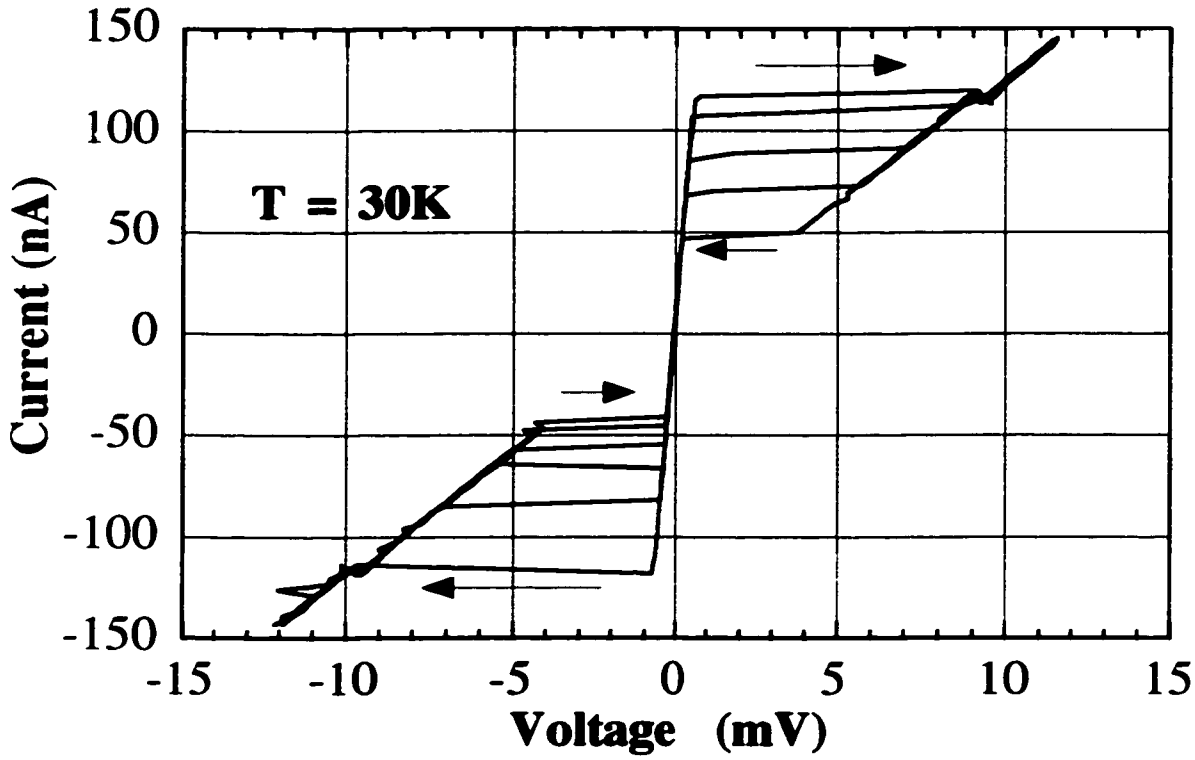

Figure 5.9: Several I-V curves on a sample of potassium doped C_{36} at 37 kbar. These curves appear to mimic Josephson Junction-like behavior. Data taken in collaboration with K. Bradley.

temperatures. As the temperature of the sample increased, the difference in resistance between the two states gradually decreased and at about 60 K, the effect was gone and the I-V curves became linear. Also, this experiment was repeated as a magnetic field of up to 8 Tesla was applied and no change in the I-V curves were observed.

These unusual and unexplained I-V curves are in some ways reminiscent of what is expected for Josephson tunneling across a superconductor-insulator-superconductor (SIS) gap. Therefore, it is instructive to examine these data in terms of results expected if a portion of the sample were superconducting. In this case, there are a number of notable differences between the data and SIS tunneling. One is that the low current state does have a non zero resistance. This could be explained if the sample contains a Josephson junction

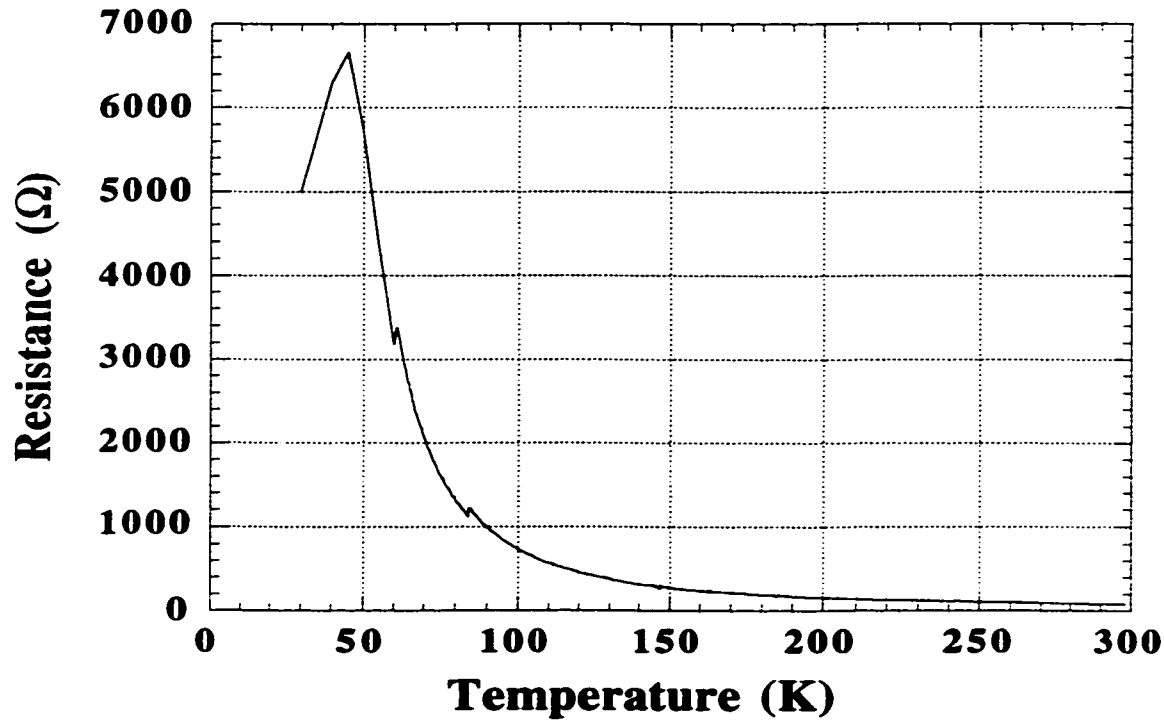

Figure 5.10: Resistance vs. temperature plot for potassium doped C_{36} data measured at low current levels. Data taken in collaboration with K. Bradley

in series with other resistive elements. Another discrepency is that the I-V characteristics should change as a magnetic field is applied. One possible explanation for this is that the size of the Josephson Junction may be exceedingly small so that only a negligible fraction of a flux quantum runs through it at experimentally obtainable fields. A single quantum of flux, Φ_o, is 2.0678 X 10^{-15} Tesla m^2. Thus, at 8 Tesla, the area containing a single quantum of flux is about 250 nm^2. If the cross section of the junction was on the order of only a few nm^2, it is unlikely that the magnetic field would have a noticeable effect on the I-V characteristics.

All of these low temperature data taken in the resistance vs. temperature plot of figure 5.8 were from the high current state of the I-V curves. In figure 5.10, this low tem-

perature data was replaced by the inverse slopes of the low current portion of several I-V curves taken at temperatures between 60K and 30K. In this low current resistance vs. temperature plot, the resistance reaches a maximum at about 45 K and then starts to decrease at lower temperatures.

5.7 Microwave loss measurements

By far the most sensitive technique for detecting superconductivity in highly granular superconductors is by microwave loss spectroscopy[62-64]. This technique is performed inside the microwave cavity of an electron paramagnetic resonance (EPR) spectrometer. The method involves placing the superconductor inside the cavity and tuning the microwave frequency to resonance after the sample has been cooled down below T_c. An external magnetic field is then slowly ramped up to some value on the order of H_{c1}. This field causes magnetic flux to penetrate into the Josephson Junctions formed between the superconducting grains thereby reducing the overall diamagnetism of the sample. This reduced diamagnetism means that the microwaves are no longer excluded from the bulk of the sample. The effective size of the microwave cavity is thus increased which leads to a loss of resonance and a decrease in the overall microwave power inside the cavity. Also contributing to a decrease in microwave power is the flux vortices moving in the Josephson Junction. Mobile vortices give the sample a non zero resistance which causes absorption of microwave power.

The dramatic change in the microwave power of a resonant cavity with the application of a relatively small magnetic field suggests the possibility of superconductivity. However, this behavior is not exclusive to superconductors. For example, Giant Magnetoresistance (GMR) materials may also display this effect. In order to conclude that the

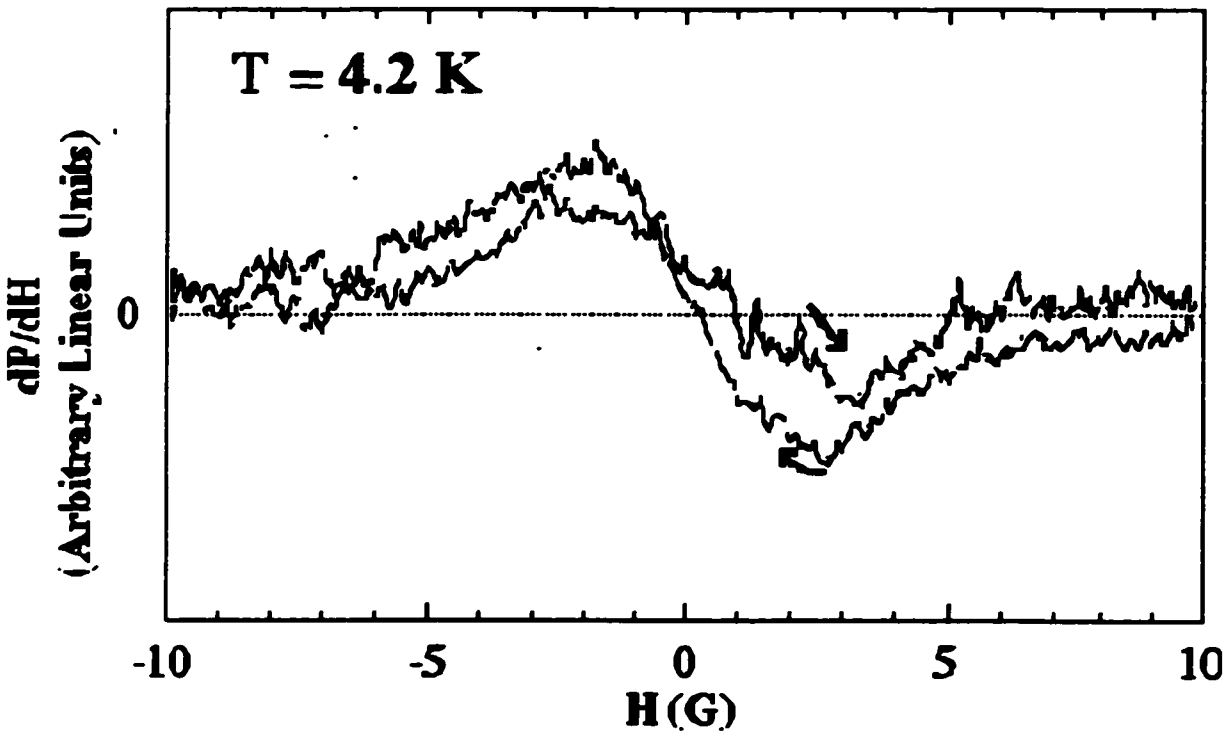

Figure 5.11: Plot showing the change in microwave power with magnetic field vs. the total applied field. The arrows indicate the sweep direction. Data were taken in collaboration with Dr. J. Krüger and Professor E. R. Weber.

sample is truly superconducting, the field must be ramped in the opposite direction, from H_{c1} to $-H_{c1}$ and finally back to zero. If the sample is superconducting, flux vortices will be pinned in the Josephson junction and when the field is reversed, these vortices will be cancelled out by vortices pointing in the opposite direction. This cancellation leads to a lower loss of microwave power when the negative field is applied.

To test intercalated samples of C_{36} by microwave loss, approximately 30 mg of pyridine extract prepared under inert conditions was combined with 5 mg of potassium metal in a dry, 6mm quartz tube. This tube was sealed off under vacuum and baked at 200°C overnight. The next day, the sample was placed in Professor E. Weber's EPR spectrometer. After cooling the microwave cavity to 4.2 K, the field was slowly swept back and forth between 10G and -10G. Figure 5.11 shows a plot of the derivative of microwave

power with respect to field (dP/dH) vs. magnetic field. The sweep in the positive direction shows a larger change in microwave power at negative magnetic fields than at positive magnetic fields. The opposite is true for the sweep in the negative direction. As a reference, this measurement was performed on a sample of powdered K_3C_{60}. A very similar plot resulted except that the signal was 2 orders of magnitude stronger. Therefore, if this signal is due to superconductivity, then only about 1% of the intercalated C_{36} sample is superconducting. To study the temperature dependence of this effect, the sample was gradually warmed and this measurement was repeated at several temperatures. The microwave loss signal was observed to gradually decrease upon warming until it was no longer detectable at about 40 K.

Although the data presented in this section is suggestive that a portion of the sample is superconducting, it would be premature to draw this conclusion based on microwave loss data alone. As discussed at the beginning of this section, there may be several other explanations of the observed signal, some of which have yet to be ruled out. A more reliable technique for showing the presence of superconductivity is by measuring the Meissner effect through D.C. magnetic susceptibility measurements. As will be shown in the next section, we have not yet been able to resolve a diamagnetic transition in any of the samples measured.

5.8 Magnetization measurements and organic ferromagnets

The magnetization properties of potassium doped C_{36} phases were measured in a magnetometer that employed a Superconducting Quantum Interference Device (SQUID). This method requires that the sample be mounted in a tube with uniform magnetization along its length. This task was especially challenging because the sample had to be kept

sealed to avoid air exposure. This was accomplished by pressing half of a gelatin capsule into the middle of a Pyrex tube and filling the capsule with the about 50 mg of potassium doped C_{36} inside the glovebox. Afterwards, the pyrex tube was flame sealed under vacuum and the assembly was centered in the SQUID Magnetometer. The sample had been prepared by extracting with pyridine under inert conditions with subsequent potassium intercalation in liquid ammonia.

To look for superconductivity, the sample is first cooled with zero magnetic field and magnetization data is taken while warming in a small field. Below T_c, the Meissner effect causes the superconductor to expel the external field and a strong negative magnetization is recorded. Next, the sample is cooled with the small magnetic field turned on. In this case, magnetic flux is "trapped" between the superconducting grains. Data is then taken while warming and the magnetization remains constant below T_c. To demonstrate this, a powder sample of K_3C_{60} was prepared and mounted in one of the evacuated pyrex tubes for magnetization measurements. This data is shown in figure 5.12 for both the field cooled and zero field cooled measurements. Notice that the two sets of data are nearly identical above 19K. Below 19K, the field cooled data remains relatively constant while the zero field cooled data shows a strong diamagnetic transition.

This same measurement was made on the potassium intercalated C_{36} sample. The plot is shown in figure 5.13. Surprisingly, both curves have a very strong positive magnetic susceptibility. Also surprising is the fact that the two curves differ significantly over the entire temperature range. This behavior is consistent with ferromagnetism rather than superconductivity. To verify that the sample was truly ferromagnetic, magnetization vs. magnetic field data was recorded at a fixed temperature. Data points were taken at 100

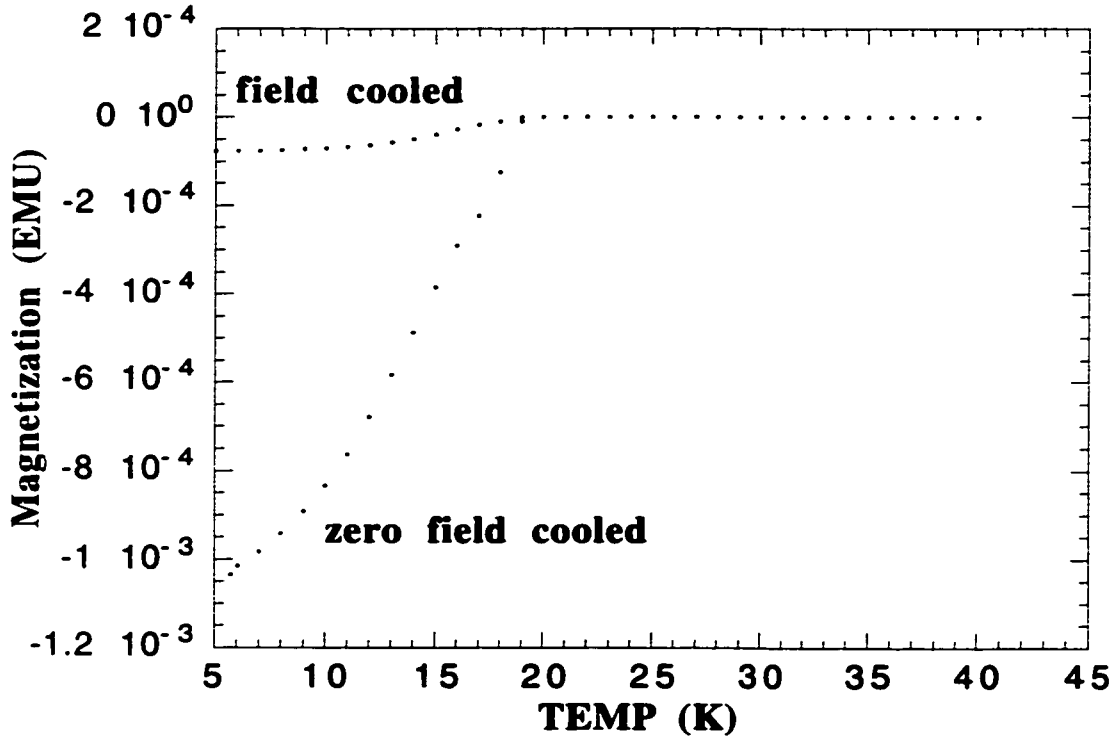

Figure 5.12: Magnetization data for 50 mg of K_3C_{60} (T_c = 19.3K). The field used for measuring magnetization was 10 Gauss. The data was taken while warming after cooling in both zero field and in a field of 10 Gauss.

Gauss increments as the field was ramped up to 1500 Gauss, back down to -1500 Gauss and finally back to zero. A ferromagnet should exhibit hysteresis due to the fact that the magnetic domains tend to align with the field and these domains remain aligned until a sufficiently strong negative field is applied. This hysteresis is exactly what is observed in the data shown in figure 5.14. It was also noticed that this material could be deflected by holding a powerful magnet to the side of the glass tube. This behavior stopped completely once the material was exposed to air.

The origin of this ferromagnetic property could be from two different sources. Either a doped phase of C_{36} is ferromagnetic or there is a ferromagnetic impurity present in the sample. To investigate the latter, the sample was submitted for Energy Dispersive

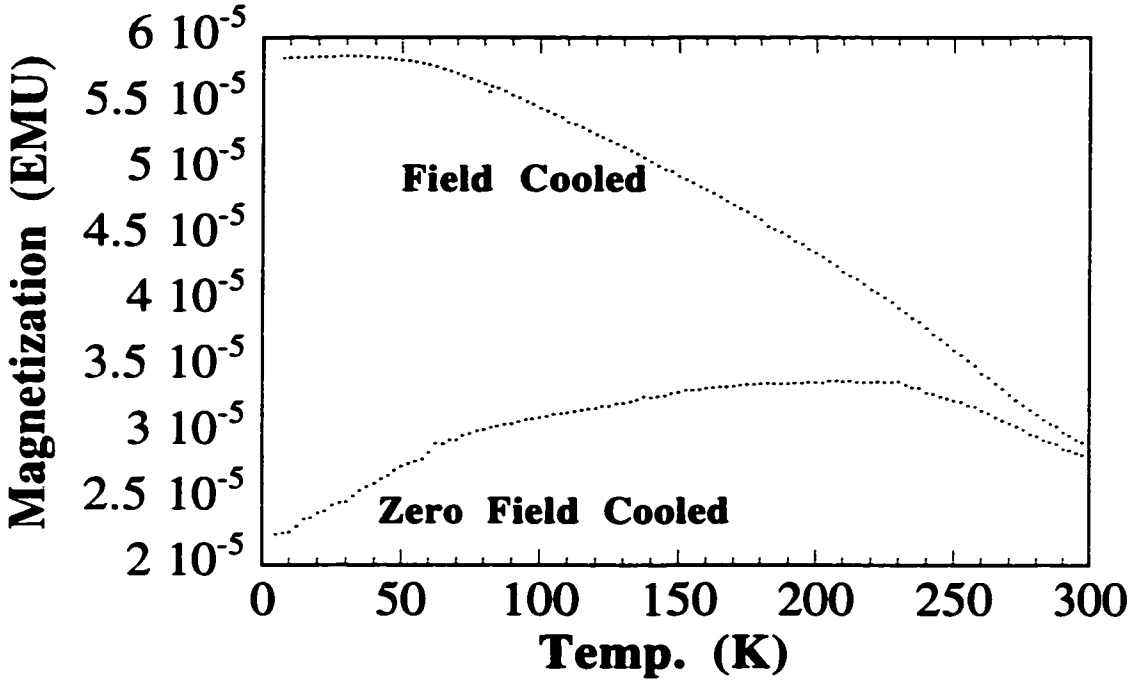

Figure 5.13: Magnetization data for potassium intercalated C_{36} using a magnetic field of 30 Gauss. The large positive magnetization and the difference between the field cooled and zero field cooled curves is indicative of ferromagnetism. Data were taken in collaboration with M. Ishigami.

X-Ray spectroscopy (EDAX). This technique uses an electron beam to excite the electrons in the core states of metals. The energies of the X-Rays emitted when these electrons drop back down into the core levels is measured to determine the type of elements present. EDAX did not detect the presence of any elemental ferromagnetic impurities in the C_{36} sample. Also, the fact that the ferromagnetism was lost upon exposure to air suggests that this is not due to the presence of transition metal impurities.

From IR measurements, the only known impurity present in these samples is pyridine (see section 5.5). To investigate the possibility that a reaction product of pyridine and potassium might be ferromagnetic, approximately 50 mg of clean potassium metal was added to a dry Schlenk flask with a magnetic stirrer inside the argon glovebox. The flask

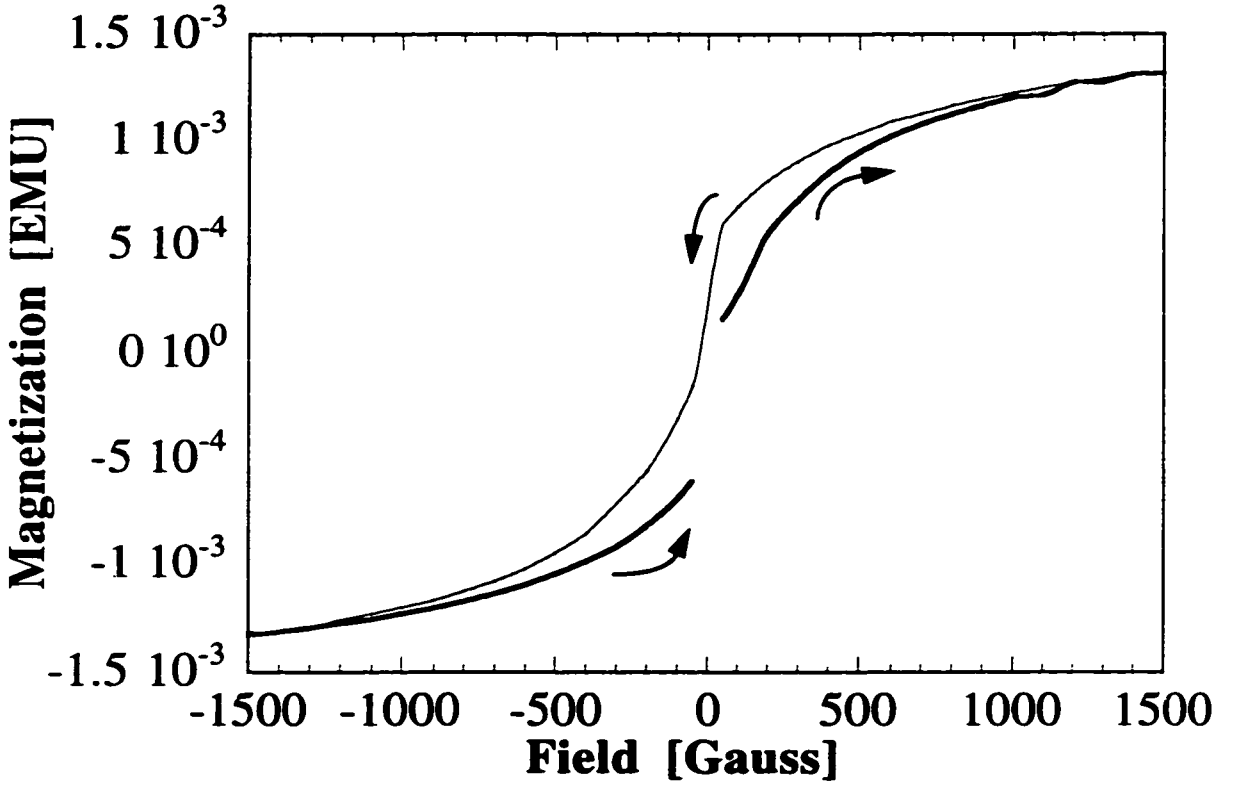

Figure 5.14: Magnetization of C_{36} vs. magnetic field at 100K. This hysteresis was present in the data up to room temperature. Data were taken in collaboration with M. Ishigami.

was then sealed, transferred out of the glovebox and attached to the Schlenk line. Next, approximately 200 ml of pyridine was transferred to the flask by cannula under argon. This pyridine had previously been dried by distillation over sodium metal in an argon atmosphere. The Schlenk flask was then heated until the pyridine started to boil slightly. This temperature was maintained with stirring for approximately 4 hours. During this process, a dark purple solution formed with a black precipitate. This is presumably due to the dimerization and polymerization of the pyridine molecules after reduction by the potassium. Afterwards, the flask was cooled to room temperature and evacuated to remove the unreacted pyridine. Once dry, the flask was transferred back into the glovebox and the remaining black powder was scraped out and placed in a pyrex tube containing half of a

gelatin capsule for SQUID measurements. SQUID measurements on this material showed a similar hysteresis loop as in figure 5.14. This time, the hysteresis was even more pronounced with a coercive field of approximately 200 Gauss. Also, several flakes in the sample could easily be dragged along the length of the tube by moving a strong magnet along the outside. This technique provided a way of separating out the portion of the sample that was most ferromagnetic. Upon exposure to air, the sample immediately turned yellow and was no longer ferromagnetic.

To the best of our knowledge, this pyridine complex is one of the first reproducible organic molecular ferromagnets with a T_c well above room temperature[65]. Organic ferromagnets are becoming a research topic of great interest to material scientists, physicists and chemists. The prospect of designing and chemically synthesizing ferromagnetic molecules will allow researchers to designate specific properties such as magnetic moment and magnetic interaction between neighboring molecules. This new organic ferromagnet has potential applications in a number of fields including low-frequency magnetic shielding, magnetic imaging, magneto-optics and information storage. Another great advantage is that organic ferromagnets are extremely lightweight relative to transition metal ferromagnets such as iron or nickel. Before any of these applications are realized, this material will need further characterization.

5.9 C_{36} derivatives

To explore the chemistry of C_{36}, a number of experiments were performed to try to functionalize this molecule. For this project, we collaborated with J. Kriesel and Professor T. D. Tilley in the College of Chemistry. In theory, a functional group ought to passivate the reactive sites on the C_{36} molecule making it less susceptible to polymerization and

easier to characterize. Most of these experiments were modeled after well known C_{60} derivatization reactions[66]. These reactions all produced a mixture of species with molecular weights in the 500-700 amu region. Unfortunately, because C_{36} has so many reactive sites, all of these reactions produced a complicated mixture of derivatives making separation and characterization difficult.

For example, a reaction was attempted where C_{36} is reduced with n-butyl lithium and quenched with methyl iodide. When Wudl, et. al. carried out this reaction on C_{60}, a mixture of species were produced[66]. This included fullerenes with up to 4 methyl groups and 1 butyl group attached. To reproduce this experiment using C_{36}, approximately 10 mg of the pyridine extract prepared in air was transferred to a small flask containing 200 ml of dry tetrahydrofuran (THF). It was noticed that the pyridine extract was not soluble in the THF. Next, 1.5 ml of n-butyl lithium (10 M in Hexanes) was added via syringe and the mixture was stirred under nitrogen. Immediately, the pyridine extract formed a dark brown solution. This was stirred for approximately 1 hour. The reaction was then quenched with 5 ml of methyl iodide. Afterwards, further purification of this material was attempted by running the material through a chromatography column packed with neutral alumina using a 9:1 mixture of THF and methyl alcohol. The major fraction obtained from this separation was submitted to the college of chemistry's mass spectrometry lab where it was run on the electron ionization (EI) mass spectrometer. The spectrum is shown in figure 5.15.

From this spectrum, there appears to be two major components present in the sample, one with a molecular weight of 621 amu and the other with a molecular weight of 636 amu. Originally, these peaks were attributed to some combination of butyl groups and

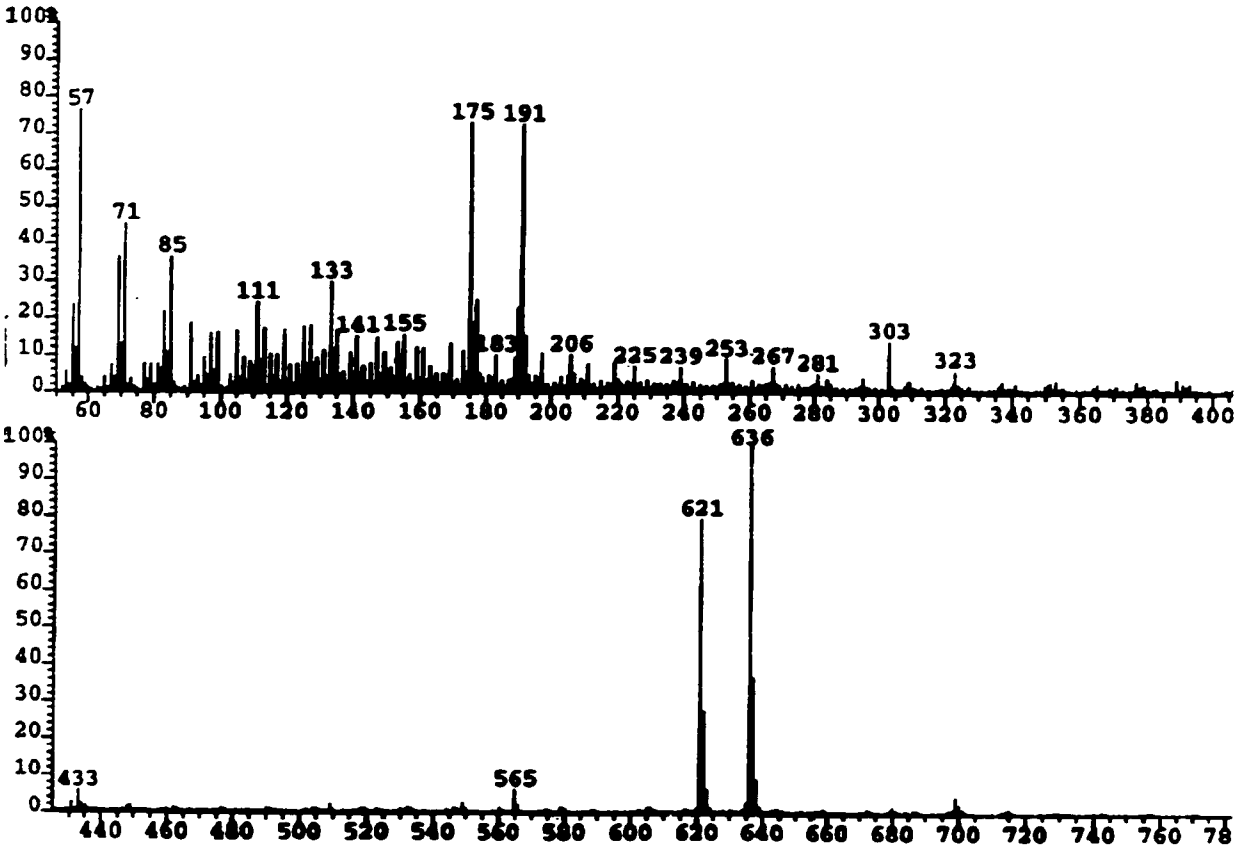

Figure 5.15: Electron impact mass spectrum of the product from a reaction with C_{36}, n-butyl lithium and methyl iodide. The major peaks at 621 and 636 amu have yet to be characterized. Spectrum obtained in the College of Chemistry's Mass Spectrometry Department.

methyl groups attached to a C_{36} parent molecule. This would have been consistent with the mass difference between these peaks being the same as the mass of a methyl group (15 amu). However, these peaks were present in similar reactions were no methyl groups were used. For example, when the pyridine extract was reacted with n-butyl lithium and quenched with water rather than methyl iodide, these two peaks were present in the spectrum. To date, the exact structure of these molecules has yet to be determined.

Chapter 6..

Other experiments

6.1 Coated ferromagnetic nanoclusters

A new technique for producing nanoscale ferromagnetic clusters by high temperature vapor phase precipitation has been developed. Highly spherical magnetic clusters of composition $Ni_{.7}Fe_{.3}$ were produced with a size distribution ranging from 20 nm to 100 nm in diameter. The synthesis method allowed the clusters to be coated with a thin film of foreign material, including either electrical insulators or conductors. To the best of our knowledge, only conducting carbon coated clusters had been reported[67-69]. During the synthesis process the clusters aggregated into long (micron length) thin flexible chains resembling beads on a string. Presumably, this aggregation is due to the magnetic dipole interaction between clusters. The cluster size within a given chain tends to be more uniform than the average distribution.

The synthesis was accomplished by arcing a composite anode against a water-cooled copper cathode inside a stainless steel, water-cooled chamber kept under a static helium pressure of 650 torr. The anode consisted of a hollow tungsten alloy tube (inner diameter 9mm, outer diameter 12 mm) constructed from a machinable tungsten alloy (denalloy, DX-1D) of atomic percentages 90% W, 7% Ni and 3% Fe. The interior of the tube was either left empty or was completely filled with either a hot-pressed graphite rod (POCO graphite) or a hot-pressed boron nitride rod (Advanced Ceramics). To initiate arc-

ing, the electrodes were connected to a regulated D.C. current power supply set at 75 amperes. Prior to the experiment, the chamber was pumped and purged with helium gas three times before the helium pressure was set to 650 torr. To start the arc, the electrodes were momentarily contacted and then separated by a small gap on the order of 1mm. Near the tip, the tungsten tube gradually melted while the boron nitride or the graphite inner rod sublimated. Almost immediately upon the initiation of an arc, wispy threads moved about in the chamber in response to convection currents in the helium gas. After arcing, the chamber was opened and the wispy material was collected for analysis. As will be discussed below, it consists almost entirely of spherical magnetic clusters almost completely devoid of tungsten.

Analysis of the synthesized material was accomplished using transmission electron microscopy (TEM) both to image the material as well as for electron diffraction studies. Also, Energy-Dispersive X-ray analysis (EDX) was used to determine the ratio of nickel to iron in the clusters as well as to measure the percentage of tungsten present.

For TEM studies, the threadlike material was dispersed on a holey carbon grid by dragging the grid over the sample and then shaking the grid to remove very large pieces. Figure 6.1 shows a TEM micrograph of a typical thread specimen prepared using boron nitride as the filler material in the composite anode. The micrograph shows several chains of almost perfectly spherical particles: each cluster in these chains has a diameter of about 20-50 nanometers. These clusters consist of a dense crystalline core and an amorphous boron nitride outer coating. The amorphous coating is approximately 2 to 5 nanometers thick or about 0.1D, where D is the diameter of the cluster. Synthesis runs with graphite as the filler material in the composite anode yielded similar results, i.e. chains of clusters

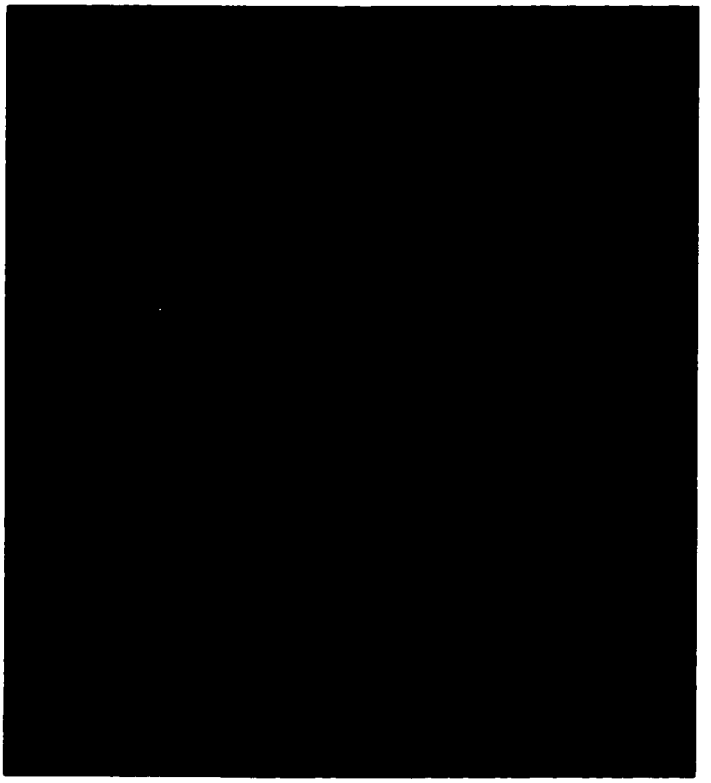

Figure 6.1: Transmission electron micrograph of several ferromagnetic nanoclusters. The clusters aggregate into long chains due to magnetic interactions.

with amorphous coatings. Synthesis runs where the anode was hollow produced "bare" clusters with no coating.

While in the TEM, several selected area diffraction patterns were also recorded. Figure 6.2 shows one of these patterns which has been indexed and matches that of a face-centered cubic structure with a lattice constant of 3.6 Å. This structure and lattice parameter are typical for nickel-iron alloys. The fact that this is a polycrystalline diffraction pattern containing rings rather than discrete spots is due to the large number of clusters contained in the selected area. This diffraction pattern along with the lattice fringes visible in most of the clusters of figure 6.1 leads us to conclude that these nickel-iron clusters are highly crystalline.

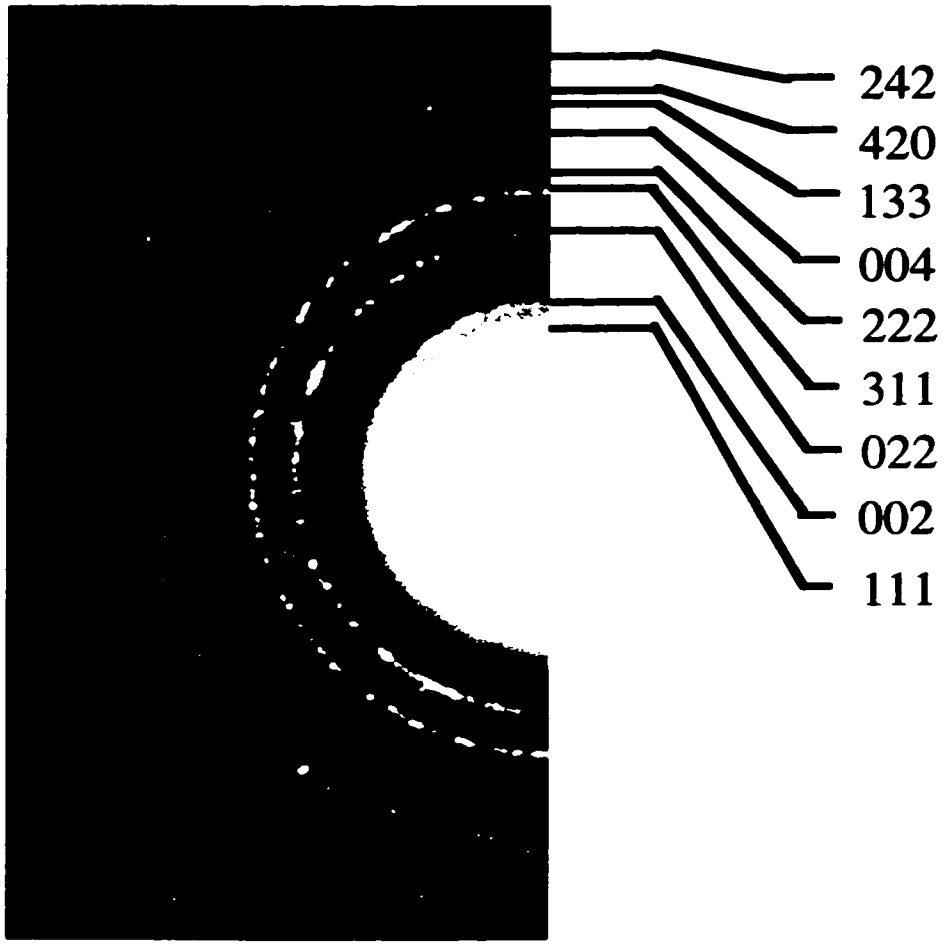

Figure 6.2 Selected area electron diffraction pattern from several nickel/iron clusters. The ring pattern has been indexed and fits to a face centered cubic crystal lattice with a lattice constant of 3.6 Å. Diffraction pattern measured by D. Bernaerts at the National Center for Electron Microscopy (NCEM).

For further characterization, these samples were quantitatively analyzed for iron and nickel by energy dispersive X-ray spectroscopy in a scanning electron microscope using a 20 kV beam. The results indicated that a micron sized portion of sample consisted of 32.39 atomic percent iron and 67.29 atomic percent nickel, very close to the original ratio specified to be in the Denalloy rod. Interestingly, the sample contained only .32 atomic percent tungsten. Because this technique is only sensitive to high Z elements, the percentage of boron nitride or carbon coating the sample could not be determined.

To test that the boron nitride coating provided sufficient electrical insulation, two silver paint contacts were made at either end of a single fiber (approximately .5 mm apart) of material collected after a run in which the tungsten alloy tube contained a boron nitride rod. These contacts were wired to a voltage source in series with a current meter capable of measuring in the microampere range. No current was measured at a potential difference of 50 volts. Therefore, the resistance of a typical single fiber is greater than 50 MΩ.

These clusters could have a broad range of applications. The prospect of growing single domain magnetic clusters with the minimum number of atoms is of increasing technological importance as magnetic data storage densities become extreme. Of equal importance is the development of a controlled way to isolate these clusters to reduce magnetic interactions that could lead to a loss of ordering. One possible solution is to develop a reliable process for coating individual clusters with a durable, nonmagnetic material of a controlled, uniform thickness. Such a coating may be of further importance in protecting the cluster from either chemical attack or mechanical indentation. Other applications may require a cluster coated with a lubricating film or an electrically or thermally insulating or conducting layer. One such application may be for chemical or biochemical experiments that require magnetic manipulation mediated by magnetic clusters[70].

In addition to these practical applications, magnetic clusters have a variety of interesting physical properties. Clusters of a few atoms to several thousand atoms in size form a convenient bridge between the characteristics of a single atom and those of the infinite solid. Because a large percentage of atoms in a cluster are surface atoms, a cluster of even modest size may display properties very different from those of the bulk material. For example, clusters often have dramatically depressed melting temperatures, unusual crystal

structures and magnetic ordering[71,72].

6.2 Enhanced growth of multi-walled carbon nanotubes

A method has been developed to greatly increase the rate of production of multi-walled carbon nanotubes using a low-pressure mixture of helium and nitrogen in the arc discharge technique described in section 2.8. Several graphite-arc experiments were performed to determine the effects of a partial pressure of nitrogen gas on the growth rate of multi-walled carbon nanotubes. These experiments were all performed in a standard water-cooled "bucky chamber" similar to the one shown in figure 2.2. After flushing and filling the chamber with buffer gas, a D. C. arc was struck between the electrodes and the anode was fed into the arc so as to maintain a 1 mm gap. The power supply was a constant current, D. C. arc welder set at 120 amperes. The buffer gas used was a mixture of helium and nitrogen in a 1:1 ratio. Several experiments were done over a range of pressures below 200 torr. For each of these experiments, the arc was maintained for exactly five minutes so that quantitative comparisons could be made. As a reference, a series of 5 minute arcs was also done using pure helium gas over a range of pressures between 50 and 750 torr. For each experiment, the mass of the boule, the anode before and after and the soft, fibrous, nanotube-rich material inside the boule was recorded to determine both the yield and the rate of nanotube production. Also, the soft fibrous material produced in the nitrogen arc was analyzed by TEM to determine the approximate percentage of nanotubes as well as by Electron Energy Loss Spectroscopy (EELS) to determine whether or not nitrogen had been incorporated into the walls of the tubes.

Table 6.1 shows the results of the series of arc runs using pure helium as the buffer gas. For each arc run, the boule was broken off from the cathode and weighed. Next, the

Figure 6.1:

total pressure (torr)	graphite mass sublimated from anode (mgs)	boule mass (mgs)	tube mass (mgs)	% tubes in boule	% yield	growth rate (mg/min)
50	1083	620	54	8.7	5.0	10.8
410	1055	590	96	16.3	9.1	19.2
490	898	473	89	9.8	9.9	17.8
550	1106	656	111	16.9	10.0	22.2
620	1048	582	112	19.2	10.7	22.4
650	942	523	104	19.9	11.0	20.4
670	905	515	83	16.1	9.2	16.6

Table 6.1: Data on yield and growth rate for a series of 5 minute arc runs in pure helium buffer gas. Percent yield is based on the total graphite sublimated from the anode and tube mass refers to the fibrous material scraped from the inside of the boules.

soft, fibrous inner material was scraped out and weighed. This is reported in the table in terms of both the mass and percentage of the total boule mass. The table refers to these quantities as the "tube mass" and the "percentage of tubes in boule" because this soft fibrous material consists almost entirely of multi-walled nanotubes. Also shown is the percent yield of nanotube containing material based on the total mass of carbon which sublimated from the anode. The rate at which this nanotube containing material inside the boule was produced is also indicated in the column labeled growth rate. The data in this table confirms previous reports that pressures slightly above 500 torr are optimal for obtaining the maximum yield of nanotubes with almost the maximum growth rate[73]. Here, it was observed that at 650 torr He, 11% of the graphite that sublimated from the anode was converted to nanotubes-rich material. Also, this nanotube-rich material was produced at a rate of 20.8 mg per minute. Interestingly, the mass of the boule itself

total pressure (torr)	graphite mass sublimated from anode (mgs)	boule mass (mgs)	tube mass (mgs)	% tubes in boule	% yield	growth rate (mg/min)
50	2179	1106	41	3.7	1.9	8.2
100	1409	976	209	21.4	14.8	41.8
150	1382	819	188	23.0	13.6	37.6
200	1611	1313	136	10.4	8.4	27.2
250	1545	1243	87	7.0	5.6	17.4
300	2041	1634	64	3.9	3.1	12.8

Table 6.2: Data on yield and growth rate for a series of 5 minute arc runs in a 1:1 helium/ nitrogen buffer gas. Percent yield is based on the total graphite sublimated from the anode and tube mass refers to the fibrous material scraped from the inside of the boules.

remained relatively constant for each run in this survey. However, some of the boules, particularly those grown at low helium pressures, had a very thick outer shell of hard, gray carbon with very little fibrous material on the inside. On the other hand, this outer shell was very thin for boules that produced a high yield of nanotubes.

Table 6.2 shows the same quantities for a series of arc runs using a mixture of helium and nitrogen at a 1:1 pressure ratio. Here, the optimum yield and growth rate was found to occur at 100 torr total pressure. At this pressure, the yield of nanotube rich, inner-boule material was found to be 14.8%, a significant increase over the optimum yield using pure helium as the buffer gas. However, most striking is the growth rate of 41.8 mg per minute, at a rate that is almost a 100% increase over the pure helium result. Under these conditions, the boule grew at a rate equivalent to the rate of anode sublimation so that very little adjustment of the anode position was necessary to maintain the necessary 1 mm gap.

Figure 6.3 shows a plot of nanotube growth rates vs. pressure for both the pure helium runs and the experiments with a mixture of helium and nitrogen. This plot is shown to better illustrate the dramatic increase in growth rate with the introduction of a partial pressure of nitrogen. Also evident from this plot is how sensitive the growth rate is to the total pressure for the nitrogen/helium mix as compared to the pure helium data.

The boules grown in the presence of nitrogen had black, powdery, carbonaceous deposits growing from the base as well as around the cathode. Samples of these deposits were collected for elemental analysis and TEM. Elemental combustion analysis found this material to consist of 89.32% carbon, 0.28% hydrogen and 4.01% nitrogen. Unfortunately, it is still yet to be determined whether the nitrogen found to be present is only physisorbed onto the surface of the carbon or has actually been chemically incorporated into the structure of the carbon network. For TEM analysis, a small amount of this powder was dispersed on a holey carbon grid and loaded into a JEOL 200 CX TEM. This material was not found to contain any nanotubes and consisted entirely of amorphous material.

In order to verify that the soft, inner-boule material contained a large percentage of carbon nanotubes for the optimum nitrogen/helium run at 100 torr total pressure, this material was examined by TEM. For mounting on a grid, these fibrous particles were ultrasonically dispersed in methanol and then a drop of this was placed on a holey carbon grid. Figure 6.4 shows a TEM image that is a good representation of the entire sample. Here, there is clearly a very high percentage of multi-walled carbon nanotubes with the a typical distribution lengths and number of walls. Also present is a small amount of amorphous carbon and graphitic "onion" structures. Overall, the density of nanotubes here is similar to other published TEM micrographs for helium synthesis prior to purification[74].

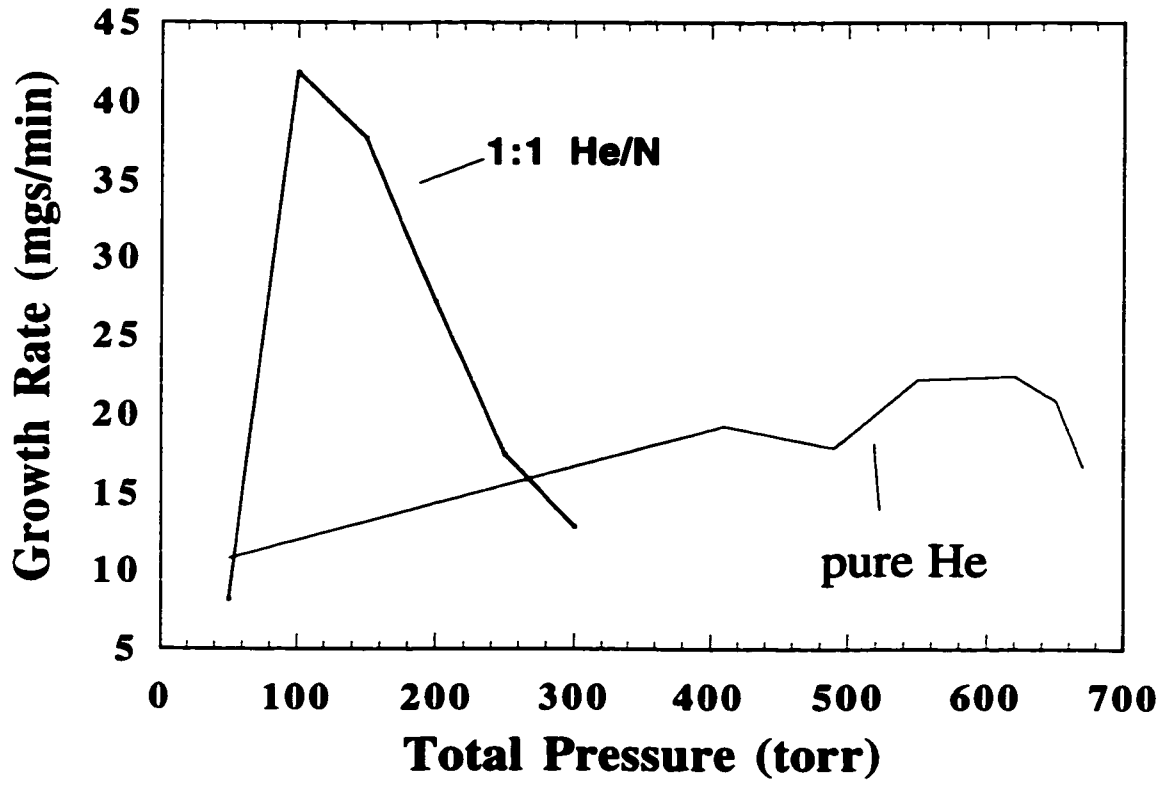

Figure 6.3: Plot comparing growth rate of nanotube-rich material to total pressure for both pure helium and a 1:1 nitrogen/helium buffer gas. This plot illustrates the dramatic enhancement of the growth rate by the introduction of nitrogen.

While in the TEM, EELS was also performed on the tubes to determine if nitrogen had been incorporated into the graphitic lattice. The results from EELS indicated that no nitrogen was present in the tubes. Therefore, for all practical purposes, these tubes are indistinguishable from those produced in the pure helium arc.

The exact mechanism for this enhancement of carbon nanotube yield and growth rate in the presence of a partial pressure of nitrogen is open to speculation. One possible explanation is that the ionization potential of nitrogen is higher than helium. This higher ionization potential gives rise to a potential difference of about 30 volts between the electrodes during the arc, as opposed to about 20 volts for the pure helium arc. At a current of

Figure 6.4: TEM micrograph of typical multi-wall carbon nanotubes grown in the low pressure nitrogen/helium arc. EELS indicates that these tubes do not contain nitrogen.

120 amperes, this corresponds to an additional 1200 Watts available to heat the plasma. This additional heating should increase the temperature and density of carbon vapor in the plasma. This higher plasma temperature ought to produce more carbon monomers, dimers and trimers which are believed to be most ideal for the formation of carbon nanotubes[75-77].

6.3 Nanotube doping

The sensitivity of carbon nanotubes to environmental contaminants such as oxygen, water, etc. has recently been appreciated[78,79]. Parameters such as the room temperature electrical resistivity and the resistance vs. temperature behavior of multi-walled

and single-walled carbon nanotubes has been found to change dramatically upon baking under vacuum. This is especially true of semiconducting nanotubes where dopants such as oxygen donate holes to the valence band making the tubes p-type. Also, some work has been done to investigate the effects of doping nanotubes with alkali metals such as potassium. Based on the curvature argument in section 2.5, alkali metal doped nanotubes have a good chance of exhibiting superconductivity.

Another interesting nanotube dopant is Buckminsterfullerene. It has been reported that heating single-walled carbon nanotubes in the presence of C_{60} under vacuum allows the fullerene molecules to diffuse inside the nanotubes. The report shows convincing TEM micrographs of "nanopeapods" consisting of linear chains of C_{60} trapped inside single-walled tubes approximately 1.3 nanometers in diameter. This unusual system may exhibit unique transport properties as the fullerene molecules move about inside the tubes under the influence of thermal energy and electric field. Another possibility is that doping these tubes with alkali metals may cause the fullerenes to go superconducting just as in K_3C_{60}.

This brief study attempts to investigate changes in the transport behavior of single-walled carbon nanotubes after treatment with various dopants. In the initial experiment, a mat of single-walled carbon nanotubes is baked out under vacuum and resistance vs. temperature data is compared to data taken before baking to determine the effect of oxygen doping. Because it is necessary to reexpose the mat to air in preparation for further doping experiments, the mat was baked out again prior to every subsequent doping experiment. Next, the mat was doped with C_{60} and potassium in separate steps. Resistance vs. temperature data was recorded at each stage of the process.

A new type of doping cell was designed and built for this experiment to allow baking up to 425°C. Specifically, this high temperature required that the cell not contain any organic materials such as epoxy or silver paint. A very simple design was developed by using a glass disk approximately 1/8" thick and a diameter of 12 mm. The disk was masked off and platinum was sputtered onto it so each side of the disk had four separate platinum pads. For each pad, platinum was sputtered around the side to connect to one of the pads on the other side of the disk. Next, the disk was placed inside a pyrex tube with a 12 mm inner diameter and fused in place with a small torch. Care had to be taken so that the platinum in the seal didn't melt. The result was a sealed pyrex tube with 4 platinum leads on the outside being connected to contact patches on the inside.

To mount the tubes, a sample of single-walled nanotubes was purchased from the company, Tubes at Rice. These nanotubes are sold as a dispersion in concentrated Triton X-100 surfactant. The nanotubes were crashed out of this suspension by washing several times in distilled water followed by acetone and methyl alcohol. While washing with water, the tubes clumped into a single mat in the liquid. After the last methanol washing, the doping cell was evacuated and the methanol was carefully pumped out. During this process, shaking was necessary to insure that the nanotube mat settled over all four contacts. Once dry, the external platinum contacts were attached to the leads of a low temperature probe with silver paint and resistance vs. temperature data was recorded down to 4.2 K. Afterwards, the tube was evacuated with a turbo pump and simultaneously held at 425°C for about 8 hours. Next, the pyrex tube was flame sealed under vacuum and the resistance vs. temperature was measured once again. Figure 6.5 shows both sets of R vs. T data for the unbaked and baked samples. Both curves show the same general behavior as

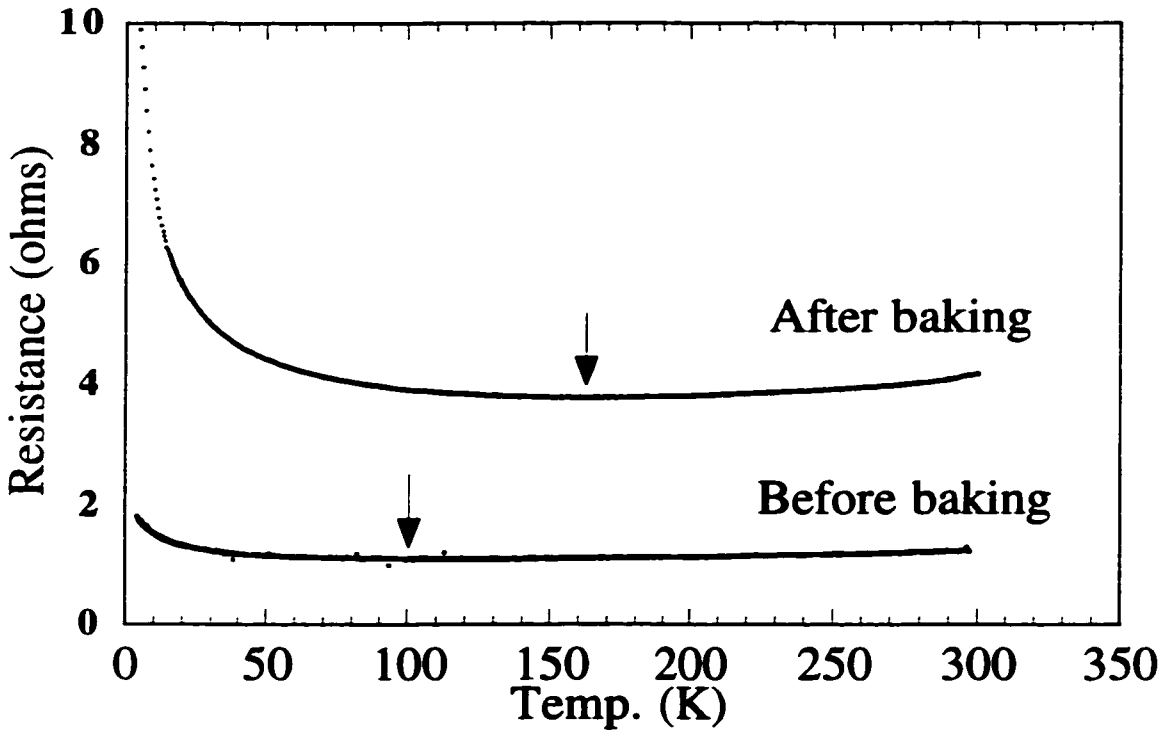

Figure 6.5: Resistance vs. temperature plot of single-walled nanotubes before and after baking at 425°C for 8 hours. The arrows indicate the location of the minimum resistance values.

the temperature is lowered: the resistance gradually decreases until it reaches some minimum, R_{min}, and then it increases fairly dramatically. As shown in this figure, the overall resistance is observed to increase by about a factor of 4. Also, the temperature of the minimum resistance, $T(R_{min})$, indicated by arrows, increased from 100 K to 160 K. This result shows that atmospheric adsorbates do affect the transport properties of carbon nanotubes proving the importance of thoroughly baking all nanotube samples prior to any transport experiment.

Next, the nanotube mat was intercalated with C_{60} to see if this had any influence on the transport properties. First, the tube was broken open and fused to a new tube with a metal to glass seal for baking. About 100 mg of pure C_{60} powder was added and the tube

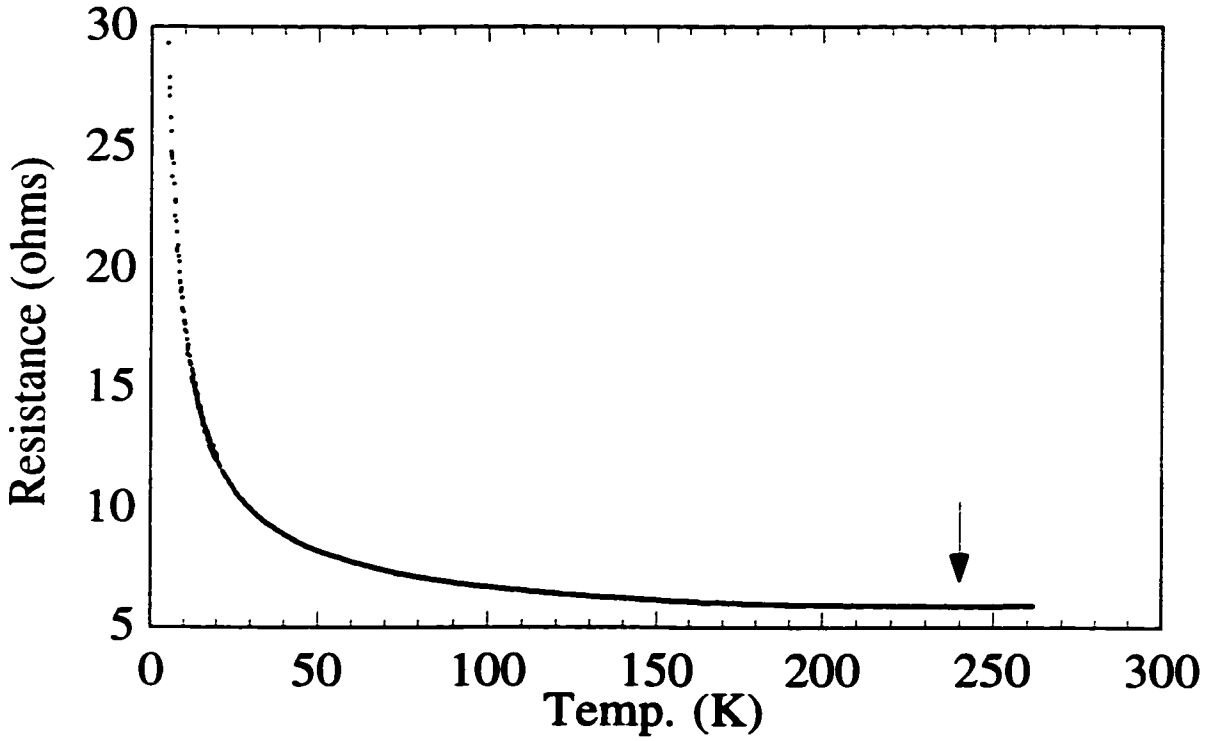

Figure 6.6: Resistance vs. temperature plot of single-walled carbon nanotubes after baking and intercalating with C_{60}. The changes in this curve from the last figure can be explained by additional baking. The arrow indicates the resistance minimum.

was baked out at 425°C for approximately 8 hours under dynamic vacuum. The next day, the tube was flame sealed and baked again at 400°C overnight to allow the C_{60} vapor to intercalate into the nanotubes. The resistance vs. temperature data is plotted in figure 6.6. The changes in this data follow the same trend of the original baking: the overall resistance has increased and $T(R_{min})$ has also increased. Therefore, these changes are most likely a result of additional baking rather than the presence of C_{60} intercalants. From this result, it appears that if C_{60} is present inside the nanotubes, it has very little effect on the tube's electronic properties. However, this should not be concluded until single tube transport has been performed through a nanotube that has been shown by TEM to contain fullerenes.

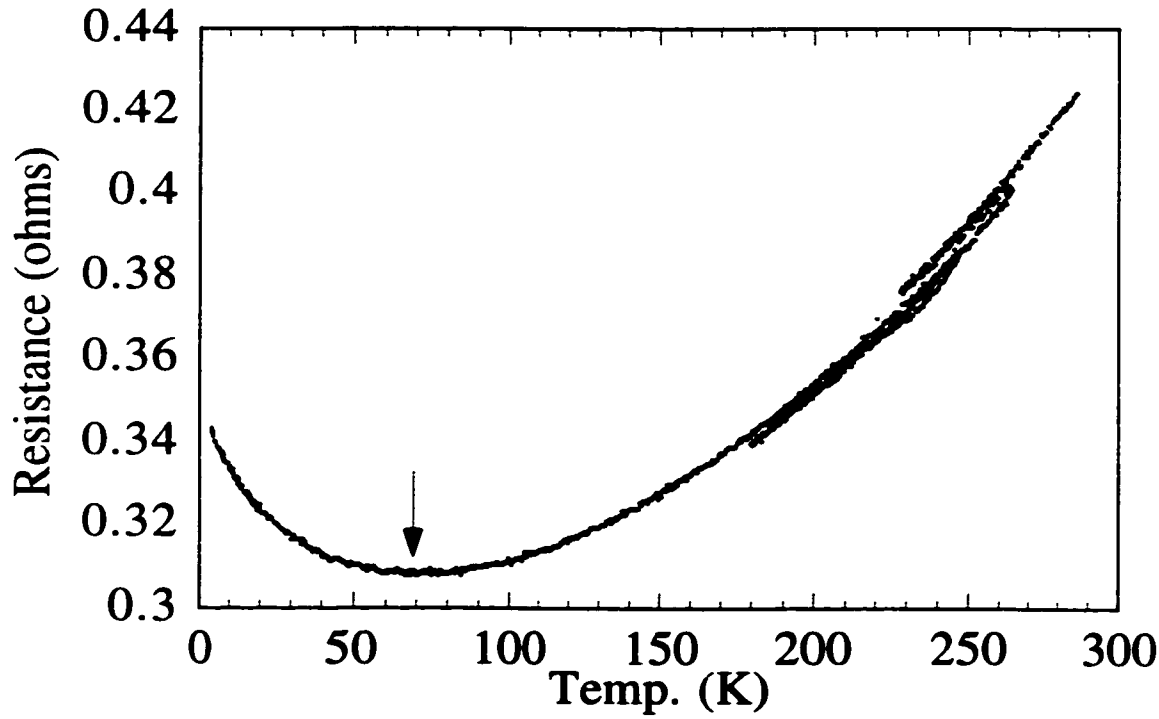

Figure 6.7: Resistance vs. temperature plot of single-walled carbon nanotubes, previously doped with C_{60}, after baking and intercalation with potassium. The alkali metal seems to have reversed the effect of baking. The resistance has dropped and $T(R_{min})$ (indicated by the arrow) is reduced.

Finally, the sample was intercalated with potassium. Again, the tube was broken open and resealed to a new tube with a metal to glass seal. The nanotubes were then baked at 425°C under vacuum for 8 hours. Next, the tube was valved off under vacuum and transferred into the argon glovebox where approximately 100 mg of potassium was transferred into the tube. Under vacuum, some of the potassium was distilled into the side of the tube with the nanotube mat and that side was flame sealed off. This tube was then baked at 350°C for 30 hours. The end containing the nanotubes was kept slightly warmer to insure that none of the potassium condensed on the surface without intercalating. Figure 6.7 shows the resulting R vs. T plot. This plot shows a dramatic decrease in the resistance as well as a drop in $T(R_{min})$.

Bibliography

1. Kroto, H. W., Heath, J. R., O'Brien, S. C., Curl, R. F. and Smalley, R. E., Nature **318**, 162 (1985)

2. Rohlfing, E. A., Cox, D. M. and Kaldor, A., Journal of Chemical Physics **81**, 3322 (1984)

3. Krätschmer, W., Lamb, L. D., Fostiropoulos, K. and Huffman, D. R., Nature **347**, 354 (1990)

4. Hebard, A. F., Rosseinsky, M. S., Haddon, R. C., Murphy, D. W., Glarum, S. H., Palstra, J. T. M., Ramirez. A. P. and Kortan, A. R., Nature **350**, 600 (1991)

5. Palstra, T. T. M., Zhou, O., Iwasa, Y., Sulewski, P. E., Fleming, R. M. and Zegarski, B. R., Solid State Communications **93**, 327 (1995)

6. Haddon, R. C., Acc. Chem. Res. **25**, 127 (1992)

7. Crespi, V. H., Phys. Rev. Lett. **60**, 1, 100 (1999)

8. Hannay, N. B., Geballe, T. H., Matthias, B. T., Andress, K., Schimdt, P. and MacNair, D., Phys. Rev. Lett. **14**, 225 (1965)

9. Hebard, A. F., Physics Today **45**, 11, 26 (1992)

10. See, Separation of fullerenes by liquid chromatography, K. Jinno, ed. (RSC Publishers, Cambridge, 1999)

11. Kroto, H. W., Nature, **329**, 529 (1987)

12. Curl, R. F. and Smalley, R. E., Scientific American, **265**, 4, 54 (1991)

13. Iijima, S., Nature, **354**, 56 (1991)

14. Ebbesen, T. W. and Ajayan, P. M., Nature, **358**, 220-222 (1992)

15. Journet, C., Maser, W. K., Bernier, P., Loiseau, A., Lamy de la Chapelle, M., Lefrant, S., Deniard, P., Lee, R. and Fischer, J. E., Nature **388**, 756-758 (1997)

16. Thess, A., Lee, R., Nikolaev, P., Dai, H., Petit, P., Robert, J., Xu, C., Lee, Y. H., Kim, S. G., Rinzler, A. G., Colbert, D. T., Scuseria, G. E., Tománek, D., Fischer, J. E. and Smalley, R. E., Science, **273**, 5274, 483-7 (1996)

17. Maser, W. K., Munoz, E., Benito, A. M., Martinez, M. T., de la Fuente, G. F., Maniette, Y., Anglaret, E. and Sauvajol, J. L., Chem. Phys. Lett., **292**, 4-6, 587-593 (1998)

18.Jose-Yacaman, M., Miki-Yoshida, M., Rendon, L. and Santiesteban, J. G., Appl. Phys. Lett., **62**, 202 (1993)

19. Luyken, R. J., Masters Thesis, Technische Universität München, München, 1995.

20. Fan, S., Chapline, M. G., Franklin, N. R., Tombler, T. W., Cassell, A. M., Dai, H., Science **283**, 512 (1999).

21. Sun, L. F., Mao, J. M., Pan, Z. W., Chang, B. H., et. al., Appl. Phys. Lett., **74**, 5, 644-646 (1999)

22. Iijima, S. and Ichihashi, T., Nature, **363**, 603 (1993)

23. Bethune, D. S., Kiang, C. H., de Vries, M. S., Gorman, G., Savoy, R., Vazquez, J. and Beyers, R., Nature, **363**, 605 (1993)

24. Hamada, N., Sawada, S. and Oshiyama, A., Phys. Rev. Lett., **68**, 1579 (1992)

25. Saito, R., Fujita, M., Dresselhaus, G. and Dresselhaus, M. S., Appl. Phys. Lett., **60**, 2204 (1992)

26. Saito, R., Dresselhaus, G. and Dresselhaus, M. S., J. Appl. Phys., **73**, 494 (1993)

27. Yorikawa, H. and Muramatsu, S., Phys. Rev. B, **50**, 12203 (1994)

28. Chico, L., Crespi, V. H., Benedict, L. X., Louie, S. G. and Cohen. M. L., Phys. Rev. Lett., **76**, 971 (1996)

29. Lambin, ph., Fonseca, A., Vigneron, J. P., Nagy, J. B. and Lucas, A. A., Chem. Phys. Lett., **245**, 85-89 (1995)

30. Saito, R., Dresselhaus, G. and Dresselhaus, M. S., Phys. Rev. B, **53**, 2044 (1996)

31. Collins, P. G., Zettl, A., Bando, H., Thess, A. and Smalley, R. E., Science, **278**, 100 (1997)

32. Yao, Z., Postma, H. W. Ch., Balents, L. and Dekker, C., Nature **402**, 273 (1999)

33. Treacy, M. M., Ebbesen, T. W. and Gibson, J. M., Nature, **381**, 678 (1996)

34. Chopra, N., University of California, Berkeley PhD Thesis, 1996.

35. Zhu. W., Bower, C., Zhou, O., Kochanski, G. and Jin, S., Appl. Phys. Lett., **75**, 6, 873 (1999)

36. Saito, Y., Hamaguchi, K., Uemura, S., Uchida, K., Tasaka, Y., Ikazaki, F., Yumura, M., Kasuya, A. and Nishina, Y., Appl. Phys. A., **67**, 1, 95 (1998)

37. De Heer, W. A., Chatelain, A. and Ugarte, D., Science, **270**, 5239, 1179 (1995)

38. Rinzler, A. G., Hafner, J. H., Nikolaev, P., Lou, L., Kim, S. G., Tománek, D., Nordlander, P., Colbert, D. T. and Smalley, R. E., Science, **269**, 5230, 1550 (1995)

39. Collins, P. G. and Zettl, A., Appl. Phys. Lett., **69**, 5230, 1550 (1996)

40. Fowler, P. W. and Manolopoulos, D. E., An Atlas of Fullerenes (Clarendon Press, Oxford, 1995)

41. Yamaguchi, Y. and Maruyama, S., Chem. Phys. Lett., **286**, 336 (1998)

42. Kouvetakis, J., Sasaki, T., Chen, C., Hagiwara, R., Lerner, M., Krishnan, K. M. and Bartlett, N., Synthetic Materials, **34**, 1 (1989)

43. Matsui, T., Yudasaka, M., Kikuchi, R., Ohki, Y. and Yoshimura, S., Appl. Phys. Lett., **65**, 17, 2145 (1994)

44. Hummelen, J. C., Knight, B., Pavlovich, J., González, R. and Wudl, F., Science, **269**, 5230, 1554 (1995)

45. O'Brien, S. C., Heath, J. R., Curl, R. F. and Smalley, R. E., J. Chem. Phys. **88**, 220-230 (1988)

46. Piskoti, C., Yarger, J. and Zettl, A., Nature **393**, 771 (1998)

47. Zhang, B. L., Wang, C. Z., Ho, K. M., Xu, C. H. and Chan, C. T., J. Chem. Phys., **97**, 7, 5007 (1992)

48. Heath, J. R., O'Brien, S. C., Curl, R. F., Kroto, H. W. and Smalley, R. E., Comm. Cond. Mater. Phys., **13**, 119 (1987)

49. Heath, J. R. in Fullerenes: synthesis, properties and chemistry of large carbon clusters, ACS Symposium Series G. S. Hammond and V. J. Kuck, eds., **481**, 1 (1991)

50. Koruga, D., Hameroff, S., Withers, J., Loutfy, R. and Sundareshan, M., Fullerene C_{60}: History, Physics, Nanobiology, Nanotechnology (Elsevier Science Publishers, North Holland, 1993)

51. Grossman, J. C., Côté, M., Louie, S. G. and Cohen, M. L., Chem. Phys. Lett., **284**, 344 (1998)

52. Côté, M., Grossman, J. C., Louie, S. G. and Cohen, M. L., Phys. Rev. Lett. **81**, 697 (1998)

53. Jagadeesh, M. N. and Chandrasekhar, J., Chem. Phys. Lett. **305**, 298 (1999)

54. Collins, P. G., Grossman, J. C., Côté, M., Ishigami, M., Piskoti, C., Louie, S. G., Cohen, M. L. and Zettl, A., Phys. Rev. Lett. **82**, 165 (1999)

55. Grossman, J. C., Louie, S. G. and Cohen, M. L., Phys. Rev. B, **60**, 10, R6941 (1999)

56. Côté, M., Grossman, J. C., Cohen, M. L. and Louie, S. G., Proc. 193rd Meeting of the Electrochemical Society, San Diego, CA (1998)

57. Allen, P. B. and Mitrovic, B., Theory of Superconducting Tc, Solid State Physics **37** (1982)

58. Fuhrer, M. S., Cherrey, K., Crespi, V. H., Zettl, A and Cohen, M. L., Phys. Rev. Lett. **83**, 2, 404 (1999)

59. Guo, T., Smalley, R. E. and Scuseria, G. E., J. Chem. Phys. **99**, 352 (1993)

60. Heath, J. R., O'Brien, S. C., Zhang, Q., Liu, Y., Curl, R. F., Kroto, H. W., Tittel, F. K.and Smalley, R. E., J. Am. Chem. Soc. **107**, 7779 (1985)

61. Lykke, K. R., Parker, D. H. and Wurz, P., International Journal of Mass Spectrometry and Ion Processes **138**, 149 (1994)

62. Khachaturyan, K. and Weber, E. R., Phys. Rev. B **36**, 8309 (1987)

63. Blazey, K. W., Portis, A. M. and Bednorz, J. G., Solid State Commun. **65**, 1153 (1988)

64. Warden, M., Stalder, M., Stefanicki, G., Portis, A. M. and Waldner, F., J. Appl. Phys. **64**, 5800 (1988)

65. Chavan, S. A., Yakhmi, J. V., Gopalakrishnan, I. K., Materials Science and Engineering **C3**, 175 (1995)

66. Hirsch, A., The Chemistry of the Fullerenes (G. Thieme Verlag, New York, 1994)

67. Jiao, J., Seraphin, S., Wang, X. and Withers, J. C., J. Appl. Phys. **80**, 1, 103 (1996)

68. Jiao, J. and Seraphin, S., J. Appl. Phys. **83**, 5, 2442 (1998)

69. Saito, Y., Mu, J., Nakashima, J. and Masuda, M., Zeitschrift fur physik D (atoms, molecules and clusters) 40, 1-4, 170 (1997)

70. Bergemann, C., Muller-Schulte, D., Oster, J., a' Brassard, L. and Lübbe, A. S., J. of Magnetism and Magnetic Materials **194**, 1-3, 45 (1999)

71. New Trends in Magnetism, Magnetic Materials and Their Applications, J. L.Morán-López and J. M. Sanchez, eds. (Plenum Press, New York, 1994)

72. Magnetic Properties of Fine Particles, J. L. Dormann and D. Fiorani, eds. (Elsevier Science Publishers, Amsterdam, 1992)

73. Ebbesen, T. W. and Ajayan, P. M., Nature **358**, 220 (1992)

74. Ebbesen, T. W., Ajayan, P. M., Hiura, H. and Tanigaki, K, Nature **367**, 519 (1994)

75. Maiti, A., Brabec, C. J., Roland, C. and Bernholc, J., Phys. Rev. B **52**, 20, 14,851 (1995)

76. Buongiorno Nardelli, M., Brabec, C., Maiti, A., Roland, C. and Bernholc, J., Phys. Rev. Lett. **80**, 2, 313 (1998)

77. Charlier, J., De Vita, A., Blase, X. and Car, R., Science **275**, 646 (1997)

78. Collins, P. G., Ishigami, M. and Zettl, A., Bull. Am. Phys. Soc. **44**, 1889 (1999)

79. Collins, P. G., Bradley, K., Ishigami, M. and Zettl, A. To be published in Science (March 10, 2000)